Clemson University

TigerPrints

All Dissertations

Dissertations

May 2020

Material Properties of Anderson Localizing Optical Fiber

Matthew Artus Tuggle
Clemson University, mtuggle578@gmail.com

Follow this and additional works at: https://tigerprints.clemson.edu/all_dissertations

Recommended Citation
Tuggle, Matthew Artus, "Material Properties of Anderson Localizing Optical Fiber" (2020). *All Dissertations*. 2584.
https://tigerprints.clemson.edu/all_dissertations/2584

This Dissertation is brought to you for free and open access by the Dissertations at TigerPrints. It has been accepted for inclusion in All Dissertations by an authorized administrator of TigerPrints. For more information, please contact kokeefe@clemson.edu.

MATERIAL PROPERTIES OF ANDERSON LOCALIZING OPTICAL FIBER

A Dissertation
Presented to
the Graduate School of
Clemson University

In Partial Fulfillment
of the Requirements for the Degree
Doctor of Philosophy
Materials Science and Engineering

---

by
Matthew A. Tuggle
May 2020

Accepted by:
Dr. John Ballato, Committee Chair
Dr. Arash Mafi
Dr. Stephen Foulger
Dr. Konstantin Kornev

ABSTRACT

Over half a century ago, the paper entitled “Absence of Diffusion in Certain Random Lattices” was published by P. Anderson and described a metal-to-insulator transition phenomenon where electron diffusion does not occur in disordered semiconductors. This phenomenon is now commonly referred to as “Anderson localization” (AL). Since the AL detailed in Anderson’s paper arose from the wave nature of electrons, similar behavior should be observed in other wave systems, more specifically in optics.

Given the utility of optical fibers, extensive theoretical treatment has been conducted on *transverse* Anderson localization (TAL, disorder in x- and y-directions, with the z-direction remaining invariant) in such systems. Only recently has it been experimentally observed, paving the way for studies into the influence of fiber material on linear and nonlinear TAL. *This Dissertation represents the first materials study of doped silicate transverse Anderson localizing optical fibers (TALOFs) and their corresponding passive and active optical properties.*

More specifically, Chapter I reviews microstructured and multicore optical fiber, and methods of their fabrication, in order to develop an understanding of the impact of the core microstructure on waveguide properties. Then, an overview of TALOFs is developed to provide insights into the different materials and fabrication methods used to develop the few TALOFs reported to date. The former fiber systems are well studied; therefore, this research Dissertation will be focused on the novel effects and material influences on the latter (Anderson) systems.

Chapter II begins the development of these novel fibers through *in situ* phase separation in optical fibers drawn using the molten core method (MCM). Limitations in the resulting fibers were studied, and adaptations to the fabrication method were made to elongate the already formed microphases through development and subsequent use of a two-tier MCM.

Chapter III introduces an alternative fiber fabrication technique, namely the stack-and-draw method, specifically adapted to utilize MCM-derived precursor fibers in the stack. The resulting fibers are characterized to understand the effects of processing on the core microstructure, and ultimately to understand how the core microstructure leads to TAL.

Chapters IV and V investigate the material properties and potential applications of the TALOFs that resulted from the fabrication technique developed in Chapter III. Specifically, Chapter IV investigates both Yb^{3+} and Er^{3+} doped TALOFs for solid-state lasing and amplification respectively. The resulting experimental observations and present limitations of these fibers for active applications are discussed.

In Chapter V, the first nonlinear optical TALOFs are explored. Even though the higher refractive index phases possessed an estimated nonlinear refractive index (n_2) similar to silica, small modal effective areas were demonstrated due to the strong localization in certain regions of these TALOFs. As a result, nonlinear optical frequency shifts were demonstrated for the first time in a TALOF, attributed to Raman and four-wave mixing (FWM), concomitantly. While not decisive into the underlying nature of

TAL in the presence of optical nonlinearities, this suggests that the two are not mutually exclusive.

Finally, Chapter VI summarizes the findings of this Dissertation, discusses the challenges with further fiber development in these TALOFs, and provides examples for future efforts in improving both the fibers themselves, and ultimately the understanding of these fibers.

DEDICATION

Through the highs and lows that life has handed us along the way, this Dissertation is dedicated to my family and loved ones. Thank you for encouraging me through this unforgettable endeavor.

ACKNOWLEDGMENTS

First and foremost, I would like to thank my Advisor, John Ballato. This has been a fun, challenging, and overall incredible journey and I thank you profusely for allowing me to embark on this unforgettable adventure. Your attentiveness and sincerity brought reason and purpose to this project, even when nothing seemed to be working. *From one old man to another, thank you for supporting me throughout this Dissertation!*

I would also like to thank our collaborator, Arash Mafi, for patiently working with me on this difficult optical fiber project. He has taught me the challenges with the theoretical and experimental physics associated with these fibers, and how to appreciate the theoretical groundwork laid out for this project. Thank you to the rest of the UNM group as well, Cody Bassett, Mostafa Peysokhan, and Esmail Mobini for hosting me at the lab. It was a few short weeks; however, we've built long-lasting friendships. I would especially like to thank Cody for teaching me the basics of these measurements and persevering through to observe something remarkable in these fibers.

To the rest of my committee, Stephen Foulger and Konstantin Kornev, I am especially grateful for your time and for agreeing to participate on my committee. Thank you both for supporting this project and challenging me to always be better.

I am forever grateful for the rest of the Ballato group; Maxime & Benoit (or Maxoit for short), Baris, Josh F., Courtney, Bailey, Robert, and especially Wade. The former few taught me the necessary components of making optical fiber, and the latter one taught me that everything is thrown out the door when it comes to *actually making* *the fibers*. Thank you all for your gifts of knowledge, collaboration, and the many times of laughter. I wish you the best in the careers ahead of us!

I would like to thank other Clemson University faculty and staff who have helped with this research and made my time at Clemson unforgettable; Gary Lickfield, Kyle Brinkman, Thompson Mefford, Bobbert Bowen, Kim Ivey, Donald Mulwee and George Wetzel. Go Tigers!

To the best of friends, I would like to thank you all for the fun times and countless memories that truly tell the story of my time at Clemson. Thank you, Anwar, Big Ben (Fellows), Little Ben (Grant), Dmitriy, Eric, Haley, Tony, and all the gaming folk. There will always lunch to be had, a new board game to play, or a new world to explore. I will always cherish these moments with each of you. Also, a special thanks to my UG friends, many of whom have since left Clemson, Austin, Dakota, Hannah, Kat, and Leslie.

In all cases above, the list of people to which I express my gratitude is extensive. If I have overlooked any names, it is by no means due to a lack of appreciation. Your friendships and memories are always cherished!

To my parents, Steve and Patti, and my sister, Emaleigh, I would like to say thank you for your unrelenting support. If times were easy or difficult, you were always willing to lend an ear, and for that I am grateful. To friends of the family, Bob and Liz Q, I thank you copiously for your constant inspiration and personal mentorship.

Finally, I would like to say thank you to the “poshest pish” in the sea, the one and only Salmon (Sam). You have encouraged me every step along this journey; I am forever grateful for your patience, support, and you. *Thank you for being special to me*.

TABLE OF CONTENTS

LIST OF TABLES

Table Page

LIST OF FIGURES

Figure Page

List of Figures (Continued)

Figure Page

List of Figures (Continued)

Figure Page

List of Figures (Continued)

Figure Page

List of Figures (Continued)

Figure Page

List of Figures (Continued)

List of Figures (Continued)

Figure Page

CHAPTER ONE

TRANSVERSE ANDERSON LOCALIZING OPTICAL FIBERS: APPLICATIONS AND FABRICATION TECHNIQUES

I. A. A (brief) introduction to optical fiber

Optical fibers are integral components within numerous high value applications, including (and by no means limited to) *in vivo* medical research [1-3], telecommunications [4-7], high energy fiber lasers (HEFL) [8-10], and nonlinear fiber optics [11-13]. In a report to the Office of Science and Technology in 2012, optics and photonics directly influences \$7.5 trillion in global markets with more than half assigned to the telecommunications sector alone [14]. All information currently transported for the internet and voice communications occurs over fiber optic systems [14], including back-end wireless networks.

Conventional (cylindrical) optical fiber consists of a high refractive index core surrounded by a low refractive index cladding, generally a doped-silica core with a pure (or fluorine-doped) silica cladding. Light coupled in the fiber remains confined in the core by means of total internal reflection. The light propagates along the fiber in certain allowed field distributions, known as modes. An optical fiber is considered single-mode (SM) if only the fundamental mode (LP_{01}) propagates in the core. If higher order modes can propagate, the fiber is considered multi-mode (MM). In practice, it may be difficult to visibly determine the presence of higher-order modes [15]. A fundamental limit based on fiber parameters exists such that SM operation occurs if $2\pi(a/\lambda)(NA) < 2.405$, with a

being the core radius (μm), λ being the incident wavelength (μm), and NA being the numerical aperture equal to $(n_{core}^2 - n_{cladding}^2)^{1/2}$. This equation defines the normalized frequency also known as the "V value." Since an optical fiber is generally determined for specific wavelength-dependent applications, λ then is fixed, while a and NA are varied when designing the fiber. While SM and MM are both efficient in waveguiding, each can satisfy very different applications. SM fibers are often adopted for long-haul telecommunication networks as only the fundamental mode can propagate, minimizing signal distortion over long lengths [16]. MM fibers generally possess larger core areas which can be used for HEFL allowing for higher power coupling into the (active) fiber core [17].

Complimentary to conventional single-core fibers are microstructured optical fiber (MOF). These are optical fibers comprised of intentional micro-inclusions, whether multiple cores that guide light, or multiple periodic inclusions that dominate transverse propagation characteristics of the light. The former is commonly referred to as a multicore optical fiber and the latter is often considered photonic crystal fiber (PCF). The architecture of a MOF is generally periodic, however recent developments in fiber waveguiding has generated interest in randomly distributed inclusions [18]. Interesting and rather clever adaptations of random air structures has been introduced into the cladding of an optical fiber yielding bend-insensitive fibers for fiber-to-the-home [19]. PCFs generally waveguide either by an effective refractive index difference between the core and microstructured cladding, or by a photonic bandgap that exploits periodic inclusions in the core, such that the transverse component of the electromagnetic wave undergoes interference. The latter creates Bragg-like conditions that limit the allowed and forbidden propagation directions, thereby limiting transverse propagation of light in the fiber [20]. Multicore fibers are generally designed for increased transmission capacity or

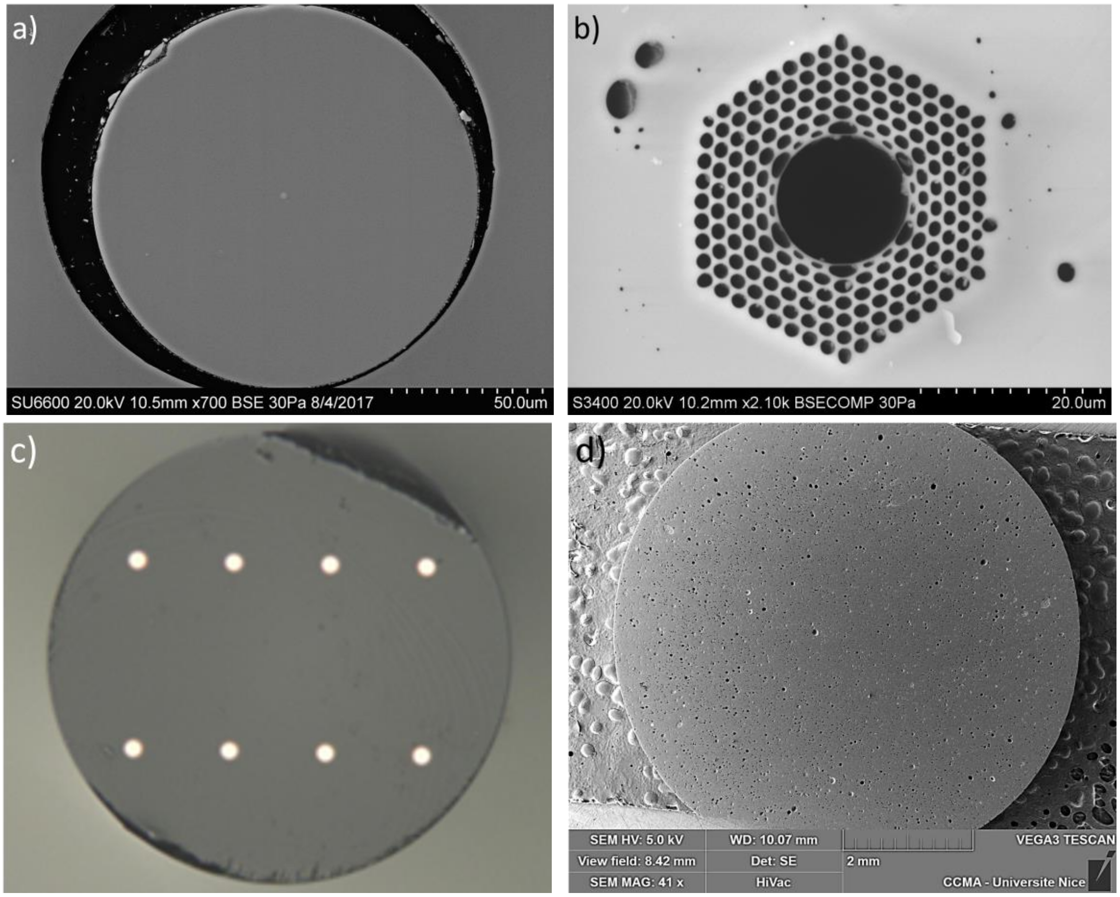

Figure I.1. Representative electron micrographs depicting the cross-sections of a) core/clad fiber, b) PCF, c) multicore fiber, and d) TALOF. Images b-d provided by, Thomas (Wade) Hawkins (Clemson University), Kevin Bennet (Corning Inc.), and Dr. Wilfred Blanc (University of Nice, France) respectively. In figures a and c, the bright regions indicate doped cores whereas in figures b and d, the dark spots are hollow.

image transport. Multicore transmission fibers are engineered such that the cores are separated enough to minimize crosstalk between cores (known as core-to-core coupling) for space-division multiplexing (SDM) [21]. SDM occurs when multiple beams are coupled into discrete channels within a single optical fiber. For imaging fibers, since crosstalk is not as detrimental, a higher concentration of cores per cross-sectional area is possible.

Of the randomly distributed structures within a MOF, random air structures in the cladding have shown to limit transverse propagation of light into the cladding, minimizing bend-loss in specialty fibers [19]. Random structures in the core, however, have recently been investigated for a rather interesting waveguide mechanism known as (transverse) Anderson localization of light [22]. If these random structures, possessing different dielectric constants compared to the surrounding glass matrix, are sufficiently disordered, then light coupled into the core scatters and becomes transversely localized (meaning the beam does not diffuse) as it propagates along the fiber.

While extensive research has been conducted in both industry and academia regarding the fabrication of optical fiber, these efforts have primarily focused on mitigating disorder, often inducing loss or other parasitic effects, through ultra-high purity vapor deposition techniques, albeit with good reason (see $7.5 trillion economic value comment above). Much of the current understanding of optical fiber fabrication coincides with eliminating scattering centers (impurities, inhomogeneities) that constitute extrinsic sources of excess loss. A fundamentally novel waveguiding mechanism in optical fiber, such as the aforementioned transverse Anderson localization, will undoubtedly require uniquely engineered fabrication techniques, especially when disorder is necessary. In recent years, alternative fiber fabrication methods have resulted in performance advances relating to specialty optical fiber, for example, a versatile melting technique, the Molten Core Method (MCM) [23], and a stack-and-draw method effective in developing MOFs and PCFs [20]. The MCM was originally conceived as a means for obtaining otherwise unstable high rare-earth oxide concentration core (specifically terbium oxide) glasses for all-fiber Faraday isolators [24]. In the 25-year lifespan of the MCM, it has been used to develop a wide variety of optical fibers, including crystal-derived optical fiber [25-27], semiconductor fibers [28,29], highly nonlinear fibers [30], and low quantum defect fiber lasers [31], to name a few.

I. B. Microstructured / multicore optical fiber

Microstructured optical fiber (MOF) are fibers that waveguide through design of the core structure. Waveguiding can occur through a photonic bandgap, or total internal reflection with a change in the effective refractive index of the cladding. Multicore optical fiber are fiber waveguides that have multiple cores in the transverse facet of the fiber each capable of waveguiding. Multicore optical fibers are generally not considered microstructured optical fiber, since each core is designed to waveguide, whereas, for MOFs, the microstructure determines waveguiding properties.

Multicore optical fibers have been utilized within many areas of optics and photonics such as multicore fibers for space-division multiplexing (SDM) [21,32,33], photonic lanterns for couplers between multimode and single mode fibers [34,35], and image transport [36,37]. On the other hand, MOF can include photonic bandgap fibers (photonic crystal fibers) [20], which have been developed for many novel devices [38] and applications, including effectively single-mode propagation in large area cores for high energy (fiber laser) applications in all-solid [39] and glass-air (holey) [40,41] fibers. Additionally, silica-based fibers with air inclusions, introduced through gas pumped into the fiber during fabrication, has been demonstrated featuring a nanostructured ring around the fiber core which has resulted in lower bend-loss fibers [42] for applications such as fiber-to-the-house.

I. B. 1. Periodicity

I. B. 1. 1. Microstructured optical fiber (PCF)

Photonic crystal fibers (PCFs) were pioneered by Prof. Philip Russell's group at the University of Southampton and the University of Bath in the United Kingdom in the mid- to late- 1990's. They were first proposed in 1995 [43] and fabricated a year later in 1996 [44]. Since their inception, PCFs represent a very active research field in optics and photonics. PCFs are optical fibers that possess periodic microstructures on the wavelength scale. The first PCF [44] contained a hexagonal-shaped microstructure around a "lattice-defect site." It was fabricated using a stack-and-draw technique whereby a 30 mm silica rod with a 16 mm hole was milled to form a hexagonal shape and was drawn down to 0.8 mm for the "precursor" material. The hexagonal fibers were cut to length and stacked in an overclad tube to be drawn to the final fiber with a periodic array of air-holes ~300 nm in diameter with an average center-to-center spacing (pitch) of 2.3

μm [20]. The hexagonal precursor fibers enabled a high degree of periodicity in the final fiber. The pitch and air-hole diameter could easily be tailored by modifying the dimensions of the hole in the initial silica rod, or the dimensions of the silica rods themselves. A high-index defect was purposely introduced in the center of the PCF by replacing the middle hollow-core hexagonal silica rod with a solid one. “High index” in this case does not necessarily mean higher refractive index than silica. The air holes surrounding this lattice-defect site reduce the effective refractive index around the center, thereby the lattice-defect becomes “high-index.” This high-index core, surrounded by an effectively lower refractive index cladding, permits waveguiding by a modified total internal reflection [20].

Even in the early PCFs, rather remarkable discoveries were made. Endlessly single-mode propagation was demonstrated [45,46], whereby a cutoff wavelength (λ below which MM becomes SM, for a given core radius and fiber NA) does not exist for a specific PCF microstructure. This phenomenon is attributed to the influence of the incident wavelength (λ) on the effective refractive index of the cladding (n_{clad}), which, in turn, impacts the optical V-value (which defines the number of allowed guided modes) through a change in the NA. As λ (denominator) decreases, the effective refractive index of the cladding (numerator) increases, extending the wavelength range for single-mode propagation. The true range is also dependent on the ratio of the diameter of the air-holes (d) to the center-to-center spacing (Λ) [45]. For $d/\Lambda < 0.4$, effectively endless single-mode propagation occurs [47]. With this phenomenon in mind, effectively single-mode, large mode area fibers, some possessing mode areas in excess of 1000 μm^2 [41,48] have been realized and are utilized in high energy laser applications [49]. Increasing the mode area of the fiber increases the power threshold values where parasitic optical nonlinearities arise [50]. More recently, PCFs have also shown the capability for supercontinuum generation [51,52], and photonic bandgap propagation (PBFs) [53-55].

PBFs guide-light due to a two-dimensional photonic bandgap in which transverse propagation into the periodic structure is forbidden [43]. This form of waveguiding allows light to be confined in lower-index regions, even air in hollow-core fibers [56-59]. PBFs were first realized as the “Bragg fiber” [60] in which Bragg reflectors are layered around a cylindrical waveguide, restricting transverse propagation of light. For this to be practical though, a substantially high index difference ($\Delta n = 2.66$) is necessary [61] which is likely not tenable in conventional glass optical fibers. PBFs reported in literature have periodic microstructures that are either all-solid [54,55] or contain air holes [45,48,51,53,56-59].

Much of the original research in the 1990’s investigating PCFs and PBFs resulted from Prof. Philip Russell’s group as noted. Presently, significant strides are being made by Prof. Liang Dong at Clemson University in developing these microstructured optical fiber. Recent advancements include near single mode, large area core fibers [62], high power, large area core Yb-doped fiber lasers [63], and efficient mid-IR supercontinuum generation in a solid tellurite-based fiber [64].

Many developments in PCFs and PBFs have been directed towards improving power-scaling in high-energy fiber lasers. While the large modal area has a tendency to reduce certain optical nonlinearities (Stimulated Brillouin Scattering and Stimulated

Raman Scattering) that presently plague power-scaling, others become more prevalent (transverse mode instabilities) [65]. In addition to these nonlinearity limitations, PBFs have limited allowable bandwidth depending on the microstructure and precise microstructures are necessary for efficient waveguiding capabilities.

I. B. 1. 2. Multicore optical fiber

A multicore fiber, as the name suggests, is a single optical fiber, possessing multiple cores each with the capability of transmitting information along the length of the fiber. Multicore fibers have been used in various applications, such as increased data-capacity for telecommunications fibers [21], photonic lanterns for low-loss interfaces between single- and multi-moded fiber systems [66] and imaging either for magnification [67] or image transport [68]. A major hinderance with multicore optical fiber is crosstalk between cores [69]. As an optical mode propagates along the core, some of the signal is lost to the evanescent field in the glass surrounding the core. Light lost to the evanescent field may leak into the surrounding cores, if too close in proximity, causing distortion to the signal and loss. Generally, crosstalk levels of -25 dB are necessary for negligible detrimental effects on the transmission in telecom fibers [70].

Commercial multicore telecom fibers generally possess 7 cores, spaced ~40 μm apart, arranged in a hexagonal shape encompassed in a 0.018 mm^2 fiber [71]. This arrangement minimizes the number of nearest neighbors of each core, thereby reducing the effects of core-to-core crosstalk [21]. More uncoupled cores existing in a single optical fiber yields higher overall bandwidth in the fiber, since each distinct core generally has the same capacity of a standard SM fiber. The fiber diameter is generally designed to be near to existing fiber diameters, as to reduce coupling losses. Since telecom-grade fibers operate over hundreds of kilometers, crosstalk levels must be sufficiently low. Recently, a configuration with 12 cores was reported with a similar magnitude of crosstalk compared to a 7-core fiber [72]. Larger fiber possessing 19 cores have been reported, though the crosstalk levels were too high, resulting in high levels of signal distortion over a few kilometers [73].

For image transport fibers, such as in multicore fiber medical endoscopes, the image resolution is determined by the number of pixels per unit area. The higher the resolution, the more pixels per unit area. Each pixel is a result of an individual core guiding light. If the cores are too close, crosstalk occurs, and the image becomes distorted [68]. However, since the propagation length is generally not more than a meter or two, the magnitude of core-to-core crosstalk can be significantly higher than the telecom counterpart before becoming detrimental to the image transport quality. An example of commercial imaging fibers consists of 6,000 cores in a 0.083mm^2 area, up to 100,000 cores arranged in a 1.54mm^2 area [74]. Generally, these cores are arranged in a highly ordered microstructure to increase the packing factor, effectively achieving the highest number of cores possible per unit area. Slight variations in the core properties do exist, and are either intentionally induced to reduce crosstalk, or are a result of the fabrication technique.

I. B. 2. Non-periodic (random) inclusions

Randomness is oftentimes avoided as the lack of controlled microstructure results in undesired scattering and loss, which diminishes the quality of the optical waveguide. In certain specific applications, this randomness enhances certain fiber characteristics, such as random air-lines in the cladding surrounding an optical fiber core [42] and novel waveguiding in Transverse Anderson Localizing Optical Fibers (TALOFs) [75]. In the former system, a random distribution of air holes in a nanostructured ring around the core serves the very specific purpose of minimizing bend-loss in premise- / edge-scale optical fiber by decreasing the effective refractive index around the core, the magnitude of which is significantly higher than if realized through conventional (glass compositional) doping techniques. This low-index ring reduces the power in the cladding outside of this region, effectively minimizing bend loss. The latter (Anderson / TALOF) systems contain micro-inclusions in the core, similar to PCFs, however the randomness permits a larger possible propagation bandwidth. Although nascent in terms of total research activities and fibers realized, TALOFs have already shown promise in several early applications, such as image transport fibers with imaging capabilities equivalent to if not better than commercial imaging fibers [76], SM operation [77], multiple beam propagation [78], and directional random lasing [79].

I. B. 2. 1. Transverse Anderson localizing optical fibers

In 1958, P. W. Anderson theorized the absence of diffusive wave transport in a highly disordered scattering media [80], specifically with respect to the diffusion of electrons in a (doped) semiconductor material. The theory states, at sufficiently low densities, [electron] transport does not occur and the wavefunctions remain localized [80]. The theory is based on classical wave-behavior; therefore, it is not limited to the transport of electrons. In 1984, S. John proposed the localization of electromagnetic waves in a three-dimensional disordered medium [81,82], shifting studies of Anderson localization to photon transport. Interestingly, 4 years prior, S. S. Abdullaev and F. K. Abdullaev proposed a pseudo-2D disordered *optical* fiber and theorized the existence of localized optical modes that would propagate along the fiber due to a transversely randomized cross-section [83]. This manuscript was published in a Russian journal and, unfortunately, was omitted from translated versions. Therefore, the initial proposal of Abdullaev and Abdullaev went largely undiscovered [84].

In addition to the novel localization of electrons [80, 85] and photons [81,82], Anderson localization has subsequently been studied with acoustic waves including ultrasound [86], matter waves in cold atoms [87], and has even been postulated for supporting quantum information storage [88]. While the theoretical work is bountiful, experimental observations in many of these fields remains scarce [75] due to the difficulty of developing strongly scattering disordered materials. In a recent instance, experimental evidence is even correcting the theory presented almost 30 years prior [89].

Anderson localization can occur within materials when the mean free path of scattering sites is on the order of the incident wavelength. Known as the Ioffe-Regel criterion [90], this appears as $kl^* \sim 1$ with k being the effective wavevector and l^* being the scattering transport length (or the mean free path). This is notoriously difficult to satisfy in 3-dimensional systems, however for 1- and 2-dimensional optical systems the Ioffe-Regel criterion is more easily satisfied [91]. Therefore, in 1D and 2D systems, all waves appear localized if, as it relates to fiber optics, the radius (ξ) of the localized mode is smaller than the radius of the scattering medium [92] (i.e. for optical fiber, light is not guided by total internal reflection). In the 1980's, a pair of visionaries, Abdullaev, *et al*., (mentioned above), and De Raedt, *et al*., presented pseudo-two-dimensional models necessary for simplifying the structural dimensionality [83,91]. These models represented transversely disordered, dielectric fiber-like systems in which light freely propagates along one direction (z) but remains confined in the other two directions (x and y), deemed *transverse* Anderson localization (TAL) [75].

Even though both proposed structures possess sites with varying refractive indices in the *transverse* (x- and y- direction) that remain longitudinally invariant, notable differences exist between the two architectures (Figure I.2a-b). The structure proposed by Abdullaev, *et al*. [83] consists of a 2D randomized array of coupled optical fiber with randomly distributed physical parameters, such as diameter or pitch, such that the propagation constants of each fiber is randomly distributed. Since the fibers are coupled, it is expected that the light will tunnel between cores. However, the efficiency of the optical tunneling will be random, due to the random distribution of propagation constants [94]. The structure proposed by De Raedt, *et al*. [91] on the other hand, divides the cross-section of the propagation media (or the core) into "pixels," with the width of each pixel being approximately the wavelength of light. The refractive index of each pixel is randomly varied as either n_1 or n_2 with equal probability, thereby obtaining a fill-ratio of

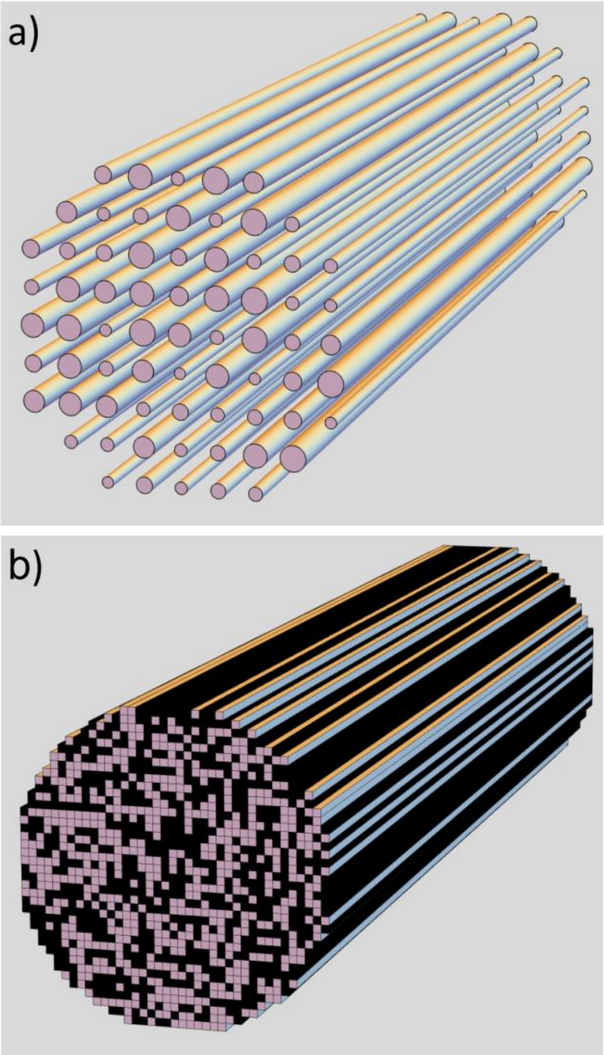

Figure I.2. Representative models of pseudo-2D disordered fibers proposed by a) Abdullaev, *et al*., [82] consisting of randomly coupled optical fibers with varying diameters and by b) De Raedt, *et al*., [83] consisting of completely random refractive index in the transverse plane. Both depictions possess longitudinal invariance along the length of the fibers. Reproduced from [93].

0.5. De Raedt, *et al.*, showed that an optical mode propagating in a fiber possessing this structure will tend to remain localized in the transverse plane due to the transverse scattering.

TALOFs can be exemplified as a combination of MOF and multicore optical fiber. The random microstructure determines the effective waveguiding properties [95] and multiple distinct localized modes can be excited across the transverse facet of the fiber [78], yielding in a sense, a multi-“core” optical fiber that waveguides according to the resulting microstructure. In a TALOF, the dielectric constant remains invariant along the length of the fiber (propagation direction) while varying randomly in the one or two transverse directions. The term “sites” described henceforth is a glass phase represented by each pixel in Figure I.2.b. (e.g. Site 1 is the black pixel and Site 2 is the pink pixel) with the color of each pixel represent a unique glass phase coexisting within the bulk. The material / microstructural requirements to for TAL to be observed are defined as: 1) the disorder exists in the transverse plane of the waveguide (longitudinally invariant), 2) the scattering strength is sufficiently strong (refractive index of scattering centers approaching 0.1 or greater), 3) the mean free path of scattering sites (or pitch, Λ) in the system is on the order of the incident wavelength (corresponding to a site diameter being roughly 1 µm), and 4) the fill-ratio (ratio of site 1 to site 2) of the disorder is approximately 0.5 [92]. These requirements will be important later in this Dissertation as novel TALOFs are designed, fabricated, and tested.

The field of transverse Anderson localization of light has grown substantially since first proposed in 1984 (following S. John’s initial proposal on translating localized electronic states to localized optical modes) [81]. Research groups from across the world are studying these novel effects, from countries including (and by no means limited to): Italy, France, Germany, Switzerland, United States, Netherlands, Norway, Japan, China, India, and the Czech Republic. Figure I.3 provides the present number of publications (both conference proceedings and journal manuscripts), and citations per year, relating to the fabrication and material properties of both polymer and glass-derived transverse Anderson localizing *optical fiber*, beginning with the fabrication of the first TALOF in

Figure I.3: Graphic of the number of publications from publications (conference proceedings and peer-reviewed journals, orange) per year. Also plotted is the number of citations per year (blue), as of 01/10/2020.

2012, up to the publication of this dissertation. The general field of transverse Anderson localization of light (not limited to optical fiber waveguides) is significantly larger, however since this dissertation focuses on optical fiber waveguides, the publications comprising Figure I.3 are exclusively related to TALOFs. The number of manuscripts published in peer-reviewed journals still resides in the single-digits each year, however, a number of these manuscripts have been published in highly esteemed journals such as Scientific Reports, Nature – Light: Sciences and Applications, and Nature Communications, with the total number of citations exceeding 200 in 2019.

In the 1970's, before transverse Anderson localization of light was even proposed, a research scientist named Thomas Seward (Corning Incorporated, Corning, NY) was investigating phase separated glass systems and studying the ability of the formed microphases to elongate [96]. The phase separated glass investigated was comprised of 60% B_2O_3 – 40% PbO (by weight), formed using a conventional batch melting technique. *Seward* found that if a phase separated glass was heated near its softening point ($10^{6.6}$ Pa.s) and drawn under a tensile load, then the microphases tend to elongate. It was recognized that upon elongation, the phase separated glass would transition from opaque to transparent along the drawing axis, yielding *waveguide-like* properties [97], even so far as to be considered a "pseudo fiber optic device" [98]. In this era of fiber optics however, considerable efforts were focused on attaining exceptionally low-loss optical fiber [99] and consequently, fabrication techniques necessary to obtain the same [100,101]. Much of the fiber community was focused on eliminating impurities in optical fiber [99] thereby avoiding phase separation. Some work was done in the following years investigating the anomalous birefringence in these glasses by renown glass scientists Prof. Minoru Tomozawa (Rensselaer Polytechnic Institute, Troy, NY) and Arun Varshneya (Alfred University, Alfred, NY) [102,103], though it would be many years before this work would be translated into possible Anderson-like waveguiding [93].

An early attempted demonstration of a TALOF was by Persch, *et al.*, in 2004 [104]. Standard telecommunications-grade optical fiber was stacked in a hollow-preform to form a hexagonal array and was drawn down to an all-solid fiber forming a transversely disordered array of cores. The resulting fiber possessed an average core-to-core spacing (Λ) of 12.1 μm with an average core diameter of 6.9 μm and was found to be longitudinal invariant over several meters. The refractive index difference between the core and the glass matrix was determined to be $\Delta n \approx 0.00384$. TAL however was not realized in this fiber. Both the Λ and the core diameters are significantly larger than the excitation wavelength used (800 nm) and the refractive index difference was likely too low.

The first observation of TAL of light was by Schwartz, *et al.*, in 2007 [105] within a disordered (planar) photonic lattice produced using a photorefractive crystal. To construct the transversely disordered lattice, an optical induction technique was used which transforms an optical interreference pattern into localized random fluctuations in the refractive index of the material. This permitted studies of the influences of the strength of disorder on the beam localization radius, since the degree of disorder (Λ, site dimensions, fill ratio) could easily be altered. While this technique offered a straightforward method to controlling the level of disorder present within the crystal, only weak localization was observed due to the low index difference obtained in the random fluctuations ($\Delta n = 0.0002$). Even demonstrating weak localization sparked a resurgence in TAL of light, bringing forth experimental evidence to validate the theory produced more than 25 years earlier.

The first observation of TAL in an optical fiber was by Prof. Arash Mafi's research group from the University of New Mexico (UNM) in 2012 with the development of a polymer TALOF [22]. 80,000 total fibers of polystyrene (PS, $n = 1.59$) and polymethylmethacrylate (PMMA, $n = 1.49$) were randomly mixed together, maintaining a 50% fill ratio of high-index to low-index sites. This bundle was drawn to an air-clad, transversely disordered optical fiber. The overall dimensions of the fiber were sufficiently large so that the boundary effects of the air-clad had no effects on the beam localization. The site sizes in the final fiber were on the order of the wavelength of light (~ 0.9 μm) with the two polymers chosen such that $\Delta n = 0.1$. The influence of each of these parameters on the beam localization length is theoretically investigated in a follow-up review [95]. This demonstrated the first flexible TALOF, which was used to investigate single-fiber beam multiplexing [78] and image transport properties of TALOF [76]. The image transport quality of this TALOF was equivalent to if not better than image transport of commercial fiber bundles [76].

In the same year, Prof. Mafi's group observed TAL in a glass-air optical fiber derived from an elongated "satin quartz" artisan glass rod, fabricated by Prof. John Ballato's group at Clemson University [106]. The starting rod was drawn from an 8 mm outer diameter porous silica rod to about a 250 μm air-clad disordered fiber. The air holes were shown to elongate [107] over sufficient distances for light to propagate. The average fill-fraction of air-to-silica was low, about 5.5% and the air-hole diameters varied from 0.2 to 5.5 μm. The high index contrast between silica and air ($\Delta n \approx 0.5$) provided sufficient scattering strength for TAL to be observed even though some of the other microstructural properties were suboptimal. Localization was only observed along the periphery of the fiber where the average fill-ratio of air-to-silica was higher. Lasing was investigated in this fiber by filling the air capillaries of a 10 cm long piece with a rhodamaine 640 dye solution. The dye filled piece was pumped with a frequency doubling Nd:YAG and directional random lasing was observed [79].

In 2014, research scientists Chen and Li from Corning Inc. reported TAL in a glass optical fiber with random airlines in the core [108] following a technique used to develop "bend-insensitive" optical fibers [42]. The bulk preform was developed using an Outer Vapor Deposition (OVD) process [100]. Pure silica soot layers were deposited and then sintered in an 100% N_2 environment. During this sintering stage, N_2 gas becomes trapped in the silica blank, leaving randomly distributed air holes. The "porous" sintered preform is then drawn to fiber. Similar to the satin quartz rod, the air-holes are elongated during fiber drawing. Multiple fibers were drawn with this technique to varying outer diameters to investigate the impact on the void sizes and localization strength. The average air-hole diameter in all fiber sizes ranged from 180-390 nm and the average air fill-fraction was slightly greater than 1% (varying from 1.3% along the fiber edge, to 0.9% in the center). Interestingly, even with the low air fill-fraction, transverse Anderson localization of light was observed even in the center of the fiber, contrary to the satin quartz derived fiber of Karbasi, *et al.* [106]. Chen and Li attribute this discrepancy to the differences in air-line diameters, density, and length (or longitudinal invariance), though the latter two are not reported in either of their References [106,108].

Intrinsic to the fabrication process, no air-lines were present in the center of the fiber. The OVD process deposits silica soot on the outside of a solid silica substrate rod. During the nitrogen-rich sintering stage, the center portion is already solid and therefore unable to trap the gas bubbles. It is generally expected that Anderson localization becomes weaker with reduced material disorder (e.g. smaller air fill-fraction), though in the fibers of Chen and Li, this seems to not be the case. Strong waveguiding (localization) is observed in the fiber center (where no air holes are present) which raises an interesting question; are there interactions between Anderson localization and other waveguiding phenomena (i.e. total internal reflection) and is it possible for these various waveguiding mechanisms to coexist within the same fiber? Or was their assertion of TAL incorrect? This remains a topic of discussion.

In 2016, Prof. Yasutake Ohishi’s group from the Toyota Technological Institute in Japan reported the fabrication of the first all-solid glass disordered optical *rod* exhibiting transverse Anderson localization of light [109]. The rod was fabricated by stacking and drawing thousands of fibers derived from two tellurite-based bulk glass compositions. A few years later, Prof. Ohishi’s group reported the fabrication of the first all-solid disordered glass optical *fiber* exhibiting TAL using this same technique [110]. The only difference between the rod and fiber designation is the measured outer diameter. Both the rod and fiber were derived from the same two bulk glass compositions, the first of the glasses comprising of TeO_2, Li_2O, WO_3, MoO_3, and Nb_2O_5 (TLWMN) and the second being TeO_2, ZnO, Na_2O, and La_2O_3 (TZNL). Both glasses were made using conventional batch melting techniques and separate rods (of unspecified dimensions) were formed from each. The rods were drawn to a diameter of 150 μm and cut to pieces approximately 15 cm in length. About 9,000 total pieces (4,500 from each glass) were mixed together maintaining the 0.5 fill ratio. This bundle was fused and drawn to a 200 μm disordered fiber, which was cut into pieces being 15 cm in length. These disordered fibers were sleeved in a TZNL overclad tube to be drawn to the final *rod* with an outer diameter of 3.6 mm. The *fiber* was comprised of the same TLWMN and TZNL glasses, only the final diameter was 125 μm instead of 3.6 mm. Multiple drawing steps were necessary to ensure the final site size was ~1 μm. At λ = 1550 nm, the refractive index difference in the bulk glasses was measured to be 0.09, and transverse Anderson localization of light was realized. Rather interesting near-IR image transport of three vertical slits was demonstrated with this fiber portraying the capabilities of TALOF at wavelengths beyond the visible spectrum [110]. Recently, Prof. Ohishi's group numerically investigated the localization of infrared light in transversely disordered arsenic selenide-based glasses [111] suggesting the possibility of future chalcogenide glass-based TALOFs for high resolution infrared image transmission.

In 2017, Prof. Axel Schülzgen's group from the University of Central Florida (UCF) demonstrated the fabrication of a TALOF using a combination of silica rods and tubes stacked in an overclad tube to develop glass-air disordered optical fiber [112,113]. The fabrication process for these fibers is not well described in the literature. The disordered core region was 278 μm with an overclad diameter of 414 μm. The air fill-ratio was 28.5% with air holes ranging from 0.64 μm^2 to 100 μm^2. Compared to the previous silica-air disordered fibers, this fiber possessed a significantly higher fill-ratio with noticeably larger air-sites, and fairly low loss (< 1 dB/m) which is likely due to a longer longitudinal invariance and lower losses of the presumably telecom-grade silica glass employed. These attributes, coupled with the large index difference between silica and air, led to strong transverse localization of the input beam, permitting high quality image transport over decently long lengths (> 1 m) [113]. Coupled with a deep learning technique called the convolutional neural network, Prof. Schülzgen's group has demonstrated high quality bend-independent image transport in these transversely disordered glass optical fibers [114].

I. C. Optical fiber fabrication (methods specific to this Dissertation)

Glass fiber fabrication techniques have evolved tremendously over time. Originally drawn with rudimentary techniques such as molding a strand of glass from a molten batch to the back of an arrow and firing across the room [115], silica-based fibers have become some of the few materials containing properties all-but matching their theoretical values [116]. Several vapor deposition techniques have arisen for the development of low-loss optical fibers comprised of the core/clad construct, such as Outside Vapor-Phase Oxidation (OVPO or OVD for Outside Vapor Deposition) [117], Modified Chemical Vapor Deposition (MCVD) [118], and Vapor Axial Deposition (VAD) [101]. Despite the success of these conventional techniques for developing low-loss optical fiber, they are scarcely used when developing specialty fibers due to limited geometric (fiber design) capabilities and breadth of dopants into silica and their respective concentrations. Thus, unconventional techniques are necessary and will be investigated for the development of TALOFs. While some vapor deposition techniques can be used, as Chen and Li have shown with their clever adaptation of the OVD technique, higher dopant concentrations and precisely engineered MOF have been developed with more unconventional techniques.

The principal technique used throughout this dissertation is the molten core method (MCM) [119]. Generally, the precursor core material (e.g. powder or crystal) is inserted into a silica-based capillary preform. The preform is loaded into an optical fiber draw tower and heated to a temperature where the precursor becomes molten and the fiber is drawn. Inherently, the molten core dissolves the surrounding cladding material, forming a silicate core often with 15-20 molar percent of the initial dopant remaining [120,121]. Through careful selection of the precursor material, a secondary phase can be incorporated into the core through liquid-liquid phase separation occurring during the fabrication process. Though not desirable for most specialty fibers, such a secondary phase, depending on its refractive index properties, size, and distribution, could be of value to novel TALOFs. In order for Anderson-localized propagation along the fiber, the microphases need to be elongated [98]. In an attempt to elongate the formed microphases during fiber drawing, a secondary step to the MCM can be included. For this extended MCM, a large diameter sample is drawn with a precursor composition such that the core becomes phase separated upon solidifying. This sample is then redrawn at a significantly lower temperature such that radial forces experienced by the fiber during drawing are translated to the microphases and they elongate.

An alternative method of fiber fabrication was investigated as well, specifically a variation of the stack-and-draw technique used in making multi-core optical fiber [122]. For the stack-and-draw process, glass fibers, rods, or tubes are stacked in a hollow-core preform or overclad tube and the bundle is drawn to fiber. Since the volume of the fibers is comprised mostly of silica, the viscosity difference between the cores and the cladding is negligible and the fiber is drawn with the cores retaining their initial shape with minor deformations. Generally, holes are drilled into the preform in the desired geometry to make the stacking process more straightforward. When designing the fiber, the desired light guiding mechanism determines the fiber geometry and precursor material used.

Recently, TALOF have been developed using this stack-and-draw technique utilizing rods of two different glass compositions composition [109] or hollow silica tubes [113]. Throughout this dissertation, many of the precursor fibers used for the stack-and-draw methodology are MCM derived core/clad optical fibers. Semiconductor core fibers developed using the reactive molten core method were explored and challenges presented. Finally, doped-silica tubes developed using the modified chemical vapor deposition (MCVD) lathe were stacked to introduce air disorder into the microstructure. Through careful manipulation of the fiber draw conditions (draw temperature, speed, applied vacuum), all-solid and air-disordered fibers can be developed.

I. D. Aims of this Dissertation

The research on TALOFs to date has focused primarily on the fabrication techniques for silica and air disordered fibers and various applications that have resulted from fibers developed. Little work has been done on the material developments of TALOFs outside of the tellurite and chalcogenide fibers of Prof. Ohishi. The purpose of this dissertation is to advance the knowledge of the material influences on TALOF (e.g. the impact active or highly-nonlinear dopants in silica on TALOF), some of which has been published in literature [123-125]. It is noted that before many material properties can be studied, a fiber fabrication process for drawing these fibers first needs to be engineered. Much of this dissertation explores and adapts different fiber fabrication methods in an attempt to establish concrete methods of engineering TALOFs. Not all the methods described herein directly yielded optical fibers exhibiting waveguiding by TAL, however it remains necessary for future scientists/scholars who may be studying material properties of TALOF to understand fiber fabrication methods that have worked, and especially those that have not.

For completeness, *fibers* generally have an outer diameter of 1 mm or less, whereas *canes* are greater than 1 mm [126]. It is worth noting that the intent of this dissertation is to develop and investigate an Anderson localizing optical fiber *waveguide*, notwithstanding the overall dimensions. Oftentimes a large core diameter is necessary for Anderson localization to be observed at long lengths to mitigate the boundary effects (cladding induced reflection). Experimentally, it is sometimes simpler to begin with a large-core-diameter cane possessing sufficient cladding to ensure mechanical durability of the sample. Inasmuch, many chapter and section titles include “fiber” in the nomenclature. This is merely used to describe the family of material under consideration. Finally, some of the fibers/canes developed throughout this dissertation were transversely disordered optical fiber (TDOF) but may not necessarily have been transverse Anderson localizing optical fiber (TALOF).

The remainder of this Dissertation is organized as follows. Chapter II explores the possibility of utilizing *in-situ* phase separation within a glass optical fiber drawn with the MCM to as a method of developing TALOFs. Chapter III utilizes an alternative method of fiber fabrication, specifically the stack-and-draw technique, and compares the microstructure and resulting optical properties with the phase separated fiber counterparts. Once a fiber fabrication technique has been established, Chapter IV introduces the material development for novel actively doped transverse Anderson localizing optical fiber (Yb^{3+} and Er^{3+} separately) and discusses the respective lasing / amplification characteristics. Chapter V investigates the presence of optical nonlinearities in these TALOFs through the realization of small modal effective areas (less than 40 μm^2 in a 150 μm diameter core) resulting from the strong localization. Finally, Chapter VI provides an overview of the findings within this dissertation, describes fabrication challenges encountered throughout, and provides suggestions for future directions of this research.

I. E. References

[1] B. Flusberg, E. Cocker, W. Piyawattanametha, J. Jung, E. Cheung, and M. Schnitzer, “Fiber-optic fluorescence imaging,” *Nature Methods* **2**, 941-950 (2005).

[2] A. Aravanis, L.-P. Wang, F. Zhang, L. Meltzer, M. Mogri, M. B. Schneider, and K. Deisseroth, “An optical neural interface: in vivo control of rodent motor cortex with integrated fiberoptic and optogenetic technology,” *Journal of Neural Engineering* **4**(3), S143-S156 (2007).

[3] D. R. Sparta, A. M. Stamatakis, J. L. Phillips, Nanna Hovelsø, R. van Zessen, and G. D. Stuber, “Construction of implantable optical fibers for long-term optogenetic manipulation of neural circuits,” *Nature Protocols* **7**, 12-23 (2012).

[4] G. Keiser, *Optical fiber communications 2nd edition* (Singapore: McGraw-Hill Book Co. 1991).

[5] S. Personick, *Fiber Optics: Technology and Applications* (Springer Science, 1985).

[6] S. Zhang, F. Yaman, Y.-K. Huang, J. D. Downie, D. Zou, W. A. Wood, A. Zakharian, R. Khrapko, S. Mishra, V. Nazarov, J. Hurley, I. B. Djordjevic, E. Mateo, and Y. Inada, “Capacity-Approaching Transmission over 6375 km at Spectral Efficiency of 8.3 bit/s/Hz,” Optical Fiber Communications Conference and Exhibition, paper Th5C.2 (2016).

[7] F. Gunning, and B. Corbett, “Time to Open the 2-μm Window?” *Optics and Photonics News*, 42-47 (March 2019).

[8] P. Dragic, M. Cavillon, and J. Ballato, “Materials for optical fiber lasers: A review,” *Applied Physics Review* **5**(4), 041301 (2018).

[9] D. J. Richardson, J. Nilsson, and W. A. Clarkson, “High power fiber lasers: current status and future perspectives,” *Journal of the Optical Society of America B* **27**(11), B63-B92 (2010).

[10] C. Baker, E. J. Friebele, A. A. Burdett, D. L. Rhonehouse, J. Fontana, W. Kim, S. R. Bowman, L. B. Shaw, J. Sanghera, J. Zhang, R. Pattnaik, M. Dubinksii, J. Ballato, C. Kucera, A. Vargas, A. Hemming, N. Simakov, and J. Haub, “Nanoparticle doping for high power fiber lasers at eye-safer wavelengths,” *Optics Express* **25**(12), 13903-13915 (2017).

[11] G. Agrawal, *Nonlinear fiber optics 2nd edition*, (San Diego, CA: Academic Press, Inc. 1995).

[12] K. Oh, and U.-C. Park, *Silica Optical Fiber Technology for Devices and Components* (Hoboken, NJ: Wiley, 2012).

[13] G. Agrawal, “Nonlinear fiber optics: its history and recent progress,” *Journal of the Optical Society of America B* **28**(12), A1-A10 (2011).

[14] T. Baer and F. Schlachter, “A report to the OSTP – Lasers in Science and Industry,” June 15, 2010.

[15] E. Snitzer, and H. Osterberg, “Observed dielectric waveguide modes in the visible spectrum,” *Journal of the Optical Society of America* **51**(5), 499-505 (1961).

[16] J. Senior, *Optical Fiber Communications 3rd edition*, (England: Pearson Educated Limited, 2009).

[17] M. Zervas, and C. Codemard, “High Power Fiber Lasers: A Review,” *IEEE Journal of Selected Topics in Quantum Electronics* **29**(5), 0904123 (2014).

[18] M. Chen, M.-J. Li, and J. S. Stone, Multicore optical fiber with a randomized core structure, US Patent Application US2017/0123146 (2017).

[19] Y. Hua, E. Makrides-Saravanos, and M.-J. Li, Airline optical fiber with reduced multipath interference and methods of forming the same, US Patent 7,542,654 B1 (2009).

[20] P. Russell, "Photonic crystal fibers," *Science* **299**(5605), 358-362 (2003).

[21] D. J. Richardson, J. M. Fini, and L. E. Nelson, "Space-division multiplexing in optical fibres," *Nature Photonics* **7**, 354-362 (2013).

[22] S. Karbasi, C. Mirr, P. G. Yarandi, R. Frazier, K. Kock, and A. Mafi, "Observation of transverse Anderson localization in an optical fiber," *Optics Letters* **37**(12) 2304-2306 (2012).

[23] J. Ballato, and A. Peacock, "Perspective: Molten Core optical fiber fabrication – A Route to new materials and applications," *APL Photonics* **3**, 120903 (2018) https://doi.org/10.1063/1.5067337

[24] J. Ballato, and E. Snitzer, Fabrication of fibers with high rare-earth concentrations for Frarday isolator applications," *Applied Optics* **34**(30), 6848-6854 (1995).

[25] P. Dragic, T. Hawkins, P. Foy, S. Morris, and J. Ballato, "Sapphire-derived all-glass optical fiber," *Nature Photonics* **6**(9), 627-633 (2012).

[26] A. Mangognia, C. Kucera, J. Guerrier, J. Furtick, T. Hawkins, P. Dragic, and J. Ballato, "Spinel-derived single-mode optical fiber," *Optical Materials Express* **3**(4), 511-518 (2013).

[27] J. Ballato, T. Hawkins, P. Foy, B. Kokuoz, R. Stolen, C. McMillen, M. Daw, Z. Su, T. M. Tritt, M. Dubinskii, J. Zhang, T. Sanamyan, and M. J. Matthewson, "On the

fabrication of all-glass optical fibers from crystals," *Journal of Applied Physics* **105**(5), 053110 (2009).

[28] J. Ballato, T. Hawkins, P. Foy, R. Stolen, B. Kokuoz, M. Ellison, C. McMillen, J. Reppert, A. M. Rao, M. Daw, S. Sharma, R. Shori, O. Stafsudd, R. R. Rice, and D. R. Powers, "Silicon optical fiber," *Optics Express* **16**(23), 18675-18683 (2008).

[29] J. Ballato, T. Hawkins, P. Foy, B. Yazgan-Kokuoz, R. stolen, C. McMillen, N. K. Hon, B. Jalali, and R. Rice, "Glass-clad sincle-crystal germanium optical fiber," *Optics Express* **17**(10) 8029-8035 (2009).

[30] M. Tuggle, C. Kucera, T. Hawkins, D. Sligh, A. F. J. Runge, A. C. Peacock, P. Dragic, and J. Ballato, "Highly nonlinear yttrium-aluminosilicate optical fiber with a high intrinsic stimulated Brillouin scattering threshold," *Optics Letters* **42**(23), 4849-4852 (2017).

[31] N. Yu, M. Cavillon, C. Kucera, T. W. Hawkins, J. Ballato, and P. Dragic, "Less than 1% Quantum defect fiber lasers via ytterbium-doped multicomponent fluorosilicate optical fiber," *Optics Letters* **43**(13), 3096-3099 (2018).

[32] G. Li, N. Bai, N. Zhao, and C. Xia, "Space-division multiplexing: the next frontier in optical communication," *Advances in Optics and Photonics* **6**(4), 413-487 (2014).

[33] R. G. H. van Uden, R. A. Correa, E. A. Lopez, F. M. Huijskens, C. Xia, G. Li, A. Schülzgen, H. de Waardt, A. M. J. Koonen, and C. M. Okonkwo, "Ultra-high-density spatial division multiplexing with a few-mode multicore fibre," *Nature Photonics* **8**, 865-870 (2014).

[34] T. Birks, B. Mangan, A. Diez, J. Cruz, and D. Murphy, "Photonic lantern spectral filters in multi-core fibre," *Optics Express* **20**(13), 13996-14008 (2012).

[35] A. Valazquez-Benitez, J, E. Antonio-Lopez, J. C. Alvarado-Zacarias, N. K. Fontaine, R. Ryf, H. Chen, J. Hernadez-Cordero, P. Sillard, C. Okonkwo, S. G. Leon-Saval, and R. Amezcua-Correa, "Scaling photonic lanterns for space-division multiplexing," *Scientific Reports* **8**, 8897 (2018).

[36] H. H. Hopkins, and N. S. Kapany, "A flexible fiberscope, using static scanning," *Nature* **173**, 39-41 (1954).

[37] K. L. Reichenbach, and C. Xu, "Numerical analysis of light propagation in image fibers or coherent fiber bundles" *Optics Express* **15**, 2151–2165 (2007).

[38] B. J. Eggleton, C. Kerbage, P. S. Westbrook, R. S. Windeler, and A. Hale, "Microstructured optical fiber devices," *Optics Express* **9**(13), 698-713 (2001).

[39] F. Kong, G. Gu, T. Hawkins, M. Jones, J. Parsons, M. Kalichevsky-Dong, B. Pulford, I. Dajani, and L. Dong, "~900W single-mode CW power from an 60μm-core Ytterbium-doped all-solid photonic bandgap fiber laser," OSA Technical Digest Frontiers in Optics 2016, paper FW5B.3

[40] J. K. Ranka, R. S. Windeler, and A. J. Stentz, "Visible continuum generation in air-silica microstructure optical fibers with anomalous dispersion at 800nm," *Optics Letters* **25**(1), 25-27 (2000).

[41] W. S. Wong, X. Peng, J. M. McLaughlin, and L. Dong, "Breaking the limit of maximum effective area for robust single-mode propagation in optical fibers," *Optics Letters* **30**(21), 2855-2857 (2005).

[42] M. -J. Li, P. Tandon, D. C. Bookbinder, S. R. Bickham, M. A. McDermott, R. B. Desorcie, D. A. Nolan, J. J. Johnson, K. A. Lewis, and J. J. Englebert, "Ultra-low bending loss single-mode fiber for FTTH," *Journal of Lightwave Technology* **27**(3), 376-382 (2009).

[43] T. A. Birks, P. J. Roberts, P. St. J. Russell, D. M. Atkin, and T. J. Shepherd, "Full 2-D photonic bandgap in silica/air structures," *Electronics Letters* **31**(22), 1941-1943 (1995).

[44] J. C. Knight, T. A. Birks, P. St. J. Russell, and D. M. Atkin, "All-silica single-mode optical fiber with photonic crystal cladding," *Optics Letters* **21**(19), 1547-1549 (1996).

[45] T. A. Birks, J. C. Knight, and P. J. Russell, "Endlessly single-mode photonic crystal fiber," *Optics Letters* **21**(19), 941-963 (1997).

[46] L. Dong, H. A. McKay, and L. Fu, "All-glass endless single-more photonic crystal fibers," *Optics Letters* **33**(21), 2440-2442 (2008).

[47] T. A. Birks, J. C. Knight, B. J. Mangan, and P. St. J. Russell, "Photonic Crystal Fibers: An Endless Variety," *IEICE Transactions on Communications* **E84B**(5), 1211-1218 (2001).

[48] L. Dong, J. Li, and X. Peng, "Bend-resistant fundamental mode operation in ytterbium-doped leakage channel fibers with effective areas up to 3160μm^2," *Optics Express* **14**(24), 11512-11519 (2006).

[49] L. Dong, and X. Peng, Rare earth doped and large effective area optical fibers for fiber lasers and amplifiers, US Patent 8,213,758-B2 (2007).

[50] C. Jauregui, H.-J. Otto, F. Stutzki, F. Jansen, J. Limpert, and A. Tunnermann, “Passive mitigation strategies for mode instabilities in high-power fiber laser systems,” *Optics Express* **21**(16), 19375-19386 (2013).

[51] L. Fu, B. K. Thomas, and L. Dong, “Efficient supercontinuum generations in silica suspended core fibers,” *Optics Express* **16**(24), 19629-19642 (2008).

[52] A. Ruehl, M. J. Martin, K. C. Cossel, L. Chen, H. McKay, B. Thomas, C. Benko, L. Dong, J. M. Dudley, M. E. Fermann, I. Hartl, and J. Ye, “Ultrabroadband coherent supercontinuum frequency comb,” *Physical Review A* **84**(1), 011806 (2011).

[53] J. C. Knight, J. Broeng, T. A. Birks, and P. St. J. Russell, “Photonic band gap guidance in optical fibers,” *Science* **282**, 1476-1478 (1998).

[54] F. Kong, K. Saitoh, D. Mcclane, T. Hawkins, P. Foy, G. Gu, and L. Dong, “Mode area scaling with all-solid photonic bandgap fibers,” *Optics Express* **20**(24), 26363-26372 (2012).

[55] F. Luan, A. K. George, T. D. Hedley, G. J. Pearce, D. M. Bird, J. C. Knight, and P. St. J. Russell, “All-solid photonic bandgap fiber,” *Optics Letters* **29**(20), 2369-2371 (2004).

[56] R. F. Cregan, B. J. Mangan, J. C. Knight, T. A. Birks, P. St. J. Russell, P. J. Roberts, and D. C. Allan, “Single-mode photonic band gap guidance of light in air,” *Science* **285**, 1537-1539 (1999).

[57] R. J. Roberts, F. Couny, H. Sabert, B. J. Mangan, D. P. Williams, L. Farr, M. W. Mason, A. Tomlinson, T. A. Birks, J. C. Knight, and P. St. J. Russell, “Ultimate low loss of hollow-core photonic crystal fibres,” *Optics Express* **13**(1), 236-244 (2005).

[58] C. M. Smith, N. Venkataraman, M. T. Gallagher, D. Muller, J. A. West, N. F. Borrelli, D. C. Allen, and K. W. Koch, “Low-loss hollow-core silica/air photonic bandgap fibre,” *Nature* **424**, 657-658 (2003).

[59] X. Chen, M.-J. Li, N. Venkataraman, M. T. Gallagher, W. A. Wood, A. M. Crowley, J. P. Carberry, L. A. Zenteno, and K. W. Koch, “Highly birefringent hollow-core photonic bandgap fiber,” *Optics Express* **12**(16), 3888-3893 (2004).

[60] P. Yeh, A. Yariv, and E. Marom, “Theory of Bragg fiber,” *Journal of the Optical Society of America* **68**(9), 1196-1201 (1978).

[61] P. R. Villeneuve, and M. Piche, “Photonic band gaps in two-dimensional square and hexagonal lattices,” *Physical Review B* **46**(8), 4969-4972 (1992).

[62] F. Kong, C. Dunn, J. Parsons, M. Kalichevsky-Dong, T. W. Hawkins, M. Jones, and L. Dong, “Large-mode-area fibers operating near single-mode regime,” *Optics Express* **24**(10), 10295-10301 (2016).

[63] F. Kong, G. Gu, T. W. Hawkins, M. Jones, J. Parsons, M. Kalichevsky-Dong, S. Palese, E. Cheung, and L. Dong, “Efficient 240W single-mode 1018nm laser from an Ytterbium-doped 50/400μm all-solid photonic bandgap fiber,” *Optics Express* **26**(3), 3138-3144 (2018).

[64] C. Dunn, F. Kong, G. Gu, T. W. Hawkins, M. Jones, J. Parsons, M. Kalichevsky-Dong, A. Runnion, R. Salem, D. Liu, D. Gardner, P. Fendel, R. Synowicki, E. Cheung, and L. Dong, “Solid Tellurite optical fiber based on stack-and-draw method for efficient mid-infrared supercontinuum generation,” in *Advanced Photonics 2016 (IPR, NOMA,*

Sensors, Networks, SPPCom, SOF), OSA Technical Digest (online) (Optical Society of America, 2016), paper SoW3G.4.

[65] L. Dong, F. Kong, G. Gu, T. W. Hawkins, M. Jones, J. Parsons, M. Kalichevsky-Dong, and C. Dunn, "Progress and challenges in further power scaling of single-mode fiber lasers," in *Asia Communications and Photonics Conference 2016*, OSA Technical Digest (online) (Optical Society of America, 2016), paper AF4A.1.

[66] T. A. Birks, I. Gris-Sánchez, S. Yerolatsitis, S. G. Leon-Saval, and R. R. Thomson, "The Photonic lantern," *Advances in Optics and Photonics* **7**, 107-167 (2015).

[67] SCHOTT North America, An introduction to fiber optic imaging; https://www.us.schott.com/d/lightingimaging/2e22eb88-bab2-4256-92de-46df689b255d/schott-introduction-on-fiber-optics-imaging-english-16082018.pdf

[68] A. Orth, M. Ploschner, E. R. Wilson, I. S. Maksymov, and B. C. Gibson, "Optical fiber bundles: Ultra-slim light field imaging probes," *Science Advances* **5**, 1-10 (2019).

[69] J. M. Fini, B. Zhu, T. F. Taunay, M. F. Yan, and K. S. Adebin, "Crosstalk in multi-core optical fibres," in Proceedings of the European Conference on Optical Communications paper Mo.1.LeCervin.4 (IEEE, 2011).

[70] P. J. Winzer, A. H. Gnauck, A. Konczykowska, F. Jorge, and J.-Y. Dupuy, "Penalties from In-band crosstalk for Advanced Optical Modulation Formats," in Proceedings of the European Conference on Optical Communications paper Tu.5.B.7 (IEEE, 2011).

[71] B. Zhu, T. F. Taunay, M. F. Yan, J. M. Fini, M. Fishteyn, E. M. Monberg, and F. V. Dimarcello, “Seven-core multicore fiber transmissions for passive optical networks,” *Optics Express* **18**(11), 11117-11122 (2010).

[72] S. Matsuo, Y. Sasaki, T. Akamatsu, I. Ishida, K. Takenaga, K. Okuyama, K. Saitoh, and M. Kosihba, “12-core fiber with one ring structure for extremely large capacity transmission,” *Optics Express* **20**(27), 28398-28408 (2012).

[73] J. Sakaguchi, B. J. Puttnam, W. Klaus, Y. Awaji, N. Wada, A. Kanno, T. Kawanishi, K. Imamura, H. Inaba, K. Mukasa, R. Sugizaki, T. Kobayashi, and M. Watanabe, “19-core fiber transmission of 19x100x172-Gb/s SDM-WDM-PDM-QPSK signal at 305 Tb/s,” in Optical Fiber Communication Conference, OSA Technical Digest (CD) (Optical Society of America, 2012), paper PDP5C.1.

[74] Fujikura Standards Specifications sheet for Image Fibers, No. B-19DA001A; http://www.fujikura.co.jp/eng/products/optical/appliedoptics/03/__icsFiles/afieldfile/2019/05/14/B-19DA001A-Imagefibers_standard_specifications.pdf

[75] A. Lagendijk, B. van Tiggelen, and D. S. Wiersma, “Fifty-years of Anderson localization,” *Physics Today* **62**, 24–29 (2009).

[76] S. Karbasi, R. Frazier, K. Koch, T. Hawkins, J. Ballato, and A. Mafi, “Image transport through a disordered optical fiber mediated by transverse Anderson localization,” *Nature Communications* **5**, 3362 (2014).

[77] G. Ruocco, B. Abaie, W. Schirmacher, A. Mafi, and M. Leonetti, “Disorder-induced single-mode transmission,” *Nature Communications* **8**, 14571 (2017).

[78] S. Karbasi, K. W. Koch, and A. Mafi, “Multiple-beam propagation in an Anderson localized optical fiber,” *Optics Express* **21**, 305–313 (2013).

[79] B. Abaie, E. Mobini, S. Karbasi, T. Hawkins, J. Ballato, and A. Mafi, “Random lasing in an Anderson localizing optical fiber,” *Light: Science & Applications* **6** (2017)

[80] P. W. Anderson, “Absence of diffusion in certain random lattices,” *Physical Review* **109**, 1492-1505 (1958).

[81] S. John, “Electromagnetic absorption in a disordered medium near a photon mobility edge,” *Physical Review Letters* **53**, 2169-2172 (1984).

[82] S. John, “Strong localization of photons in certain disordered dielectric superlattices,” *Physical Review Letters* **58**, 2486-2489 (1987).

[83] S. S. Abdullaev and F. K. Abdullaev, “On propagation of light in fiber bundles with random parameters,” *Radiofizika* **23**, 766–767 (1980).

[84] M. Segev, Y. Silberberg, and D. N. Christodoulides, “Anderson localization of light,” *Nature Photonics* **7**, 197-204 (2013).

[85] E. Abrahams, P. W. Anderson, D. C. Licciardello, and T. V. Ramakrishnan, “Scaling theory of Localization: Absence of quantum diffusion in two dimensions,” *Physical Review Letters* **42**(10), 673-676 (1979).

[86] H. Hu, A. Strybulevych, J. h. Page, S. E. Skipetrov, and B. A. van Tiggelen, “Localization of ultrasound in a three-dimensional elastic network,” *Nature Physics* **4**, 945-948 (2008).

[87] J. Billy, V. Josse, Z. Zuo, A. Bernard, B. Hambrecht, P. Lugan, D. Clement, L. Sanchez-Palencia, P. Bouyer, and A. Aspect, “Direct observation of Anderson localization of matter waves in a controlled disorder,” *Nature* **453**, 891-894 (2008).

[88] Elihu Abrahams, *50 Years of Anderson Localization* (Singapore: World Scientific Publishing Company), Chapter 1, pp 1-6 authored by P. Anderson.

[89] W. Schirmacher, B. Abaie, A. Mafi, G. Ruocco, and M. Leonetti, “What is the Right Theory for Anderson Localization of Light? An Experimental Test,” *Physical Review Letters* **120**, 067401 (2018)

[90] A. F. Ioffe, and A. R. Regel, *1960 Progress in Semiconductors* vol. 4. Editors: A. F. Gibson, F. A. Kroger and R. E. Burgess (London: Heywood) p.237

[91] H. De Raedt, A. Lagendijk, and P. de Vries, “Transverse localization of light,” *Physical Review Letters* **62**, 47–50 (1989).

[92] A. Mafi, “Transverse Anderson localization of light: a tutorial,” *Advances in Optics and Photonics* **7**, 459–515 (2015).

[93] A. Mafi, M. Tuggle, C. Bassett, E. Mobini, and J. Ballato, “Advances in the fabrication of disordered transverse Anderson localizing optical fibers,” *Optical Materials Express* **9**(7), 2769-2774 (2019).

[94] B. E. A. Saleh and M. C. Teich, *Fundamentals of Photonics*, 2nd ed. (Wiley Series in pure and applied optics. New York, NY: Wiley 2007).

[95] S. Karbasi, C. R. Mirr, R. J. Frazier, P. G. Yarandi, K. W. Koch, and A. Mafi, “Detailed investigation of the impact of the fiber design parameters on the transverse

Anderson localization of light in disordered optical fibers," *Optics Express* **20**, 18692–18706 (2012).

[96] T. Seward III, "Elongation and spheroidization of phase-separated particles in glass," *Journal of Non-Crystalline Solids* **15**, 487-504 (1974).

[97] T. Seward III, "Some unusual optical properties of elongated phases in glasses," *The Physics of Non-Crystalline Solids; Trans Tech Publications*: Aedermannsdorf, Switzerland pp. 342–347 (1977).

[98] L. Randall, and T. Seward III, Pseudo-fiber optic devices, US Patent 3,870,399 (1975).

[99] D. B. Keck, R. D. Maurer, and P. C. Schultz, "On the ultimate lower limit of attenuation in glass optical waveguides," *Applied Physics Letters* **22**(7), 307-309 (1973).

[100] D. Keck, P. Schultz, and F. Zimar, Method of forming optical waveguide fibers, US Patent 3,737,292 (1973).

[101] T. Izawa, T. Miyashita, and F. Hanawa, Continuous optical fiber preform fabrication method, US Patent 4,062,665 (1977).

[102] T. Takamori and M. Tomozawa, "Anomalous Birefringence in Oxide Glasses," *Treatise on Material Science and Technology* **12**, 123-155 (1977).

[103] A. Varshneya and K. Hosmer, "Anomalous Birefringence in discretely phase-separated glasses," *Journal of the American Ceramic Society* **72**(11), 2078-2083 (1989).

[104] T. Pertsch, U. Peschel, J. Kobelke, K. Schuster, H. Bartelt, S. Nolte, A. Tünnermann, and F. Lederer, "Nonlinearity and Disorder in fiber arrays," *Physical Review Letters* **93**(5), 053901 (2004).

[105] T. Schwartz, G. Bartal, S. Fishman, and M. Segev, “Transport and Anderson localization in disordered two-dimensional photonic lattices,” *Nature Letters* **446**, 52-55 (2007).

[106] S. Karbasi, T. Hawkins, J. Ballato, K. Koch, and A. Mafi, “Transverse Anderson localization in a disordered glass optical fiber,” *Optical Materials Express* **2**(11) 1496-1503 (2012).

[107] W. Blanc, M. Vermillac, F. Peters, C. Kucera, M. Tuggle, T. Hawkins, and J. Ballato, “Drawing optical fibers: elongating bubbles, breaking nanoparticles,” *OPAL,* May 2018, Barcelona, Spain. 2018.

[108] M. Chen and M.-J. Li, “Observing transverse Anderson localization in random air line based fiber,” *Proceedings Volume 8994, Photonic and Photonic Properties of Engineered Nanostructures IV*; 89941S (2014).

[109] T. Tuan, T. Cheng, S. Kuroyanagi, S. Tanaka, K. Nagasaka, T. Suzuki, and Y. Ohishi, “Fabrication of an all-solid tellurite disordered optical rod for transverse localization of light,” *Lasers Congress*, paper JTh2A.21 (2016).

[110] T. Tuan, S. Kuroyanagi, K. Nagasaka, T. Suzuki, and Y. Ohishi, “Characterization of an all-solid disordered tellurite glass optical fiber and its NIR optical image transport,” *Japanese Journal of Applied Physics* **58**, 032005 (2019).

[111] T. Suzuki, A. Nakatani, T. H. Tuan, and Y. Ohishi, “Numerical investigation on local confinement of infrared light on chalcogenide transversely disordered optical fibers,” *Proceedings of Optical Components and Materials XVI*, Vol. 10914 (2019).

[112] J. Zhao, J. E. Antonio-Lopez, R. A. Correa, A. Mafi, M. Windeck, and A. Schülzgen, “Image transport through silica-air random core optical fiber,” in *Conference on Lasers and Electro-Optics*, (Optical Society of America, 2017), p. JTu5A.91.

[113] J. Zhao, J. E. A. Lopez, Z. Zhu, D. Zheng, S. Pang, R. A. Correa, and A. Schülzgen, “Image transport through meter-long randomly disordered silica-air optical fiber,” *Scientific Reports* **8**, 3065 (2018).

[114] J. Zhao, Y. Sun, Z. Zhu, J. E. Antonio-Lopez, R. A. Correa, S. Pang, and A. Schülzgen, “Deep learning imaging through fully-flexible glass-air disordered fiber,” *ACS Photonics* **5**, 3930-3935 (2018).

[115] Jeff Hecht, *City of Light: The story of Fiber Optics*, (New York, NY: Oxford University Press, Inc. 1999)

[116] T. Miya, Y. Terunuma, T. Hosaka, and T. Miyashita, “Ultimate low-loss single-mode fibre at 1.55μm,” *Electronic Letters* **15**, 106-108 (1979).

[117] M. Blankenship, and C. Deneka, “The outside vapor deposition method of fabricating optical waveguide fibers*,” IEEE Journal of Quantum Electronics* **QE-18**, 1418-1423 (1982).

[118] J. MacChesney, and P. O’Connor, Optical fiber fabrication and resulting product. US Patent 4,217,027.

[119] S. Morris, and J. Ballato, “Molten-core fabrication of novel optical fibers,” *American Ceramic Society Bulletin* **92**, 24-29 (2009).

[120] M. Cavillon, J. Furtick, C. Kucera, C. Ryan, M. Tuggle, M. Jones, T. Hawkins, P. Dragic, and J. Ballato, "Brillouin Properties of a Novel Strontium Aluminosilicate Glass Optical Fiber," *Journal of Lightwave Technology* **34**, 1435-1441 (2016).

[121] M. Cavillon, P. Dragic, B. Faugas, T. W. Hawkins, and J. Ballato, "Insights and Aspects to the Modeling of the Molten Core Method for Optical Fiber Fabrication," *Materials* **12**(18), 2898 (2019).

[122] R. Fiacco, M. Hackert, D. Hawtof, and M. Van Ryn, Multicore glass optical fiber and methods of manufacturing such fibers, US Patent 6,154,594 (2000).

[123] M. Tuggle, C. Bassett, T. Hawkins, R. Stolen, A. Mafi, and J. Ballato, "Observation of optical nonlinearities in an all-solid transverse Anderson localizing optical fiber," *Optics Letters* **45**(3), 599-602 (2020).

[124] C. Bassett, M. Peysokhan, E. Mobini, M. Tuggle, J. Ballato, and A. Mafi, "Characterization of the Yb-doped glass Anderson localizing optical fiber," SPIE Photonics West, San Francisco, CA, February 3-6 (2020).

[125] A. Mafi, C. Bassett, M. Tuggle, M. Peysokhan, E. Mobini, and J. Ballato, "Optical pulse propagation in transverse Anderson localizing optical fibers," *Bulletin of the American Physical Society*, March 2-6, 2020.

[126] B. Faugas, T. Hawkins, C. Kucera, K. Bohnert, and J. Ballato, "Molten core fabrication of bismuth germanium oxide $Bi_4Ge_3O_{12}$ crystalline core fibers," *Journal of the American Ceramic Society* **101**(9), 4340-4349 (2018).

CHAPTER TWO

FABRICATION OF DISORDERED GLASS OPTICAL FIBERS

PART I – *In situ* PHASE SEPARATION

II. A. Introduction

This dissertation relates to understanding and advancing the necessary material microstructures for TAL in a light-guiding structure, such as an optical fiber. Since AL can be observed in the optics regime [1], herein, TAL will be described from an optics perspective. Through use of a melting technique, such as the Molten Core method (MCM) [2], *in situ* disordered glass fibers can be fabricated by exploiting the liquid-liquid phase separation phenomena. Phase separation is often regarded as detrimental in waveguiding structures as it yields poor optical properties due to the extensive scattering sites present in the system. However, upon post-processing, phase separated microphases in glass have been shown to elongate [3-5]. As described in Chapter I, the induced longitudinal invariance has introduced light guiding capabilities in certain glass systems [6], potentially exhibiting transverse Anderson localization *avant la lettre*.

The purpose of this Chapter is to evaluate the effectiveness of exploiting phase separation in glass as a means to develop transverse Anderson localizing optical fiber (TALOF) through a study of the resulting microstructure in phase separated optical fiber. Firstly, the molten core method will be introduced, and a preliminary material system will be investigated to obtain a phase separated glass optical fiber. Then the relationship between the microstructure and transmission properties will be discussed. As knowledge of the relationships between microstructure and localization tendencies was gained, post-processing techniques were developed to elongate the formed microphases in an attempt to obtain longitudinal invariance. Finally, as insights into the viscosity dependence of particle elongation became apparent, alternative material systems were investigated and are discussed.

II. B. Glass fiber fabrication using the Molten Core method

As discussed in Chapter I, a potential method for fabricating disordered optical fiber is through use of the MCM [2]. Precursor core materials (powder or crystalline rods) are prepared and inserted into a glass capillary preform. The loaded preform is transferred to an optical fiber draw tower and heated past the softening temperature of the silica-based cladding to be drawn to fiber. At this temperature, the core material becomes molten and dissolves some of the surrounding silica cladding, diluting the initial precursor mixture [7]. The high quenching rates (~2000°C/s) allow otherwise unstable silicates to form the core. This allows for a plethora of dopants to be utilized, including alkaline earth oxides (AEO) [8], alkali earth oxides [9], and rare-earth oxides (REO) [10], many of which exhibit liquid-liquid immiscibilities with silica. Using this technique, optical fibers can be fabricated yielding highly-doped silicate compounds that not are normally achievable through conventional vapor deposition methods, some with dopant concentrations in excess of 50 molar percent (mol%) [10].

If the initial material system exhibits liquid-liquid immiscibility with silica, *in situ* phase separation can occur within the core. This is due to the core composition shifting during the draw to higher silica concentrations oftentimes within the liquid-liquid immiscibility dome, leading directly to a phase separated core that is quenched into a solid when the fiber cools. Phase separation is not always detrimental for glass systems [11]. Manipulating the microstructure of the immiscible phases in these systems allows glass scientists to tailor material components of these systems, such as transparency [12], viscosity [13,14], and chemical durability [15].

Since phase separation corresponds with specific temperature and composition ranges (-TΔS) [16], the microstructure is directly related to the relative positioning within the immiscibility dome on phase diagrams. Compositions closer to the edge of the immiscibility dome often have finer microphases (~100 nm diameters) and those further towards the interior have larger microphases (~1 µm) [13]. It was originally believed that adding certain nucleating agents, such as P_2O_3, ZrO_2, or TiO_2 into a silicate glass melt will promote phase separation, due to the large ionic field strength possessed by said nucleating agents [17]. However, it was later shown that adding some of these minor constituents, such as ZrO_2 or TiO_2, actually mitigates phase separation in silicate systems. Looking at the Z/r component (with Z being valance electrons, and r being ionic radius) of ions becomes insufficient for determining phase separating tendencies of minor constituents. Further studies indicated the Z/a^2 component (with a being atomic separation) of ions is a better indication of phase separation tendencies. It was stated that if ions have a Z/a^2 value less than Si, they will mitigate phase separation in silicate systems, and if the ions have Z/a^2 values larger than Si, they will enhance phase separation. Certain dopants when added to these phase-separated silicate systems, such as

Al_2O_3 to decrease [18] or P_2O_5 to enhance [17] phase separation, can be used to tailor the overall microstructure.

Mechanical techniques, such as controlled elongation [3,4], can be used to modify the microstructure of formed microphases. At temperatures near the softening temperature of the glass ($10^{6.6}$ Pa.s, or ~1925°C for pure silica [19]), if an axial load is applied, the glass will elongate by viscous flow and will exert pressures on particles or microphases present within the glass, potentially yielding elongated microphases. For more information regarding the mechanisms of microphase elongation, T. Seward provides a thorough review of the phenomenon [5] providing both theory and experimental evidence. These elongated phases demonstrated “anomalous optical properties” of interest, such as birefringence [20], light guiding, and polarization [6].

A wealth of literature is available on phase separation tendencies of binary and ternary silicate glasses [2-6,11-15,17-25], including the (unintentional) fabrication of phase separated optical fibers using this molten core method [27] with AEO powder as a precursor. Many binary AEO-SiO_2 compositions phase separate at high silica concentrations [28]. Of these, magnesium oxide (MgO), calcium oxide (CaO), and strontium oxide (SrO) will be considered, due to availability and fewer safety concerns relative to the remaining AEOs.

A pure silica preform is generally drawn to fiber at temperatures between 1750°C – 2100°C (though it becomes difficult when drawing below 1800°C), a range that encompasses the entirety of the CaO-SiO_2 immiscibility dome [28]. This suggests microstructural tailorability in the final fiber as the dimensions of the formed microphases correspond to relative positions within the immiscibility dome. Therefore, CaO-SiO_2 is used as a preliminary system to begin investigating the microstructure of phase separated, highly disordered optical fiber. For convention, samples produced from a single oxide precursor will be known as “MO-derived” with M being the metal cation.

II. C. *In situ* phase separation

II. C. 1. Fabricating disordered optical fibers

Calcium oxide powder (Puratronic® 99.998% purity, provided by Alfa Aesar) was packed into a telecommunications grade silica capillary preform (3 mm inner / 30 mm outer diameter, provided by Heraeus). The packed preform was loaded into the optical fiber draw tower and subsequently drawn into cane (~150 μm core / 1.5 mm cladding diameter) at 2000°C. The feed rate and line speed were 2 mm/min and 0.8 m/min respectively. Sections of the resulting cane were scored using a ceramic tile and broken to produce a flat cross-section. These samples were polished to a 0.5 μm finish using SiC polishing pads. Additional samples were suspended longitudinally in an EpoKwick FC epoxy resin (Buehler) and polished to expose the core along the length of the fiber. Both the cross-section and longitudinal axis were analyzed under the Hitachi SU-6600 scanning electron microscope (SEM) operating at an accelerating voltage of 15 keV in variable pressure mode at 30 Pa and a working distance of 10 mm to verify phase separation and investigate longitudinal invariance (micrographs provided in Figure II.1). Physical properties of the microphases, such as diameter (Φ), fill-ratio, and pitch (Λ), were determined using ImageJ.

II. C. 2. Characterization of disordered optical fibers

Figure II.1 shows the highly disordered, phase separated core. The microphases are SiO_2-rich (dark) phases, and the matrix is CaO-rich (light) phase encompassing the microphases. The average microphase diameter varied radially, being 1.3 μm towards the edge and 0.9 μm towards the interior of the core. The average pitch (distance between nearest neighbors) was 0.7 μm and the fill-ratio of microphase to matrix was 0.32. Longitudinal analysis indicated no invariance as the microphases were spherical in shape. These values correspond to the cross-sections presented in Figures II.1 a-c but may not be representative of the entire fiber, due to the intrinsically random nature of phase separation.

Energy dispersive x-ray spectroscopy (EDX) was conducted using the Hitachi SU-6600 for compositional analysis to be used in refractive index calculations. For EDX, an electron beam interacts with the sample and excites electrons to higher energy states within the atoms. As the electrons relax, they emit characteristic x-rays that are detected and counted. The electrons from the beam scatter as they interact with the material, therefore the beam probes a volume of the material, regarded as a teardrop shape, collecting an average composition [29]. The teardrop diameter is dependent on the electron-beam energy, incident angle, and atomic density of the sample. The denser the material, the shorter the penetration depth and the smaller the teardrop diameter. As an example, the teardrop diameter for gallium arsenide (ρ = 5320 kg/m^3) at a given accelerating voltage is ~1 μm [30], so the teardrop diameter for fused silica (ρ = 2200 kg/m^3) at the same accelerating voltage will be larger. Within phase separated silicate

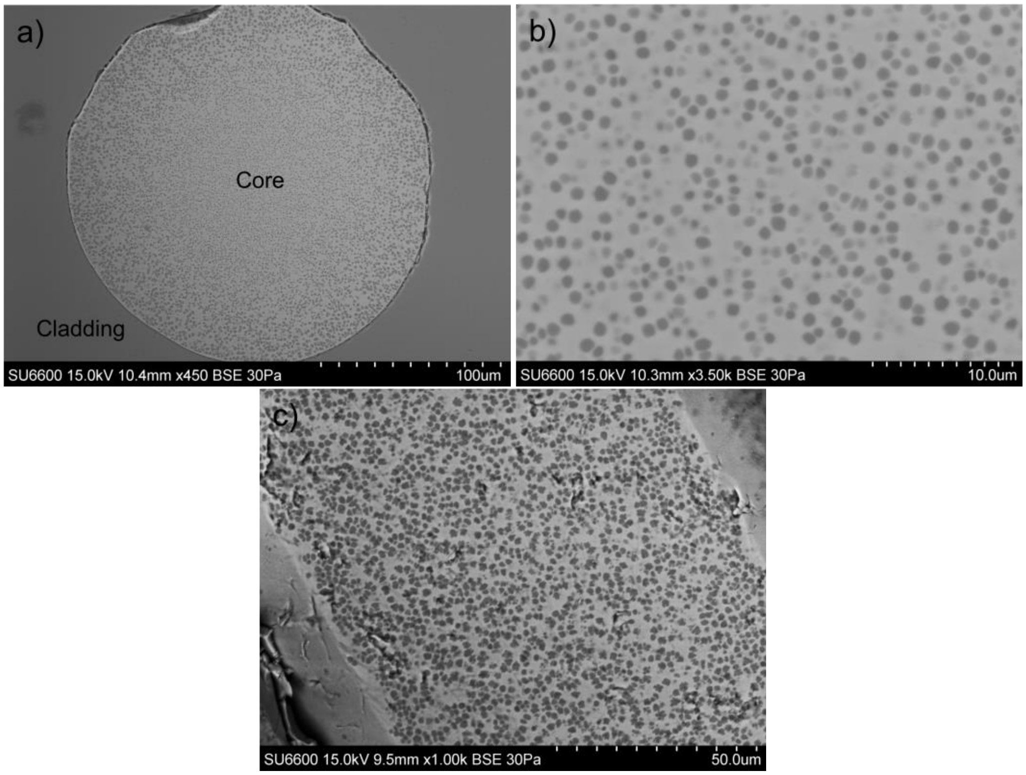

Figure II.1. SEM micrographs of phase separated, CaO-derived cane at a) 450x and b) 3500x. The matrix of the core is the lighter region and the microphases are the darker circular shapes. c) shows the longitudinal section of the cane at 1000x with distinct microphases.

glasses, the probing region of the electron beam is oftentimes larger than the observed microphases, thereby collecting counts from the surrounding matrix as well as the microphase, yielding inaccurate compositional data. Alternatively, if the sample is thin enough (< 100 nm), the electron beam cannot transversely scatter as widely, and the microphases may be analyzed.

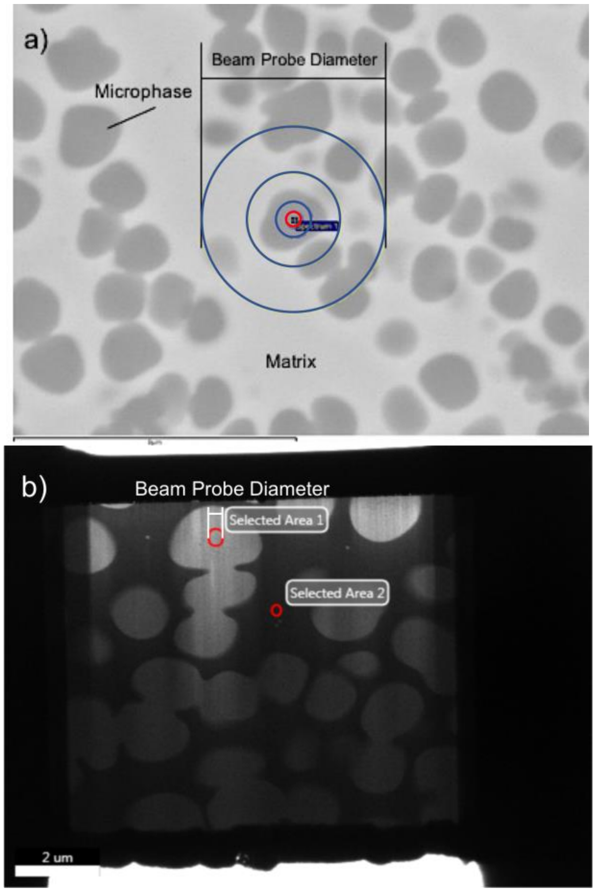

Figure II.2. SEM micrographs of CaO-derived optical fiber with a) was taken using the Hitachi SU-6600 and b) using the Hitachi NB5000 dual-beam after the sample was removed from the fiber and polished to a thickness of ~100 nm. Provided on both are the beam probe locations (red) and the probe diameter (outer blue ring for Figure a).

Using the Hitachi NB5000 dual-beam Focused Ion Beam (FIB) and Scanning / Transmission Electron Microscope (STEM), a 50 μm^2 region of the core was lifted out. The FIB bombards the sample with gallium ions, allowing for the precise fabrication of a micrometer-sized sample (10 μm x 5 μm). The sample is removed from the bulk using a probe, and subsequently ion polished to a thickness of less than 100 nm (a more detailed description of this process is provided in Appendix II.F.1). The sample is then analyzed using EDX for compositional data. This technique allows for more accurate compositional analysis as the beam probe diameter is less than 1 µm, instead of ~3.5 µm (Figure II.2). While this allows for a more precise compositional measurement (smaller probing area), the sample can be contaminated with gallium ions that may skew the actual composition.

The measured compositions are plotted against the CaO-SiO_2 phase diagram in Figure II.3. For a phase separated system, the composition of the two phases are (often) determined by an isothermal line intersecting either side of the immiscibility dome, with the intersection points being the respective compositions. Interestingly, this is only somewhat the case for the measured compositions. The slight discrepancy could be a result of the two compositions (CaO-rich matrix and SiO_2-rich microphase) having different fictive temperatures, thereby effectively solidifying at different temperatures, or the composition of the matrix varying radially in the core.

The refractive indices of the matrix and microphase were estimated to be 1.502 and 1.449 respectively, yielding an index difference (Δn) of 0.052. The refractive index values were calculated using an additivity model [32] given as:

$$n_{binary} = \mathrm{m}n_A + (1 - m)n_B \qquad (1)$$

n_{binary} is the refractive index of the binary system, m is the dimensionless volume fraction, and $n_{A/B}$ is the refractive index of pure material A or B. Furthermore, m is calculated using Equation 2:

$$m_A = \frac{\frac{M_A}{\rho_A}[C_A]}{\frac{M_A}{\rho_A}[C_A] + \frac{M_B}{\rho_B}[C_B]} \qquad (2)$$

with $M_{A/B}$ being the molar mass of component A or B in kg/mol, $\rho_{A/B}$ being the density of A or B in kg/m^3, and $[C_{A/B}]$ the molar composition in fraction or percent as a decimal.

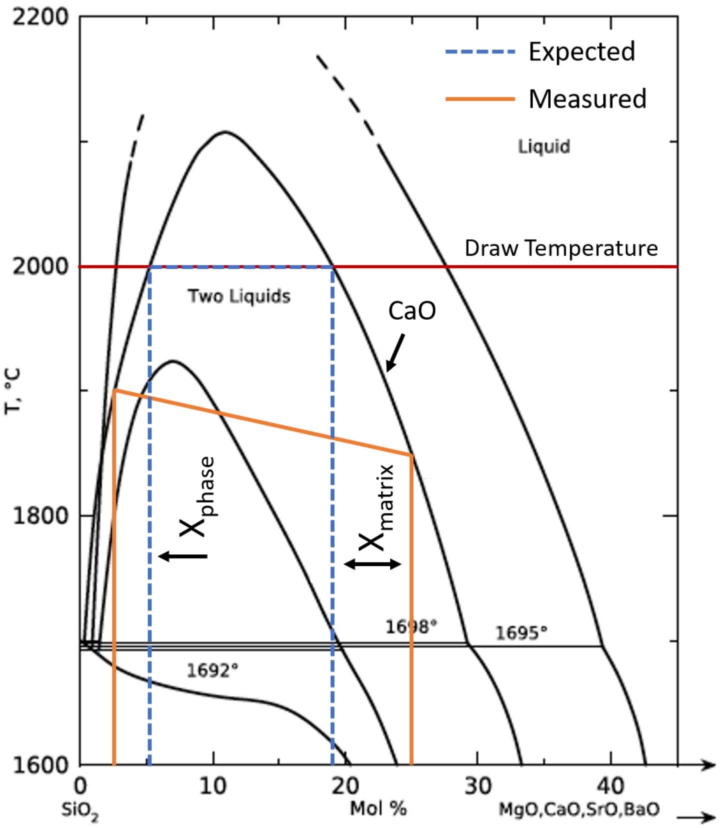

Figure II.3. Compositional phase diagram for the AEO-SiO_2 systems with emphasis on the immiscibility domes. Included is the draw temperature at 2000°C, the expected compositions (X_{matrix} and X_{phase}) at this temperature (blue, dashed) and the measured compositions (orange, solid). Adapted from [31].

Compositional data determined from the ion etched sample and estimated refractive indices are provided in Table II.1. The density and refractive index values used in the calculations are also provided. The refractive index and density values for amorphous fused silica and amorphous calcium oxide were given in [33] and [34] respectively. While there is quite a lot of variability reported for the density of amorphous CaO, for simplicity, the value used in the calculations was simply the one provided in Ref. 34.

Table II.1. Refractive index (n) data for CaO-derived cane with density (ρ) and molar mass (M) provided. Density was not determined for the matrix or the microphase.

	SiO_2 molar%	CaO molar%	n [λ = 1534 nm]	ρ [kg/m^3]	M [kg/mol]	References
Microphase	97.5	2.5	1.449	---	---	---
Matrix	74.1	25.9	1.502	---	---	---
SiO_2	100	0	1.444	2200	.06008	33
CaO	0	100	1.711	2608	.05608	34

Table II.2. A summary of the microstructural parameters of the CaO-derived cane compared against target values, including average microphase diameter (Φ, μm), average pitch (Λ, μm), the fill ratio, refractive index difference between the matrix and microphase (Δn), and longitudinal invariance. "Microstructural Requirements" deduced from a systematic study of fiber design parameters presented in Ref. [35].

	Φ [μm]	Λ [μm]	Fill Ratio	Δn	Longitudinal Invariance
CaO-derived	1.1	0.66	0.32	0.052	✗
Microstructural Requirements	1.00	1.00	0.50	0.100	✓

A comparison between the microstructural properties obtained with a phase separated system and the “ideal requirements” for TAL are provided in Table II.2.

II. C. 3. Transmission properties

Cane samples (~10 cm length segments) were sent to University of New Mexico (UNM) for Anderson localization testing. The samples were cleaved, polished, and then butt-coupled to a standard single mode telecommunications optical fiber (SMF-28) and analyzed using a He-Ne laser. The SMF-28 fiber is on a motorized stage that can move in the three Cartesian directions. The SMF-28 fiber is then moved to positions relative to the core and the light intensity is recorded from the output facet of the cane using a CCD camera beam profiler. Figure II.4 shows the output face of the disordered fiber having a light source input in various regions as indicated. There was no indication of transverse localization as no light was transmitted through the core. This is due to the lack of longitudinal invariance along the z-axis of the fiber, meaning any light entering the fiber scatters and experiences losses surpassing the initial intensity. This suggests light does not propagate to the end of the fiber sample and is most evident when the beam source enters the center of the fiber (Figure II.4.a). When the beam enters near the edge of the core (Figures II.4.b-e), light appears to propagate along the core/cladding interface (Figures II.4.c and II.4.e) and occasionally through the cladding (Figures II.4.b and II.4.d).

The disordered cane fabricated using *in situ* phase separation satisfied many requirements for transverse Anderson localization to be observed. The average microphase diameter and the average pitch were 1.1 and 0.7 μm respectively with a target value of 1 μm for both. The estimated index difference is lower than ideal, 0.052 when targeting 0.100, but this may be improved with utilizing a precursor system possessing a higher refractive index than calcium oxide. The limiting factor is the lack of longitudinal invariance. In order for light propagation to occur, and for TAL to be observed, it is imperative that longitudinal invariance exists.

II. D. Microphase elongation

It is suggested throughout literature that phase separation in glass can be controlled/tailored mechanically [3-6,21], or chemically through dopants [11-17]. Although certain dopants may increase phase separation tendencies in glasses [21] or increase the diameter of the formed microphases [24], they do not impact the spherical nature of the microphases. The minimization of surface energy leads to a spherical shape when formed in a liquid, i.e. liquid-liquid immiscibility. Since liquids are free to move and, therefore, do not support plastic deformation, the phase separated microstructure cannot elongate unless one or both phases are sufficiently viscous as to deform and elongate under strain. For longitudinal invariance, the formed microphases must be elongated in the z-direction. This can potentially be accomplished by mechanical elongation of the glass at a temperature near the softening viscosity (η) [5].

If a cylindrical rod in the glassy-state, and an axial load is applied to the rod at a temperature near the softening point (~$10^{6.6}$ Pa.s), it will elongate by viscous flow. If particles (nanoparticles, or phase separated microphases) are present within the glass

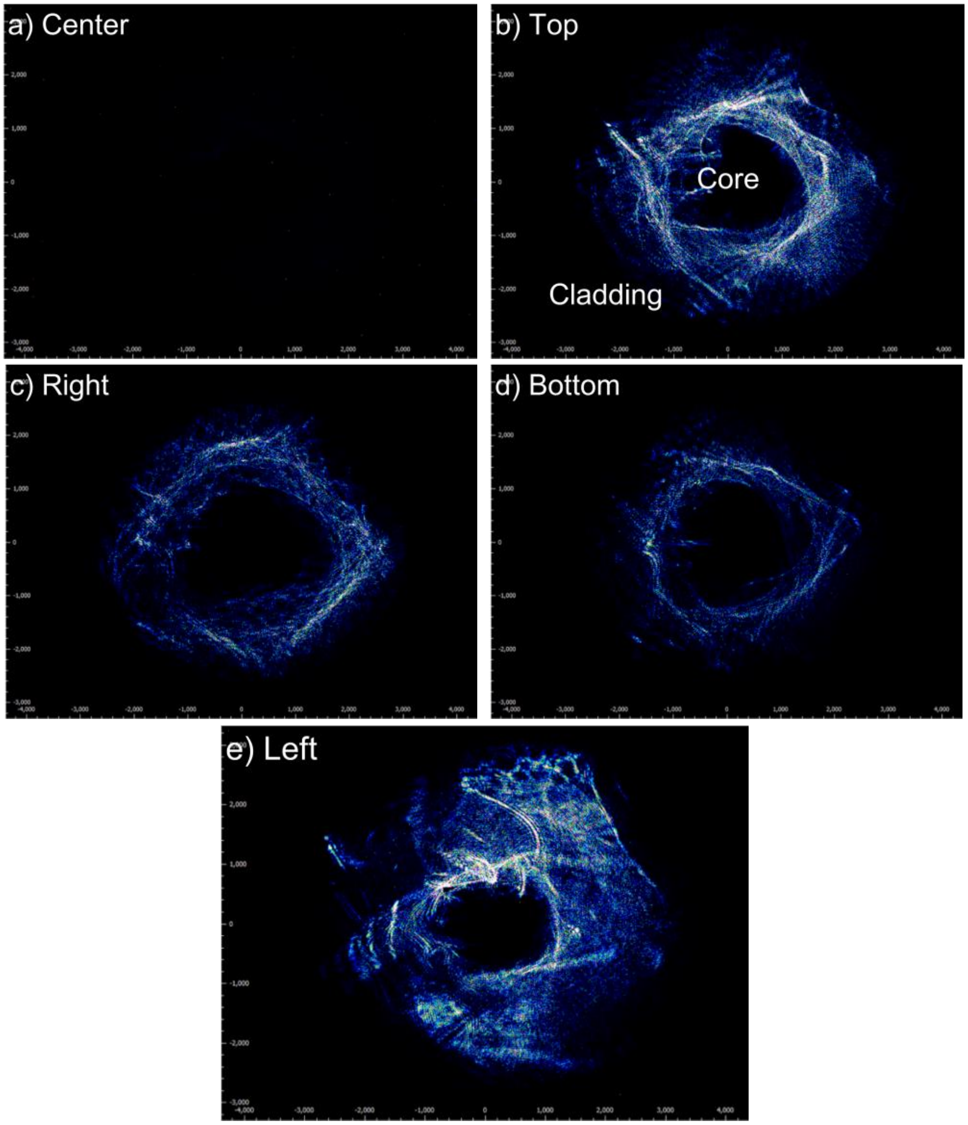

Figure II.4. Light transmission results on fabricated CaO-derived fibers. The images show the output face of each fiber as the input beam is moved. The positioning of the input beam relative to the core is indicated. For Figures a-e, the blue indicates the output light. For simplicity, core/cladding labeled only in "b" but is the same for all figures.

during this deformation, they will be subject to pressures resulting from the viscous flow process. These pressures will tend to elongate the particles until the internal pressure is equal to that of the pressures resulting from the interfacial surface energy. The maximum internal pressure a particle must have for considerable elongation is given as $2\gamma/r_0 \approx 8.6x10^6\ N/m^2$ [5] with γ being the interfacial surface energy (J/m^2) and r_0 being the initial radius of the particle (m).

Using a general value of $\gamma = 5x10^{-3}$ J/m^2 for a phase separated soda lime silicate glass [36], the minimum particle size that can be deformed by viscous flow is 1.16 nm (in a soda-lime silicate glass). Microphases larger than this minimum diameter have been experimentally shown to elongate [4-6]. As indicated previously, the microphases observed in the present system are 3 orders of magnitude larger and therefore may be able to be elongated *if the phase separated cane sample is redrawn at a temperature near the softening point*.

II. D. 1. Two-tier molten core method

In an attempt to mechanically elongate the microphases, a modified two-tier molten core method was devised. The preform used is a conventional 3x30 mm silica capillary preform, although slightly adapted for this technique. The length of the capillary in this case is 15 cm, as compared to the standard 5 cm. The precursor powder is loaded into the preform, and the preform inserted into the optical fiber draw tower. In general, the preform is drawn to a 10 mm diameter sample at some initial draw temperature (~2000°C). As is characteristic with the molten core method, the core becomes diluted by some of the surrounding silica during the draw, thereby shifting the final composition to high silica concentrations. The large diameter sample is drawn first to fabricate the initial phase-separated core. The large diameter (phase separated) sample is reloaded into the furnace and redrawn to ~1 mm diameter cane at a lower temperature (~1700-1800°C). For the large diameter sample to be redrawn, a meter-long sample is needed which is not tenable with a shorter capillary in preforms used in the preceding experiments. The purpose of redrawing at a lower temperature is the intent that the glass will be near the softening point upon drawing, thereby elongating the microphases, and the disordered cane will exhibit signs of longitudinal invariance.

In order to test this hypothesis, the CaO-derived system was utilized. The modified telecommunications-grade, silica preform was loaded with CaO powder (Puratronic® 99.998% purity, provided by Alfa Aesar) and drawn to the large diameter fiber at 2000°C. The cladding and core dimensions were 10 mm and 1 mm respectively. The core was inspected under SEM to verify phase separation. The resulting sample was reloaded in the furnace and redrawn at 1800°C to a 1 mm diameter sample. Again, phase separation was verified using SEM.

Segments of the redrawn canes were cleaved and polished to inspect the cross-section, and additional samples were suspended in resin and polished longitudinally to validate any elongation using the SEM. As shown in Figure II.5, the cane samples remained phase separated, but there were no signs of microphase elongation. This is likely due to the viscosity of the core being significantly lower than the softening point at the redrawing temperature.

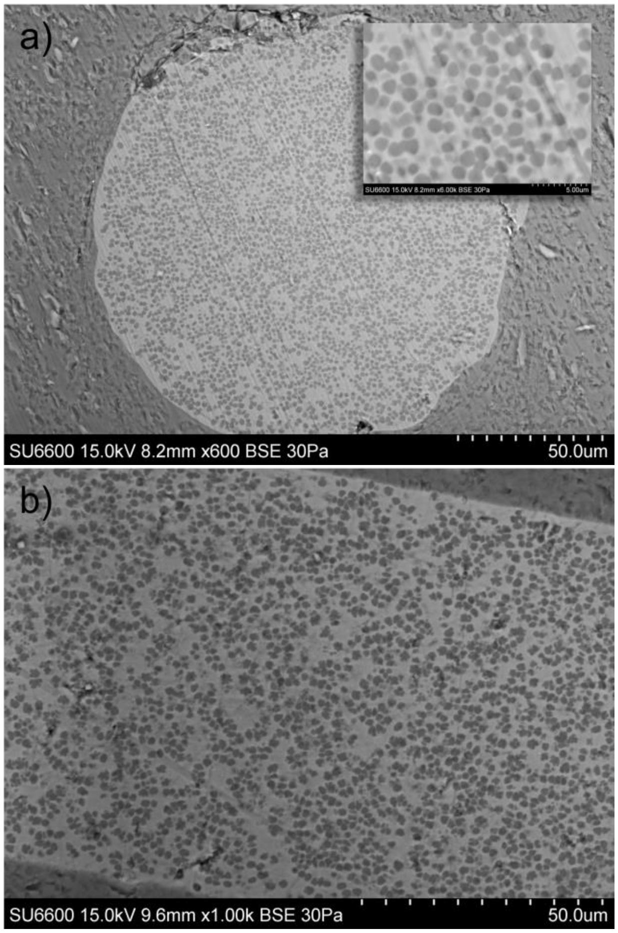

Figure II.5. SEM micrographs of the CaO-derived fiber using the two-tier MC method of fiber fabrication with a) showing the cross section of the fiber after redrawing with a magnified representation of the phase separation, and b) showing the longitudinal section of the fiber.

II. D. 2. Impact of viscosity on microphase elongation

In order to validate this theory, the core viscosity was estimated using the measured compositions. Figure II.6 shows the compositional dependence on viscosity for the CaO-SiO_2 system at 1873K (1600°C) and 2073K (1800°C) [37]. Also indicated are the compositions of the CaO-rich matrix and the SiO_2-rich microphases (determined in II.C.2), their viscosities, and the softening point at $10^{6.6}$ Pa.s. At the redrawing temperature, the viscosity of the microphase is more than 3 orders of magnitude lower than the softening point, and the viscosity of the matrix is 6 orders of magnitude lower. This suggests a much lower drawing temperature is necessary to elongate the microphases, one not tenable with a pure silica cladding.

This can be realized with the relative position within the CaO-SiO_2 phase diagram. The liquidus temperature of the immiscibility dome for this system is 1698°C (Figure II.3). Above this temperature, the system is expected to be fluid ($\eta \approx 10^1$ Pa.s). Since the redrawing temperature is 1800°C, more than 100K higher than the liquidus temperature, the core is effectively molten during redrawing, and the microphases experience negligible viscous pressure. Since the matrix and the microphases possessed viscosities of ~10^1 Pa.s and ~10^4 Pa.s respectively, the microphases were simply transported along the core as the sample was redrawn and were not deformed, similar to glass marbles in a stream of water.

With this in mind, three alternative binary silicate material systems exist with a liquidus in the immiscibility dome higher than the redraw temperature. These are chromium oxide – silica (Cr_2O_3 – SiO_2) [38], zirconia– silica (ZrO_2 – SiO_2) [39], and nickel oxide – silica (NiO-SiO_2) [40]. The liquid-liquid immiscibility temperature for the ZrO_2-SiO_2 system is above 2200°C, well above the highest draw temperature for silica and thereby will not be immediately considered, but the liquid-liquid immiscibility for the NiO-SiO$_2$ system is 1777°C [40], just above the minimum drawing temperature for silica.

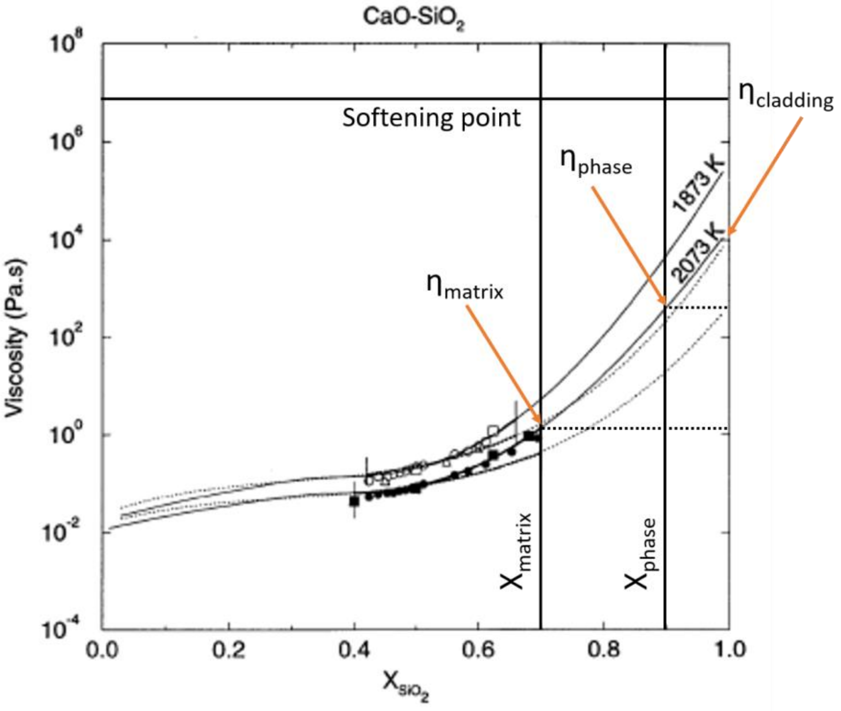

Figure II.6. Compositional dependence of viscosity for the CaO-SiO$_2$ system at 1600°C (1873K) and 1800°C (2073K). Indicated is the softening point for glass ($10^{6.6}$ Pa.s), compositions of the matrix (X_{matrix}) and microphase (X_{phase}) , and corresponding viscosities (η). Adapted from [37].

II. D. 3. Nickel oxide-derived system

In a further attempt to elongate the formed microphases, the NiO-SiO$_2$ system was investigated. Historically, small amounts of NiO are used as a colorant in glasses and ceramics to produce various hues of greens and produces spotted or streaking effects desired by artists [41]. As with many colorants in glass, minute dopant concentrations (< 2 mol%) are necessary to preserve optical transparency. The liquidus in the immiscibility dome of the NiO-SiO_2 system spans from 3 mol% NiO to beyond 50 mol% NiO [40]. Such high dopant concentrations will diminish the optical clarity of the glass. This said, the material system is not ideal for waveguiding but may provide a better insight into and understanding of the microstructure formed in glass fibers as a result of phase separation, and the effects of post-processing on the formed microstructure.

NiO powder (99.995% purity provided by Alfa Aesar) was loaded into the modified, telecommunications-grade silica capillary preform. The preform was drawn to a 10 mm OD sample at 2000°C to induce phase separation, verified by SEM. The sample was reinserted into the draw tower and redrawn to cane with a diameter of 1 mm with a core diameter of ~100 μm at 1770°C, just below the liquid-liquid immiscibility temperature of NiO-SiO_2. Sections of the cane were investigated (transversely and longitudinally) for phase separation and microphase elongation. As shown in Figure II.7.a, the redrawn cane remained phase separated, displaying various phase architectures. Dispersed throughout the core were micron-sized silica-rich phases surrounded by smaller phase separation on the order of hundreds of nanometers (10^{-7} m) (Figure II.7.b). Within the smaller-scale phase separation, the phases showed what appeared to be signs of elongation (Figure II.7.c), and in many cases, the phases were both reoriented and aligned along the draw axis (Figure II.7.d).

In order to better understand some of the phase architecture and provide insight into the microphase elongation, core composition was investigated to determine phases

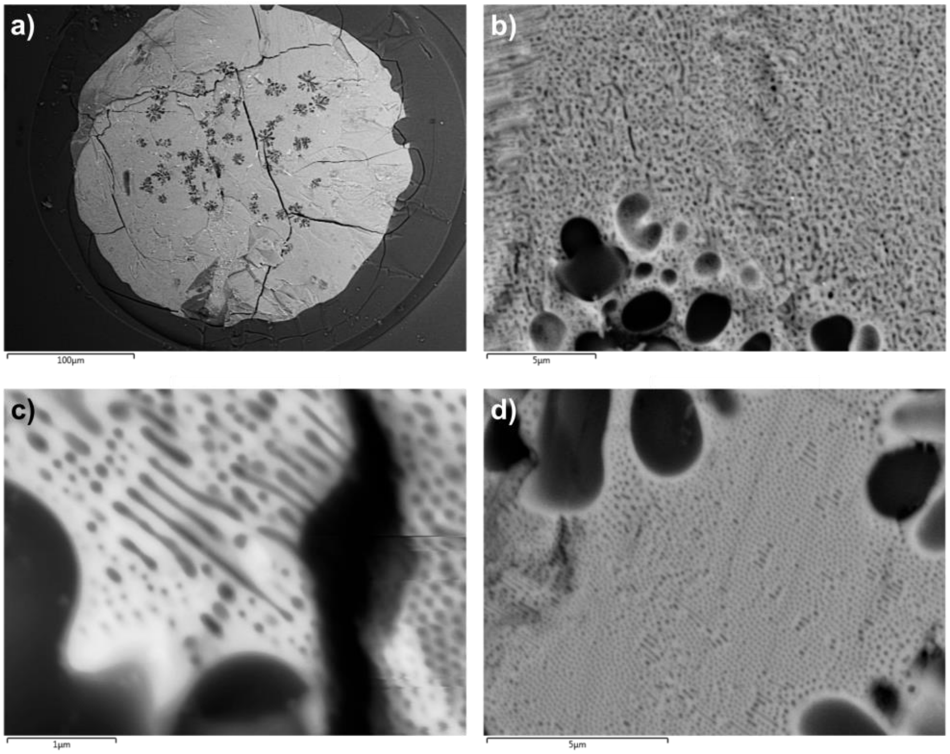

Figure II.7. Micrographs of a) the cross-section of the NiO-derived, redrawn core, b) smaller phase separation surrounding larger phases, c) signs of phase elongation and d) evidence of phases aligning and reorienting along the draw axis. Scales provided below each figure.

present. A section of the core was lifted out using the FIB and subsequently polished to ~100 nm. SEM imaging and EDX provided evidence that the matrix containing the submicron size microphases may contain crystalline nickel orthosilicate (Ni_2SiO_4). To determine the crystallinity, parts of the fiber were pulverized to power for X-ray Diffraction (XRD). Powder XRD was conducted using a Scintag PAD-V X-ray Diffractometer to identify crystalline phases (or lack thereof). The canes were ground to powder using a silica mortar and pestle. It is therefore expected the powder will contain both core and cladding material. The diffractometer utilized Cu K_α radiation (λ = 1.5406 Å) for X-ray generation. The scan range was set to between 5° and 80° two-theta (2θ) with a scan rate of 1°/min. Figure II.8a shows the diffraction pattern obtained from the fiber with the characteristic broad peak for amorphous silica at 23° (2θ), along with distinct Ni_2SiO_4 peaks at 25°, 33°, 35°, 36°, and 37° (2θ).

Further investigations of the microstructure using electron microscopy yielded more indications of crystallinity, including grains and various crystal orientations. Figures II.8 b-e show more of the aforementioned "microphase elongation," except the elongation goes against the draw axis (z-axis). A contradicting NiO-SiO_2 phase diagram possesses a liquidus line for the immiscibility dome is closer to 1700°C [42], similar to that of the CaO-SiO_2 system. This combined with crystalline structures presented in Figure II.7 suggests the observed microphase elongation may have been a result of crystal growth and not necessarily from viscous elongation. However, further studies are necessary regarding the impact of crystal growth on the microphase deformation are necessary to validate this hypothesis.

Interestingly, crystalline Ni_2SiO_4 is known to have magnetic properties [43]. A section of the fiber was placed approximately 5 mm away from a high strength magnet and was attracted to the magnet. The magnetization of three short samples was measured using a PMC MicroMag 2900 Series AGM magnetometer (Princeton Measurements Inc.). Two locations along each sample were tested and the results were averaged over 5 runs. The magnetic moments were determined over a range of -40,000 A/m to

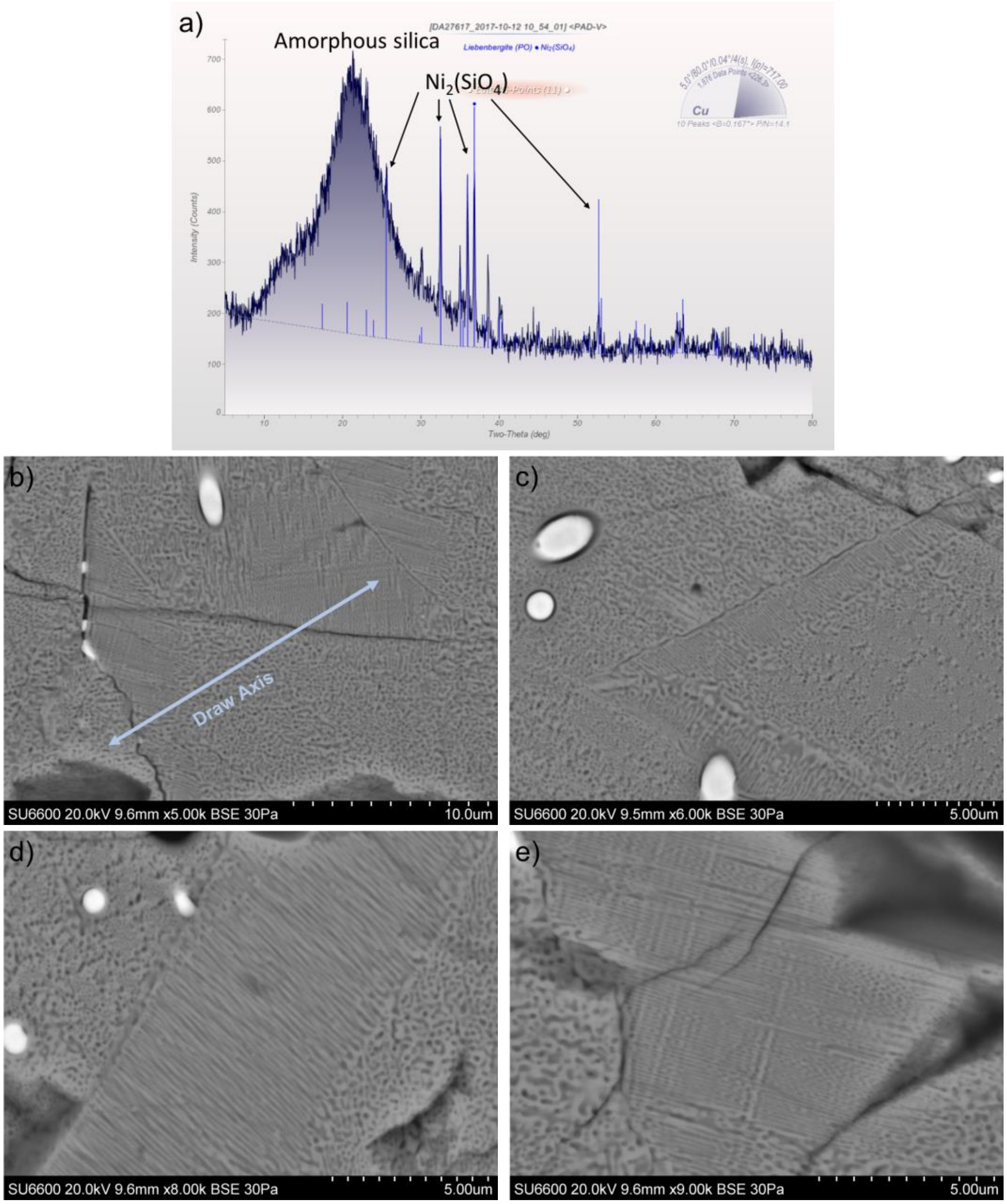

Figure II.8. XRD peak pattern for a) the NiO-derived optical fiber and micrographs of various locations along the longitudinal axis of the fiber showing different crystallographic structures taken at b) 5000x, c) 6000x, d) 8000x, and e) 9000x. For simplicity, the draw axis is provided on the first micrograph, but remains the same for subsequent figures.

40,000 A/m at 342K. Figure II. 9 provides a plot of the resulting magnetic moment as a function of the applied magnetic field. Inset is a magnification of the central region to emphasize a hysteresis. The narrow hysteresis suggests the fibers comprise a soft ferromagnetic material in the core. Additionally, the magnetic moment varies along the length of the fiber, suggesting heterogeneous domains, which is likely considering the microstructure in this present fiber (Figure II.8). While this fiber did not show Anderson localization, if the draw conditions for this material system were optimized and a transversely disordered, longitudinally invariant core produced, rather interesting

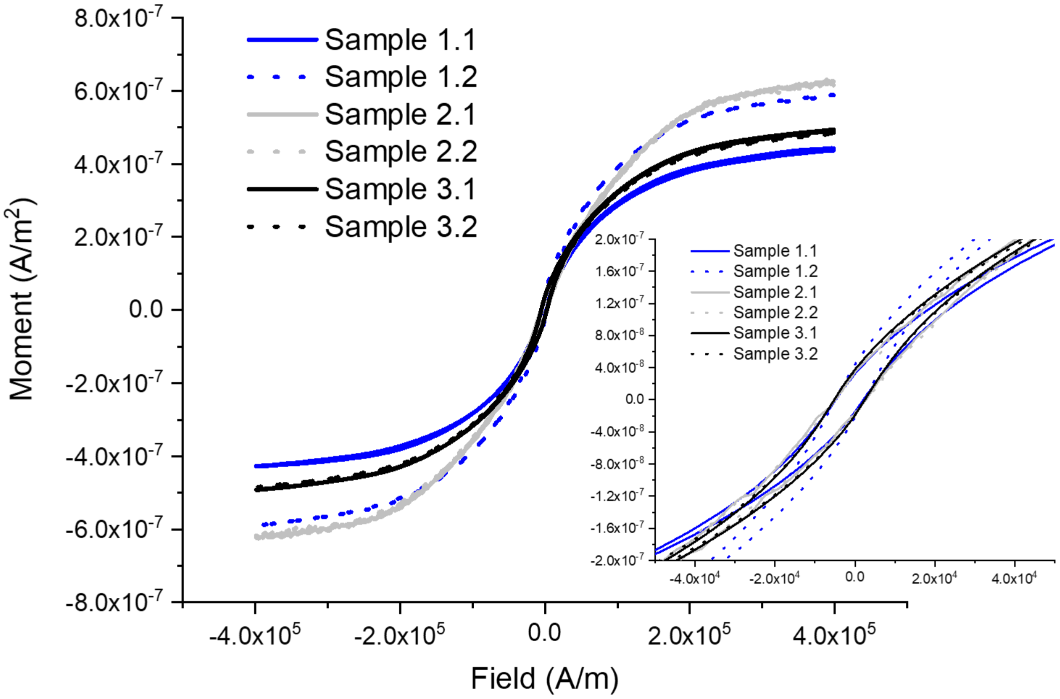

Figure II. 9. Magnetization hysteresis curves for the NiO-derived optical fiber with a magnified plot inset to better represent the hysteresis.

magnetic effects on Anderson localization of light could potentially be investigated [44] using such a fiber.

II. E. Conclusions

Optical fibers exhibiting phase separation during the draw process are profoundly disordered; albeit disordered in both the transverse (desired) and longitudinal directions (undesired). Microspheres formed along the longitudinal axis of the fiber effectively scatter all incident light. For waveguides to guide via Anderson localization, a fiber can be disordered along the cross-section (x- and y-direction) but needs to remain longitudinally invariant (z-direction). In an attempt to satisfy the longitudinal invariance, the two-tier MCM was devised and further investigated. In this process, an initial large diameter (10 mm) cane is drawn to induce phase separation. The phase separated cane is redrawn at a lower temperature so the formed microphases are elongated by viscous flow resulting from a viscosity mismatch between the matrix and the microphase.

The CaO-derived fiber system was investigated as it is known to phase separate using the MCM. A large diameter (10 mm) cane sample was initially drawn (at 2000°C) to induce phase separation in the core, and subsequently redrawn (1 mm) at a lower temperature (1800°C) to elongate the formed microphases. Even at the lowest draw temperature for the silica cladding, the core material exhibited a viscosity more than three orders of magnitude below the softening point. The low viscosity effectively reduces the transfer of force (tension) from the fiber draw process necessary to elongate the microphases, and the phases remained spherical in the final redrawn cane. If the redraw temperature is above the liquid-liquid immiscibility temperature of the core constituents, the core viscosity will be too low to elongate the formed microphases.

The viscosity may be close enough to the softening point if the redraw temperature is below the liquidus of the immiscibility dome of the core constituents. This hypothesis was tested with the NiO-SiO_2 fiber system, since the liquid-liquid melting temperature was initially believed to be 1780°C. The large diameter cane sample was fabricated to induce phase separation, and subsequently redrawn at 1770°C. The core exhibited multiple phase structures and showed signs of phase elongation. This said, the high nickel ion concentration yielded a green translucent core and the multitude of phase structures caused more scattering than light localization and guiding. Also, further investigations revealed the core was semi-crystalline and formed Ni_2SiO_4 phases that, upon crystal growth, may have elongated some of the phases. This is indicated by the elongated phases beginning along the grain boundaries. The small fraction of these phases within the overall fiber structure was sufficient to demonstrate ferromagnetism. Finally, contradicting phase diagrams of the NiO-SiO_2 system portray the liquidus line lower than ~1780°C, suggesting that the core material melted upon redrawing and possessed a viscosity too low to elongate the microphases.

The liquidus temperature is the temperature when the entire system becomes liquid. Below the liquidus, a liquid phase is still present coexisting with a solid phase. Even if a material system is designed to possess a liquidus temperature (of the immiscibility dome) above the redrawing temperature, the consequential liquid phase may still mitigate drawing stresses that would otherwise result in phase elongation. It may be necessary to redraw the formed fiber below the solidus, which is not tenable with a pure silica cladding. As such, exploiting phase separation in glass optical fibers fabricated using the MCM likely is not the optimal fabrication technique for developing TALOFs.

II. F. Appendices

II. F. 1. Lift-out process using the Focused Ion Beam (FIB)

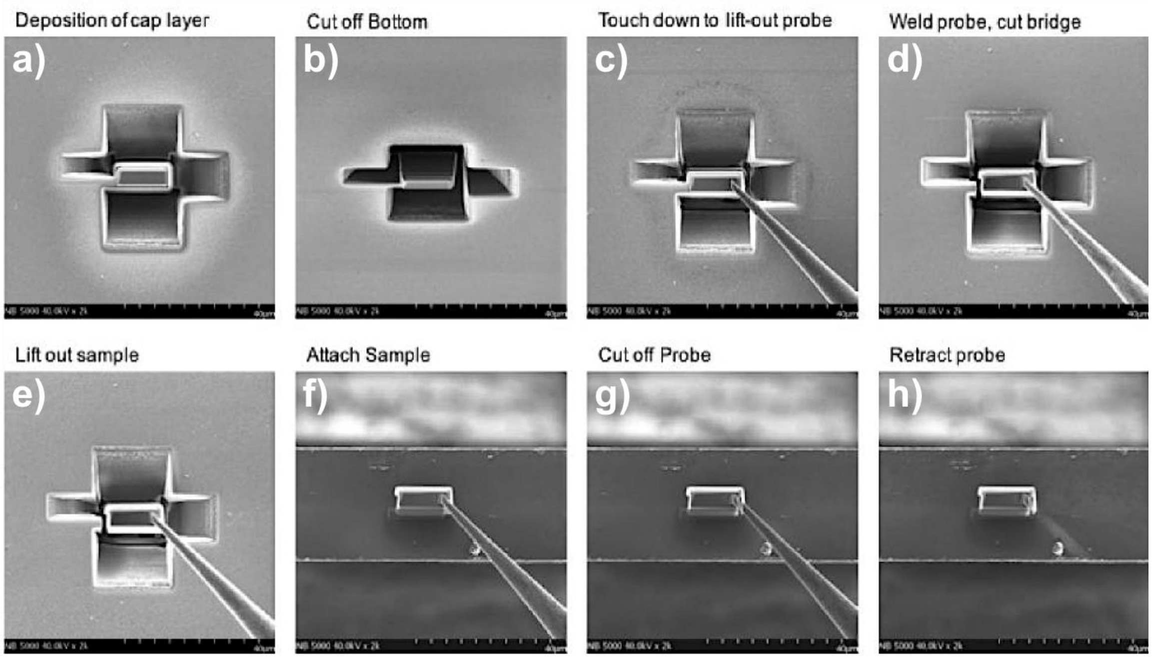

Micrograph representation of lift-out process using the FIB. Figure a) shows material etched away using a gallium ion beam around the rectangular sample, and tungsten layers deposited on top for welding at a later step. The stage is then angled, and the bottom of the sample etched away. At this point in b) the sample itself is attached to the bulk material by a small “bridge.” A small probe is c) positioned several nanometers away from the sample and d) welded to the tungsten layers on the surface. The bridge is etched away and e) the sample is removed from the bulk material. The probe with attached sample is moved and f) attached to a copper TEM grid. The probe is g) etched to detach from the sample and h) retracted for sample analysis. Further ion etching may be conducted to thin and polish the sample to a desired thickness after this point. Figures courtesy of Hitachi.

II. F. 2. Elongation using laser tapering

CaO-derived fibers were sent to AFL Telecommunications in Duncan, SC to be tapered using the LZM-100 LAZERMaster Laser Splicing System. This system uses a CO_2 laser for the heating source, as SiO_2 is known to absorb radiation at the wavelength that CO_2 lasers operate. CO_2 lasers are more precise and tailorable than conventional oxygen/hydrogen flames when acting as heat sources. This system is limited to a 2.3 mm field of view (FOV), therefore the CaO-derived fibers were drawn using the standard MC method to a diameter of 2 mm. Aforementioned fibers were tapered to a diameter of 1 mm and returned to Clemson University for longitudinal characterization. These experiments showed similar results as the two-tier MC method in that the formed microphases were not elongated (Figure II.6). It was later determined that during laser tapering, the glass fiber experiences temperatures higher than 1700°C. At these elevated temperatures, the core material (for the present system) became molten, and the microphases flowed along the fiber as it was tapered.

II. F. 3. Phase separated “cloves”

While exploring phase separating tendencies of other compositions, it was found that not all the formed microphases would be spherical. In two instances, the microphases formed in clusters that had an unusual clove appearance. The first observation of this was in a Y_2O_3 – SiO_2 system (Figure II.10.a), and the other was in a CaO – P_2O_5 – SiO_2 system (Figure II.10.b). It is presently unclear why these “cloves” are forming, and very little is found in the literature regarding their formation / origin.

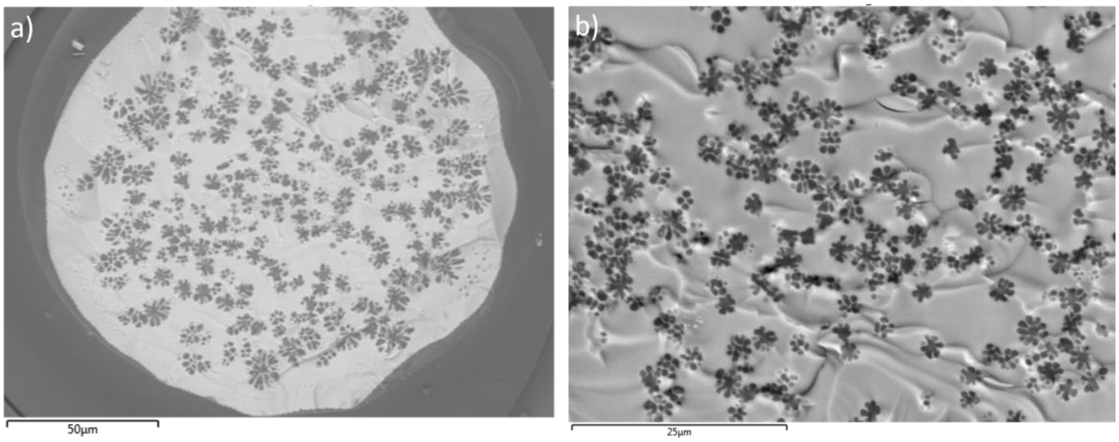

Figure II.10. Electron micrographs depicting unusual phase separation in the a) Y_2O_3 – SiO_2 material system and b) the CaO – P_2O_5 – SiO_2 system.

II. G. References

[1] S. John, “Electromagnetic absorption in a disordered medium near a photon mobility edge,” *Physics Review Letters* **53**, 2169-2172 (1984).

[2] J. Ballato and A. C. Peacock, “Perspective: Molten Core Optical Fiber Fabrication – A Route to New Materials and Applications,” *APL Photonics* **3**, 120903 (2018).

[3] L. Rongved, C. Kurjian, and F. Geyling, “Mechanical Tempering of Optical Fibers,” *Journal of Non-Crystalline Solids* **42**, 579-584 (1980).

[4] L. Randall, and T. Seward, Pseudo-Fiber Optic Devices, US Patent 3,870,399 (1975).

[5] T. Seward, “Elongation and Spheroidization of Phase-Separated Particles in Glass,” *Journal of Non-Crystalline Solids* **15**, 487-504 (1974).

[6] T. Seward, “Some Unusual Optical Properties of elongated phases in Glass,” *Physics of Non-Crystalline Solids*, 342-347 (1977).

[7] J. Ballato, and P. Dragic, “Rethinking Optical Fiber: New Demands, Old Glass,” *Journal of the American Ceramic Society* **96**, 2675-2692 (2013).

[8] M. Cavillon, J. Furtick, C. Kucera, C. Ryan, M. Tuggle, M. Jones, T. Hawkins, P. Dragic, and J. Ballato, “Brillouin Properties of a Novel Strontium Aluminosilicate Glass Optical Fiber,” *Journal of Lightwave Technology* **34**, 1435-1441 (2016).

[9] P. Dragic, C. Ryan, C. Kucera, M. Cavillon, M. Tuggle, M. Jones, T. Hawkins, A. Yablon, R. Stolen, and J. Ballato, “Single- and few-moded lithium aluminosilicate optical fiber for athermal Brillouin strain sensing,” *Optics Letters* **40**, 5030-5033 (2015).

[10] P. Dragic, T. Hawkins, P. Foy, S. Morris, and J. Ballato, “Sapphire-derived all-glass optical fibres,” *Nature Photonics* **6**, 627-633 (2012).

[11] J. Hammel, J. Mackenzie, Method of Forming Microporous Glass Fibers, US Patent 3,650,721 (1972).

[12] J. Kerwawycz, and M. Tomozawa, “Light Scattering from Phase-Separated Glass,” *Journal of the American Ceramic Society* **57**, 467-470 (1974).

[13] T. Takamori, and M. Tomozawa, “Viscosity and microstructure of phase-separate borosilicate glasses,” *Journal of the American Ceramic Society* **62**, 373-377 (1979).

[14] J. Simmons, S. Mills, and A. Napolitano, “Viscous flow in glass during phase separation,” *Journal of the American Ceramic Society* **57**, 109-117 (1974).

[15] M. Tomozawa, and T. Takamori, “Effect of Phase Separation on HF etch rate of borosilicate glasses,” *Journal of the American Ceramic Society* **60**, 301-304 (1977).

[16] D. Gaskell, *Introduction to the Thermodynamics of Materials 5th ed.*, (New York, NY: Taylor & Francis Group, LLC. 2008.) Ch. 10, pp. 263-303.

[17] M. Tomozawa, Advances in Nucleation and Crystallization in Glasses, *Symposium of the Glass division of the American Ceramic Society*, April 26-28, 1971.

[18] M. Tomozawa, and R. Obara, “Effect of minor third components on metastable immiscibility boundaries of binary glasses,” *Journal of the American Ceramic Society* **56**, 378-381 (1973).

[19] R. Doremus, “Viscosity of silica,” *Journal of Applied Physics* **92**, 7619-7629 (2002).

[20] A. Varshneya, and K. Hosmer, “Anomalous Birefringence in Discretely Phase-Separated Glasses,” *Journal of the American Ceramic Society* **72**, 2078-2083 (1989).

[21] M. Tomozawa, *Treatise on Material Science and Techhnology*, Vol 17, Glass II, eds. M. Tomozawa, and R. H. Doremus (New York, NY: Academic Press, 1979).

[22] M. Tomozawa, S. Sridharan, and T. Takamori, “Origin of viscosity increase of phase-separated borosilicate glasses*,” Journal of the American Ceramic Society* **75**, 3103-3110 (1992).

[23] M. Tomozawa, "Liquid phase separation and crystal nucleation in Li_2O-SiO_2 glasses," *Journal of the American Ceramic Society* **13**(6), 161-166 (1972).

[24] G. Neilson, M. Weinberg, and G. Smith, "Effect of OH content on phase separation behavior of soda-silica glasses," *Journal of Non-Crystalline Solids* **82**, 137-142 (1986).

[25] M. Tomozawa, "A source of the immiscibility controversy of borosilicate glass systems," *Journal of the American Ceramic Society* **82**(1), 206-208 (1999).

[26] R. Shaw, and D. Uhlmann, "Subliquidus immiscibility in binary alkali borates," *Journal of the American Ceramic Society* **51**(7), 377-382 (1968).

[27] M. Cavillon, "Molten Core Fabrication of Intrinsically low Nonlinearity Glass Optical Fibers," Ph.D. dissertation, Department of Material Science and Engineering, Clemson University, Clemson, SC, 2018.

[28] I. Veksler, "Liquid immiscibility and its role at the magmatic-hydrothermal transition: a summary of experimental studies," *Chemical Geology* **210**, 7-31 (2004).

[29] J. Wachtman, *Characterization of Materials*, (Stoneham, MA: Reed Publishing Inc, 1993.) Ch. 34, pp. 341-349.

[30] K. D. Vernon-Parry, "Scanning Electron Microscopy: an introduction," *III-V's Review*, **13**(4), 40-44 (2000).

[31] Y. I. Ol'shanskii, *Dokl. Akad. Nauk SSSR* **76,** 93 (1951).

[32] P. Dragic, M. Cavillon, A. Ballato, and J. Ballato, "A Unified materials approach to mitigating optical nonlinearities in optical fiber. II. A. Material additivity models and basic glass properties," *International Journal of Applied Glass Science* **9**(2), 278-287 (2018).

[33] P. Dragic, M. Cavillon, A. Ballato, and J. Ballato, “A unified materials approach to mitigating optical nonlinearities in optical fiber. II. B. The optical fiber, material additivity and the nonlinear coefficients,” *International Journal of Applied Glass Science*, **9**(3), 307-318 (2018).

[34] M. Cavillon, P. Dragic, C. Kucera, T. Hawkins, and J. Ballato, “Calcium silicate and fluorosilicate optical fibers for high energy laser applications,” *Optical Materials Express* **9**(15), 2147-2158 (2019).

[35] S. Karbasi, C. Mirr, R. Frazier, P. Yarandi, K. Koch, and A. Mafi, “Detailed investigation of the impact of the fiber design parameters on the transverse Anderson localization of light in disordered optical fibers,” *Optics Express* **20**(17), 18692-18706 (2012).

[36] J. Hammel, “Direct Measurements of Homogeneous Nucleation Rates in a Glass-Forming System,” *Journal of Chemical Physics* **46**(6), 2234-2244 (1967).

[37] L. Zhang, and S. Jahanshahi, “Review and Modeling of Viscosity of Silicate Melts: Part I. Viscosity of Binary and Ternary Silicates Containing CaO, MgO, and MnO,” *Metallurgical and Material Transactions B* **29** (1), 177-186 (1998).

[38] E. Levin, C. Robbins, and H. McMurdie, National Bureau of Standards, Gaithersburg, Maryland; Private Communication (1964).

[39] A. Kaiser, M. Lober, and R. Teller, “Thermal Stability of Zircon ($ZrSiO_4$),” *Journal of the European Ceramic Society* **28**(11), 2199-2211 (2008).

[40] “NiO – SiO_2” *Data from TDnucl – Thermodata nuclear database:* http://www.crct.polymtl.ca/fact/phase_diagram.php?file=NiO-SiO2.jpg&dir=TDnucl.

[41] C. Harman, and B. King, “Applications of Nickel Compounds in Ceramics,” *Industrial & Engineering Chemistry* **44**(5), 1015-1017 (1952).

[42] T. Besmann, N. Kulkarni, and K. Spear, “Thermochemical and Phase Equilibria Property Prediction for Oxide Glass Systems Based on Modified Associate Species Approach,” pp. 557-566 in *Proceedings of the Electrochemical Society* (Spring 2003).

[43] R. H. Colman, T. Fennell, C. Ritter, G. Lau, R. J. Cava, and A. S. Wills, “Low temperature magnetic structure of the quasi 1-dimensional magnet Ni_2SiO_4,” *Journal of Physics: Conference Series* **145**, 012037 (2009).

[44] L. Schertel, O. Irtenkauf, C. M. Aegerter, Georg Maret, and G. J. Aubry, “Magnetic-field effects on one-dimensional Anderson localization of light,” *Physical Review A* **100**, 043818 (2019).

CHAPTER THREE

FABRICATION OF DISORDERED GLASS OPTICAL FIBERS

PART II – MOLTEN CORE-DERIVED STACK-AND-DRAW

III. A. Introduction

Briefly, as noted in Chapter I and to set the stage for this chapter on fiber fabrication, an early investigation of light transmission in a disordered glass [optical fiber] was made by T. Seward [1,2]. Phase separated glass rods were formed and then elongated at a temperature near the softening point of the glass. The formed microphases were shown to have elongated and unusual light guiding properties were observed in once opaque glasses. Interestingly, these observations were made in the mid- to late-1970s, a few years before TAL was postulated [3,4]. Many years later, Pertsch, *et al.*, [5] investigated light propagation in a 2D array of randomly coupled optical fiber in an attempt to observe TAL in an optical fiber. The fiber developed possessed a structure similar to that proposed by Abdullaev, *et al.* [3] (See Figure I.2.a), however TAL was not observed likely due to the low index difference ($\Delta n \approx 0.00384$). Since then, most of the fibers developed that exhibit TAL have been more closely related to the structures proposed by De Raedt, *et al.* [4]. This includes the first demonstration of TAL in an optical fiber by Karbasi, *et al.* [6], the first observation in a silica-air disordered fiber by Karbasi, *et al.* [7], further studies of TAL in glass-air disordered fibers by Chen and Li [8] and Zhao, *et al.* [9], and the first observation in an all-glass solid tellurite-based fiber by Tuan, et al. [10,11].

While the stack-and-draw method of fiber fabrication is more widely employed for realizing a range of photonic crystal and microstructured optical fibers, including endlessly single-mode optical fibers [12], hollow-core optical fibers [13], fibers for supercontinuum generation [14], and periodic photonic crystal fibers [15,16], many of the *disordered* fibers were developed by some adaptation of this same technique [17]. Each fiber was discussed in Chapter I, however, for completeness, will be briefly described. The polymer disordered fiber [6] was developed by stacking tens of thousands of polymer rods together, fusing the bundle, and drawing to a single disordered fiber. The glass-air disordered fibers of Chen and Li [8] and Zhao, *et al*. [9], were developed by stacking hollow silica tubes of various dimensions together and drawing down to a single fiber. Finally, the tellurite-based fiber [10,11] was developed by stacking tellurite glass rods of different compositions (such that an index difference of 0.1 was achieved) together and drawing to a consolidated rod.

The purpose of this Chapter is to investigate the viability of the stack-and-draw technique utilizing core/clad optical fibers in the stack for fabricating a single disordered optical fiber in the attempt to observe TAL. Firstly, an adapted version stack-and-draw method of fiber fabrication is introduced for stacking prefabricated fibers. Then, the impact of processing the precursor fibers, namely through wet chemical etching and modifying preform dimensions, on the final core architecture is discussed. Additionally, microstructure and material properties of the disordered fiber are investigated, characterized, and the resulting transmission characteristics are discussed. Lastly, initial efforts on semiconductor core TAL fibers are investigated for use as precursor fibers for the stack in an attempt to obtain a large Δn.

III. B. Glass fiber fabrication using the stack-and-draw technique

Precursor optical fibers, i.e., optical fibers later stacked and re-drawn for TAL fiber studies, were initially drawn using the molten core method [18] (MCM, Chapter II.B). A well-studied powder composition (8:5 molar ratio of Al_2O_3 - SrO) was used for the precursor fibers [19]. Unless otherwise specified, all fibers described within this chapter (until the Si-core semiconductor fibers) were derived from this composition. The powder was prepared by weighing and mixing commercial SrO (99.5% purity, Alfa Aesar) and Al_2O_3 (99.995% purity, Alfa Aesar) powders. The powders were ball-milled to ensure homogeneous mixing, and then loaded into a silica tube to construct the preform to be drawn to fiber. This fiber (denoted SrAlSiO) was chosen for the robustness of the bare fiber, which permits post-processing, as well as for possessing intrinsically low nonlinearities, which may ultimately aid in power-scaling of an eventual active device. The capillary silica preform (3 mm inner / 30 mm outer diameter) was drawn to 125 μm outer diameter fiber. Table III.1 provides the initial core composition, draw temperature, final core composition (beginning, end of the fiber) and estimated refractive index of the precursor fibers.

It is necessary that the fibers are bare (no organic material on the surface) when stacked, otherwise the organic material will volatilize during the draw, likely resulting in a rapid, undesirable expansion of softened glass or trapped air bubbles (shown in Section

Table III.1. Composition of the precursor fiber, along with the calculated refractive index (n) and the draw temperature (T_{draw}).

	SiO_2 (mol%)	Al_2O_3 (mol%)	SrO (mol%)	n^*	T_{draw} (°C)
Powder (SrAlSiO)	0	61.5	38.5	---	---
Fiber$^+$	73.1	17.1	9.8	1.52	1925

$^+$ *Obtained from Ref. [19]*

* *Refractive index values used in the calculations were measured at 950 nm, however since the dispersion in the Δn is small over the range of 950 to 1550 nm, the values are assumed to be identical [19]*

III. C. 2). The acrylate coating was removed by soaking the fibers in acetone to swell the coating, then stripped using a razor blade. Any residual coating was removed by setting the fibers in an alumina crucible and placing in a furnace at 600°C for 30 minutes. One end of the bare fibers was dipped in glue to adhere the bundle (Figure III.1.a). If desired, this bundle could then be wet etched in 49% hydrofluoric acid (HF, not pictured). The (etched) fibers were then inserted in a 2.1 mm inner / 2.9 mm outer diameter capillary silica tube to form the bundle (Figure III.1.b). This bundle was inserted in a 3 mm inner / 30 mm outer diameter telecommunications-grade capillary preform (3x30 for short, Figure III.1.c) and subsequently drawn at 2000°C to a 1.5 mm outer diameter (150 μm core diameter) disordered cane.

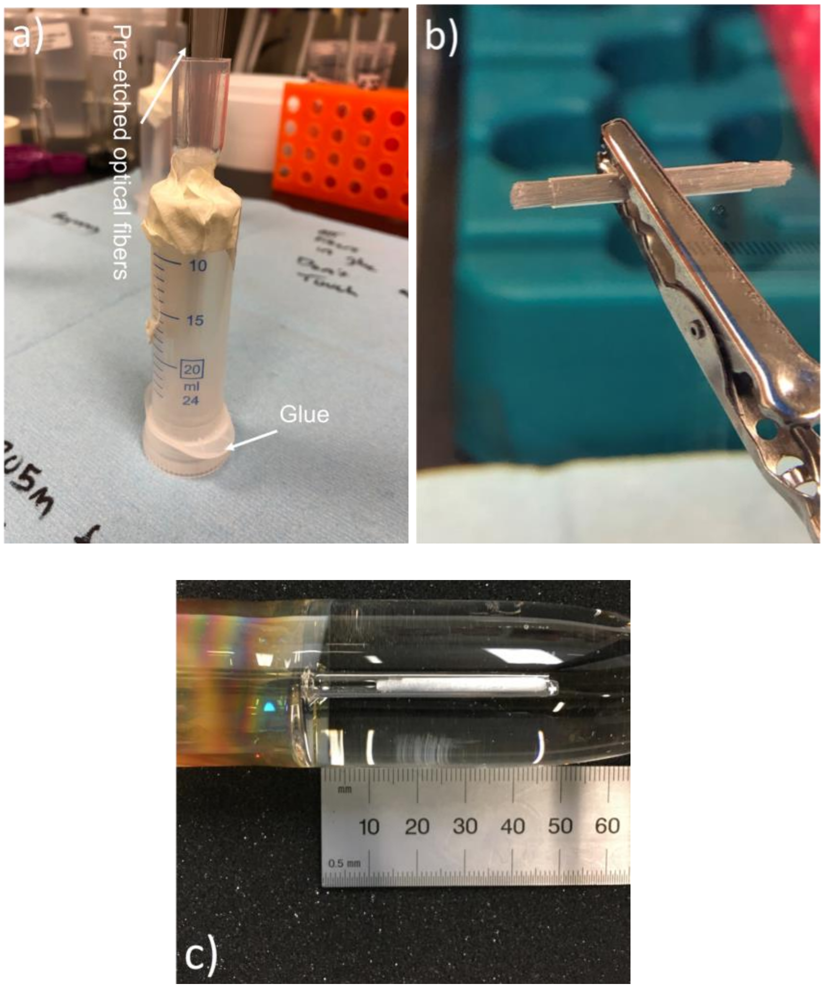

Figure III.1. Sample preparation for the stack-and-draw method, including a) the fiber bundle being adhered using glue to aid in subsequent etching steps, b) the bare fibers in a capillary sleeve and c) the sleeved fibers in a silica capillary preform to be drawn to fiber.

III. C. Fabrication of the disordered cane

Figure III.2.a provides a representative image of the precursor fibers used in the bundle (core diameter was ~15 μm), and Figures III.2.b-d show the resultant disordered cane (DC1) taken at the beginning, middle, and end of the draw, respectively. The gaps present around the overall core indicate that the preform was not entirely consolidated during the draw process. Herein, for consistency, what were the “cores” are considered the high-index phase (doped-silica), and what was the cladding is the low-index phase (undoped-silica). When drawn, the inner diameter of the silica sleeve reduced by a factor of 14 (2.1 mm drawn to 0.15 mm, inner diameter of the sleeve limits the outer diameter of the core). Interestingly, the average site size (Φ) of the high-index phase was 2 μm. If the same diameter reduction were applied (as the preform reduction) to the initial core diameter (15 μm), the expected site size would be 1.1 μm. Additionally, the average pitch (distance between sites, Λ) is 4 μm, and the fill-ratio of the high-index phase was 0.13. The refractive index difference between the high- and low-index phases was assumed to be some value less than what was reported for the precursor fibers, or < 0.07 [19].

The distribution of high index core regions was rather periodic, and the Λ and Φ values deviate from the target. However, these can potentially be remedied by tailoring the precursor material, such as varying the precursor core / clad geometries to lower the average center-to-center spacing between the different phases in the final fiber. Concomitantly, the cane can be further consolidated if a slight vacuum is applied within the preform capillary during the draw in order to remove the gap and yield a fully solid fiber. Since the precursor fibers were all ~125 μm in diameter, the fibers were able to stack in a periodic structure. Acid etching the precursor fibers to different diameters should obviate the periodicity.

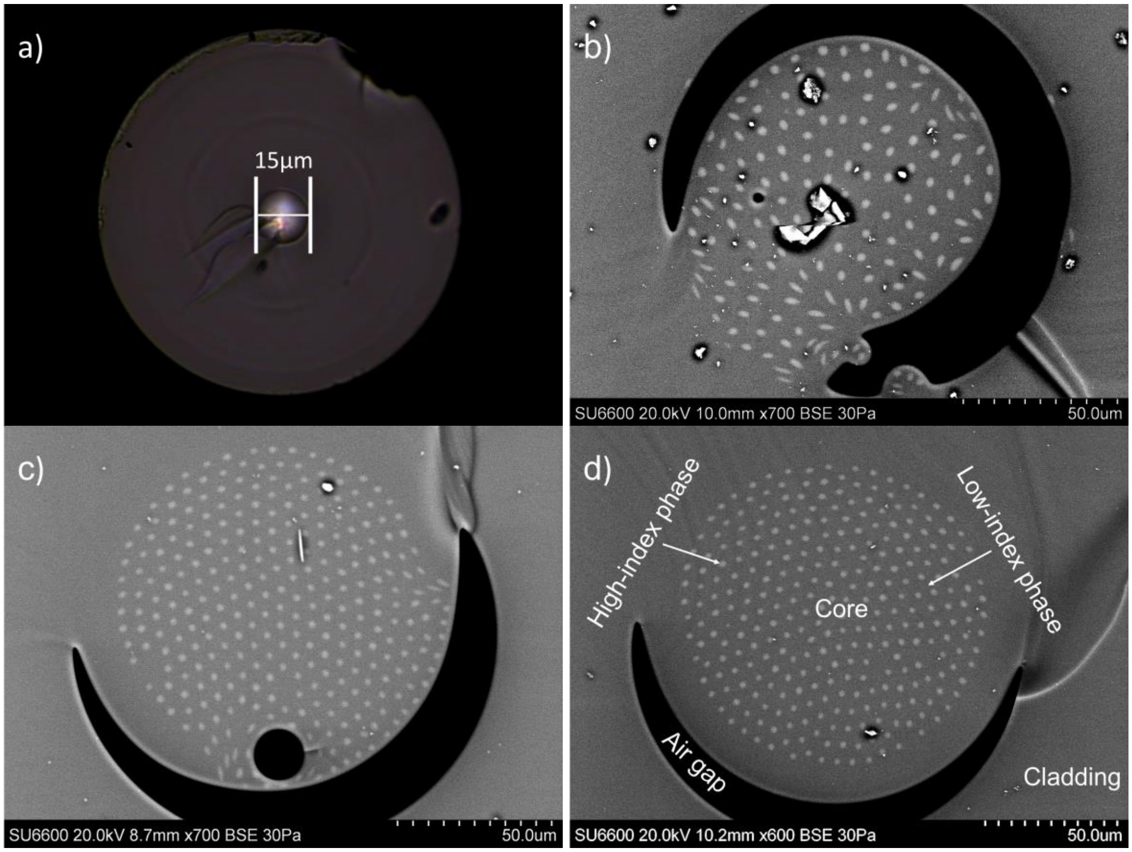

Figure III.2. a) Back-illuminated light microscope image of the precursor fiber used in the stack. Electron micrographs of the disordered core of DC1, taken at b) the beginning of the draw (700x magnification), c) the middle of the draw (700x magnification) and d) the end of the draw (600x magnification).

III. C. 1. Impact of wet etching precursor fibers on final microstructure

Hydrofluoric acid (HF) is commonly used to chemically etch SiO_2 for applications such as precision micromachining of thin films in standard integrated circuits [20] as well as to clean and reduce the dimensions of optical fiber preforms [21]. Due to the extensive technological industries derived from these two applications, HF etching of SiO_2 has been studied for quite some time [22-25]. For pure SiO_2, the general chemical reaction reported by Monk, *et al.*, [24], as:

$$SiO_2(s) + 6HF(l) \xrightarrow{yields} 2H_2O(l) + \; H_2SiF_6(aq)$$

There is some disagreement within the literature regarding the formation of fluorosilicic acid (H_2SiF_6) during the reaction [26] (Verhaverbeke, *et al.*, suggest dissociating H_2SiF_6 to $2H_2O + 2H^+ + SiF^{2-}_6$ as the end-products), however this is not within the scope of this research. In either reaction, a slight concentration gradient may form within the etching solution. Samples will either be suspended in the middle of the solution, or the solution will be agitated during etching to avoid non-uniform etching along the length of the fibers.

It is imperative to know the etching rate of the system, keeping in mind that doped silica tends to etch faster than undoped silica. Literature suggests that the etching rate deviates from a first-order (linear) reaction at high HF concentrations (> 4M or ~8% by weight) [27]. For all etching experiments described herein, the time-scale is generally short and the precision of outer diameter is not imperative, therefore, a linear approximation of the etching rate is deemed sufficient.

Silica-clad, SrAlSiO (SrO-Al_2O_3-SiO_2) core fibers were used to determine the HF etching rates for the 49% HF solution (by weight). A teflon stir-bar was used to ensure a homogeneous solution during etching. Since the outer diameter of the fibers are being measured, the etching rate is considered for fused silica from the cladding. Figure III.3 provides a plot of the optical fiber diameter (measured using an optical microscope, 127 μm at $t = 0$) as a function of time submerged. The slope of the line (possessing a linearity

r^2 value of 0.9977) suggests an average HF etching rate of 3 μm/min of pure silica. Even though the HF etching rate of silica is dependent on composition, stress, and fictive temperature [28], it is assumed the fictive temperature of the fiber cladding is similar between all samples (since draw at approximately the same draw temperature and speed and fiber outer diameter, hence cooling rate) and residual stress in the cladding is negligible that neither will have an appreciable impact on the etching rate.

The bare fibers were etched for 3, 5, 8, and 13 minutes in the HF-solution to yield precursor core fibers of varying outer diameters. The etched fibers were then bundled inside a silica capillary sleeve and inserted into a silica 3 mm x 30 mm (“3x30”) capillary preform. The preform was drawn at a temperature of 2000°C under a vacuum of 50” of

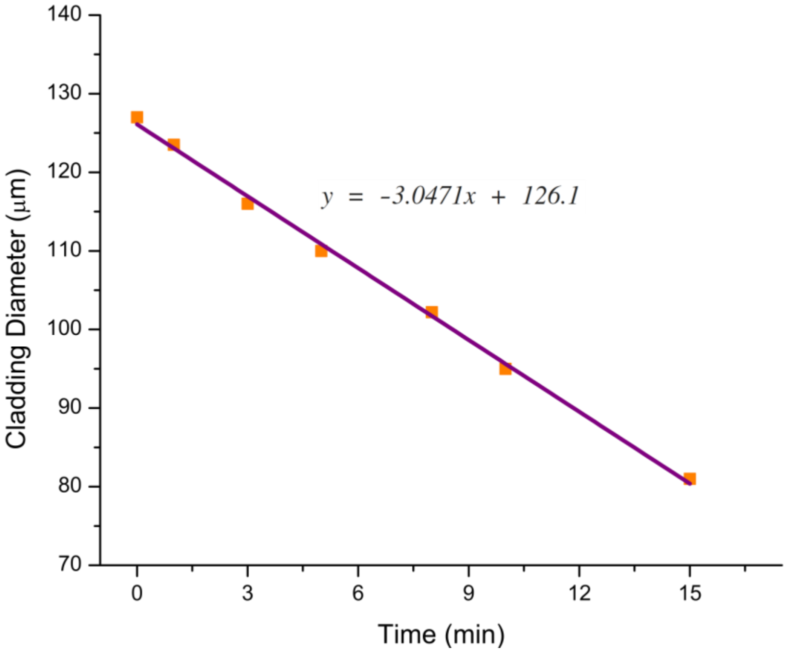

Figure III.3. Plot of the measured (silica) cladding diameter as a function of etching time in 49% HF solution. The slope of the line provides an estimated etching rate in μm/min.

water to a 1.5 mm cane (150 μm core diameter). Figure III.4 is a micrograph of the resulting disordered cane (DC2). There are no visible gaps around the core, suggesting the vacuum applied during the draw effectively consolidated the core, and the microstructure appears to be less periodic. The fill-ratio was slightly higher than DC1 at 0.18, and the average Λ decreased to 2.5 μm. The average Φ remained similar to the previous draw at 2.1 μm, which is to be expected as the reduction in preform diameter remained constant. These, in addition to the microstructure of DC1, are summarized with the target values after this section in Table III. 2 of Section III. D.

DC2 was tested for TAL at the University of New Mexico. For localization testing, cane samples were cleaved to different lengths and the facet hand-polished. The cane was then end-coupled to a SMF-28 optical fiber, which itself was coupled to a He-Ne laser (λ=632.8 nm). The SMF-28 fiber is on a motorized stage that can move in the

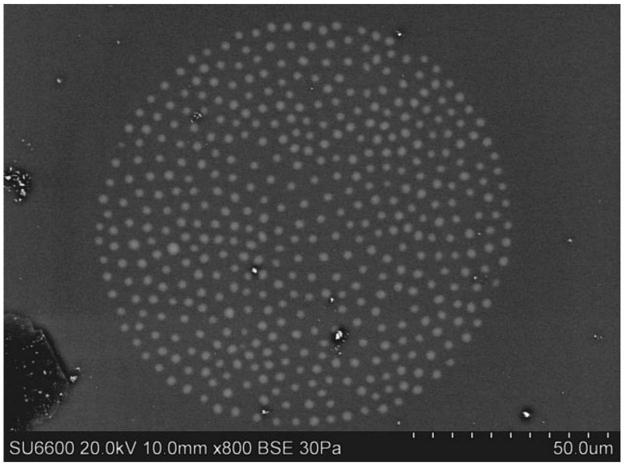

Figure III.4. Electron micrograph of the cross-section of DC2 at 800x magnification. The lighter contrast phases are the high-index phases.

three Cartesian directions. The SMF-28 fiber is then moved to positions relative to the core and the light intensity is recorded from the output facet using a CCD camera beam profiler [29]. Figure III.5.a-c show the output face of the disordered cane (recorded on a CCD) as light is coupled to different regions of the core. Light propagated along the length of the cane, though the nature of the output, in which the light is seen illuminating the high index cores regions, suggests the individual high-index nodes were guiding the light by total internal reflection, and not TAL. Accordingly, many of the microstructural parameters still needed to be optimized, namely the Λ and the Φ, and the index difference quantified.

III. C. 2. Impact of preform dimensions on final microstructure

In order to obtain a (high index core region) site size closer to the target value of 1 μm, either the final cane needs to be drawn to a smaller diameter from the 3x30 preform, or the initial preform dimensions needs to be larger. Since a large-area core is desired, the former option was eliminated, suggesting larger preform dimensions are needed. Therefore, the etched fibers were sleeved in a larger silica capillary tube (5.4 mm inner / 6.8 mm outer diameter) and inserted in a larger inner diameter silica preform (7.8 mm inner / 30 mm outer diameter) as shown in Figure III.6a. The preform was drawn at 2000°C to a 1 mm cane (~175 μm core). Figure III.6b shows an electron micrograph of the cross section of the disordered core (DC3). The voids throughout are likely from organic residue (acrylate coating) on the precursor fibers off-gassing during the draw

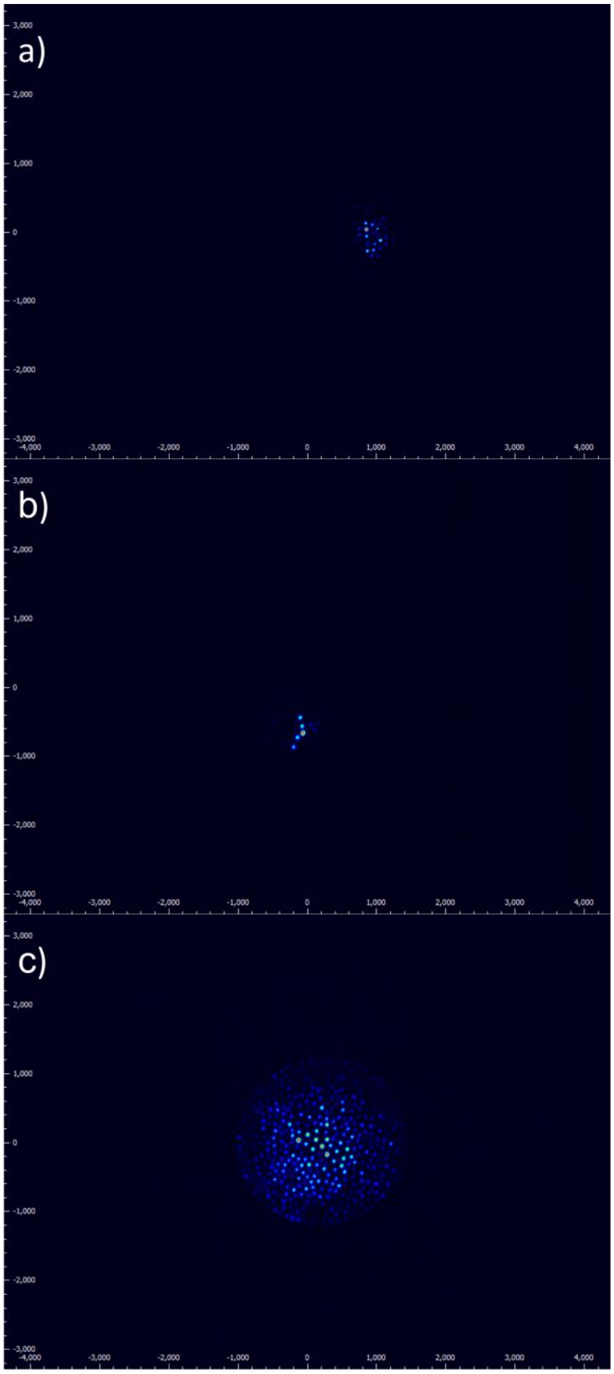

Figure III.5. Output of light recorded on a CCD camera from the disordered core when light is input in the a) right, b) the left, and c) the center of the core. The x- and y- axis represent the relative position (arbitrary units).

process. Since the number of fibers used in the stack nearly quadruples (~400 fibers used for DC1 or DC2, and ~1500 used for DC3), the likelihood of missing some of the acrylate coating on the fibers is higher. The average Φ decreased to 1.4 μm and the Λ was 1.6 μm. It is expected that a decrease in Λ would yield a higher fill ratio, however, due to the voids occupying large areas thereby skewing the image analysis, the average fill ratio was measured to be 0.20 similar to DC2.

The longitudinal invariance of the core microstructure was investigated along a 20 cm length piece of the cane. The cane was cleaved in 5 cm intervals. Figure III.7a-d are electron micrographs taken at the 0, 5, 10, and 20 cm for the respective samples. As shown, air bubbles are present, and an air bubble is occasionally elongated (shown with the orange arrow) though most seem to be randomly distributed throughout the length of

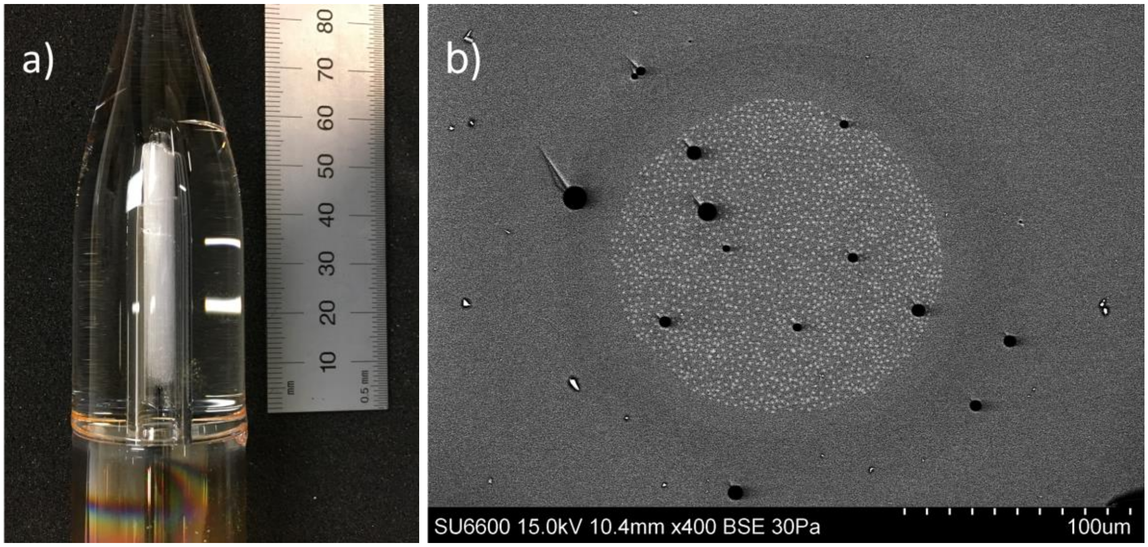

Figure III.6. Example image of a) the fiber bundle inside a 7.8 x 30 mm preform, and b) representative electron micrograph of DC3 taken at 400x magnification.

the cane. Since not all are longitudinally uniform, these bubbles will undoubtedly impact the transmission properties resulting in significant loss. Since transmission loss is not an initial concern, these air bubbles can be neglected for current measurements. Future precursor fibers are thermally treated to eliminate organic residue on the surface of the fibers to minimize the presence of these bubbles in the final core. Contrary to the bubbles, the high-index phases show minimal variations along the tens of centimeters. Three locations are emphasized with an orange circle to visually aid the reader in following the change in architecture throughout the images. Since many of the TAL measurements occur at lengths less than 10 cm, it is assumed the core architecture is essentially uniform over these short lengths.

The actual composition was not measured for DC3 since the high-index phases are small in diameter. As described in Chapter II, standard EDX probes the surrounding silica during measurements thereby providing an inaccurate composition. For more accurate measurements, samples need to be “lifted out” using a focused ion beam and subsequently ion etched to a thickness of ~ 100 nm. At this thickness, the electron beam probes much smaller areas, ensuring the measurement is only of the high index phase. This technique is oftentimes difficult and can be time-consuming (thereby expensive) and was not performed on all fibers. The composition was, however, measured for the cane DC4 later described in Chapter IV. The only difference between compositions and draw parameters was the addition of 5 mol% of Yb_2O_3 for DC4. The measured composition of Yb_2O_3 in DC4 was less than 0.5 mol%. Since the active dopant concentration is so low, it

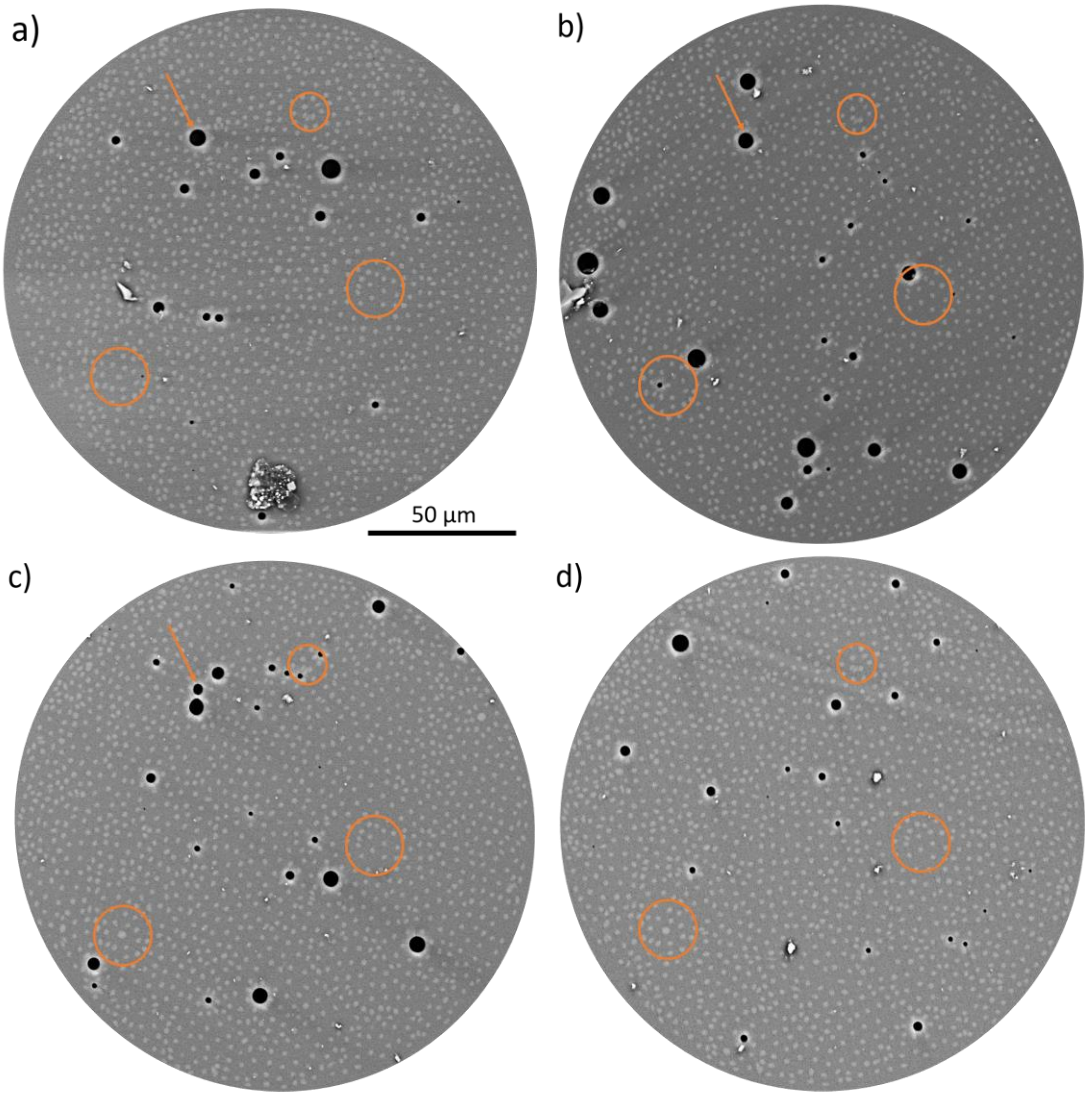

Figure III. 7. Representative electron micrographs (500x magnification) of the core architecture from a) 0 cm, b) 5 cm, c) 10 cm, and d) 20 cm along the length of the cane sample depicting the evolution of the microstructure. The scale bar applies to all figures. The black spots represent the air holes, the high-index cores appear as the brighter dots, and the low-index silica is the darker grey. Circles and arrows added to aid the reader.

is assumed the Δn of DC3 is similar to that of DC4. Therefore, an assumed Δn value of 0.01 (determined in Chapter IV) will be used for subsequent discussions of DC3.

With the microstructure "inching" closer to the target parameters, DC3 was tested for localization. Figure III.8a-c provides the output facet of the disordered core as light from a He-Ne source is coupled to different regions. Although some of the individual high-index nodes guide light, they are randomly coupled with nearby nodes, suggesting evidence of TAL [30]. There was a large amount of transverse scattering observed within the core, effectively limiting the observed TAL to shorter lengths (< 5 cm). Beyond this critical length, the beam either occupies the entirety of the core and appears localized due to the mismatch between the cores and the protective cladding, or the intensity of the beam diminishes due to loss.

It is unclear the exact mechanism of the transverse scattering, though it is believed to be a result of one or a combination of the longitudinal variations in the microstructure, or due to a low refractive index difference between the high and low index phases. This said, many optical measurements (e.g. absorption, emission, lifetime, attenuation, and optical nonlinearities to name a few) can be made using short lengths of the fiber. Thereby, this fabrication technique provides a plausible route to investigating material influences on TALOF, and core structure / waveguide influences on optical properties of the resulting optical fibers.

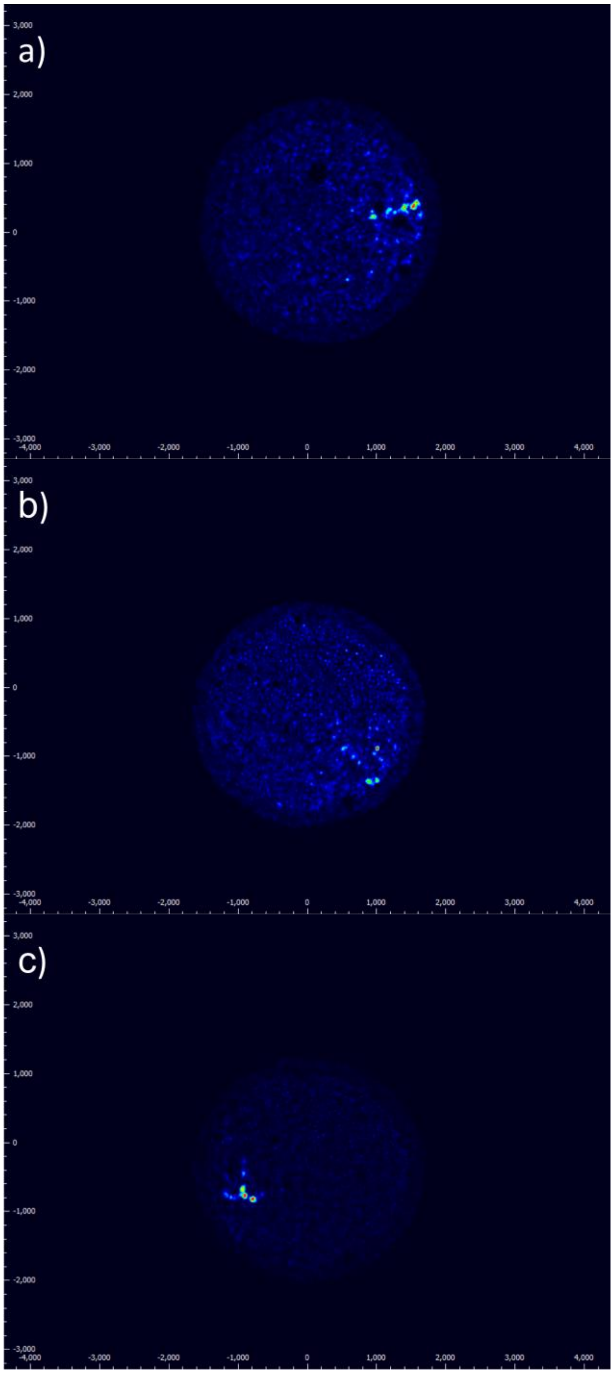

Figure III.8. Output of light recorded on a CCD camera from the disordered core when light is input in the a) upper right, b) the lower right, and c) the left side core. The x- and y- axis represent the relative position.

III. D. Comparison to *in situ* phase separation

A model was established to characterize the disorder within these fibers compared to the CaO-derived phase separated cane of Chapter II using a radial distribution function (RDF) and the statistical variance (σ^2) of the resulting plots. Figure III. 9 provides a plot of the RDF for the cross-section of DC1 (Figure III. 2d), DC3 (Figure III. 6b) the CaO-derived phase separated cane (denoted PS-cane, Figure II. 1a), and a theoretical photonic crystal fiber [31] for comparison. The PCF is included as a reference to the reader to exemplify a perfectly ordered system, as compared to the disordered systems of this dissertation.

The RDF counted all instances of a micro inclusion (high-index phase for DC1 and DC3, or low-index phase for PS-cane and PCF) intersecting one of a series of concentric circles spaced equidistant from the center of the core region. Position 0 represents an arbitrary point in the center of the core. For DC1, the radius of each concentric circle increased by 2.1 μm, 2.5 μm for DC3, 3.4 μm for PS-cane, and 1.1 μm for the PCF. Therefore, to obtain the true distance for each sample, simply multiply the number along the abscissa by the respective interval factor. The number of counts was normalized to the distance of the intervals to account for the increased circumference of each circle.

The variance of each was calculated (neglecting the 0 counts) using the sample sets in excel and are provided in Figure III. 9 next to the respective plots. Inasmuch, the PCF showed perfect order with a variance of 0.0%, with the next lowest being DC1 with a variance of 2.2%, DC3 had a variance of 8.0%, and the PS-cane had the highest of

107.9%. The higher percent variation as a function of radius, the more disorder considered to be within the microstructure. Inasmuch, when comparing DC1 and DC3, etching the precursor fibers and increasing the preform dimensions resulted in a near four-fold increase in variance. This said, both DC1 and DC3 were more than an order of magnitude lower than the PS-cane.

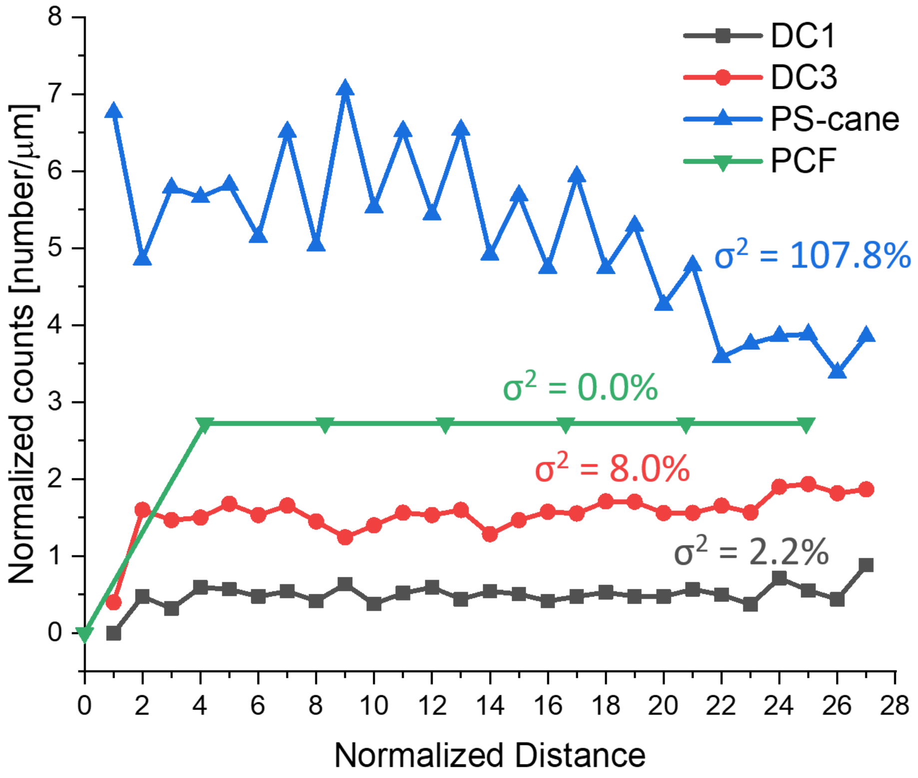

Figure III. 9. RDF plot measuring the number of inclusions as a function of radius for cross-sections of DC1 (black), DC3 (red) the phase separated cane described in Chapter II (blue), and a theoretical PCF (green) proposed in Ref. 31. The 0 position along the abscissa indicates an arbitrary point in the core center.

Table III.2 provides a comparison of the microstructural properties for the CaO-derived phase separated fibers of Chapter II and DC3. Most of the microstructure properties between DC3 and the CaO-derived fibers are similar in magnitude. Due to the random nature of both fibers, the Λ and Φ are reported as average values since they will differ throughout the fibers. The Δn and longitudinal invariance, however, differ greatly. The stack-and-draw technique yielded a cane with large degree of longitudinal uniformity with only minor variations along tens of centimeters, contradictory to the phase separated fibers. Additionally, the refractive index difference between the two glass phases was significantly lower for the stack-and-draw technique compared to the phase separation, however the lower index difference primarily limits the optical path length (length at

Table III.2. Microstructural properties of DC3 compared with the phase separated CaO-derived fiber from Chapter II and the target properties for a TALOF adapted from Ref. 32, including the refractive index difference (Δn), the core diameter (Φ_{core}), the diameter of the microphase ($\Phi_{microphase}$), and the pitch (Λ).

Material Parameter	**Target**	**DC1**	**DC2**	**DC3**	**CaO-derived**
Δn	0.10	< 0.07	< 0.07	0.01^{+}	0.05
Φ_{core}	150 μm	115 μm	150 μm	175 μm	120 μm
Avg. Fill Ratio	0.50	0.13	0.18	0.20	0.32
$\Phi_{microphase}$	1.00 μm	2.00	2.10	1.40 μm	1.10 μm
Λ	1.00 μm	4.00	2.50	1.60 μm	0.66 μm
Longitudinal Invariance	Yes	Yes*	Yes*	Yes	No

$^{+}$*Assumed using measurements taken from DC4 described in Chapter IV*

**Assumed based on the longitudinal invariance study of DC3* which TAL can be observed). While both are imperative to obtaining a TALOF, at least small lengths (5 cm) of longitudinal invariance is necessary for light propagation.

III.E. Semiconductor core optical fiber

In an attempt to develop a TALOF with an exceptionally high Δn, silicon (Si) core semiconductor fibers [33] were investigated for use as precursor fibers further utilizing the stack-and-draw technique as modified and developed in this Dissertation. The estimated Δn for a fiber consisting of a silicon core and a silica cladding is greater than 2 (at $\lambda = 1.30$ μm, $n_{silica} = 1.4469$ [34] and $n_{silicon} = 3.5050$ [35]), an order of magnitude larger than the target value of 0.1. High purity silicon was inserted in a high purity 3 mm inner / 30 mm outer diameter telecommunications grade silica preform and drawn to fiber. Nearly 500 m of fiber was drawn at a temperature of 1950˚C to a total cladding diameter of about 125 μm. A conventional single UV-curable acrylate coating was applied during the draw yielding a fiber diameter of about 250 μm. Herein, this fiber will be considered the “Si-core fiber.” Figure III.10. provides an optical microscope image of the resultant fibers. The strong Fresnel reflection under front illumination in the core suggests the presence of the Si semiconductor phase. Using a combination of ImageJ and measurements from the optical microscope, the core diameter was determined to be ~10 μm.

Due to the high temperatures associated with the draw, the core (high-index phase) is further diluted with the surrounding silica cladding during redrawing of the precursor fibers. Consequently, if enough silica (or oxygen) from the cladding is

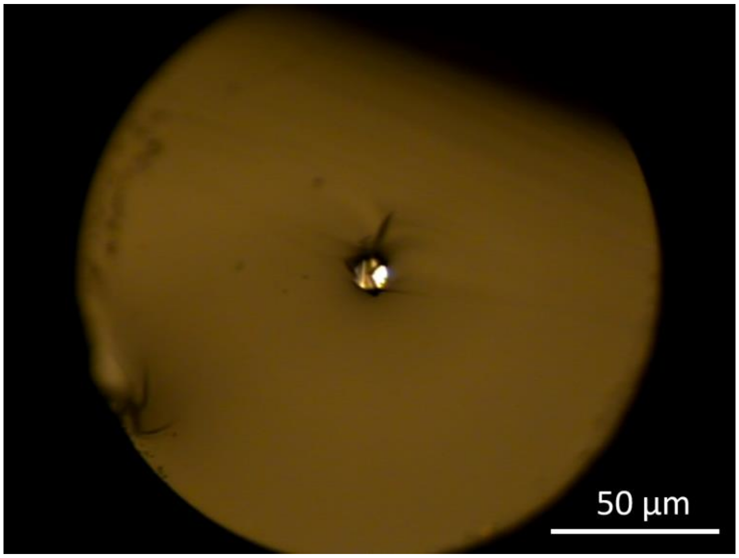

Figure III.10. Optical microscope image of a silicon core fiber clad in silica. The strong Fresnel reflection in the core suggests the presence of the semiconductor phase.

incorporated into the Si-core, the silicon effectively oxidizes, and the semiconductor phase core is lost. To study the impact of redrawing on the final core composition with the semiconductor system, fibers were stacked and redrawn neglecting the acid etching step. Precursor fibers were set in acetone to swell the acrylate coating that was then removed using a razor blade. The bare fibers were placed in a conventional box furnace at 600°C to ensure no residual organic material on the surface. Bare fibers were bundled together in a capillary silica tube (2.1 mm inner / 2.9 mm outer diameter) and subsequently inserted into the silica preform (3 mm inner / 30 mm outer diameter), shown in Figure III.11. The preform was loaded in the draw tower and drawn to a 1.5 mm

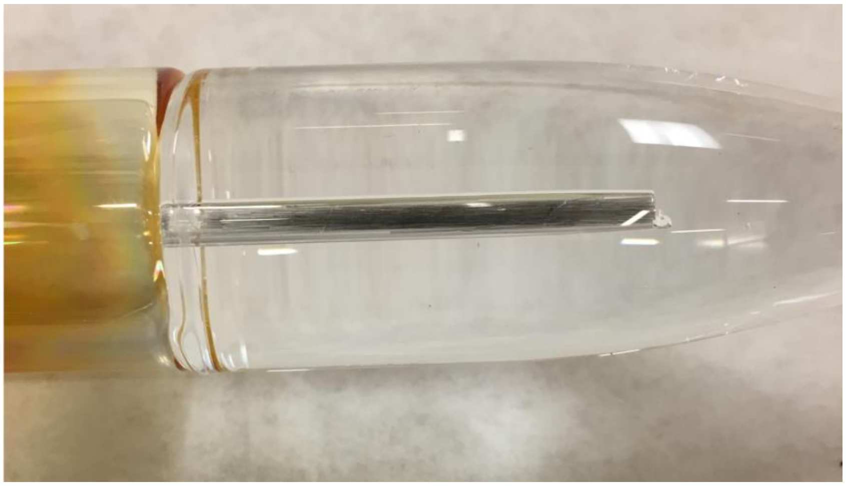

Figure III.11. Optical fiber preform with Si-core precursor fibers stacked in the inner capillary to be drawn to the final disordered cane. The dark color of the fibers suggests the presence of the semiconductor phase.

outer diameter (150 μm core diameter) cane at 1950°C with a vacuum of 50” of water applied to consolidate the cane.

Figure III.12.a-b are optical microscope images of the resultant cane drawn under vacuum. Few high index (Si) sites remain in the core after drawing, either due to the dissolution of the silica cladding and subsequent oxidation of the Si to SiO_2, or the vacuum pulling the molten Si from the stack. Since the draw temperature is nearly 500K higher than the melting temperature of crystalline Si, the viscosity of the melt will be significantly lower than the surrounding silica (viscosity of fused silica at 2000°C is approximately 10^4 Pa.s [36] whereas the viscosity of silicon measured 400K colder is ~10^{-4} Pa.s [37]) and the molten silicon could potentially be pulled out of the core with a sufficient vacuum. Another stack of precursor Si-core fibers was prepared and drawn to a disordered cane with similar draw conditions, except no vacuum was applied. As shown in Figure III.12.c-d, still very few high index sites are present, and the core has noticeable air-gaps, suggesting the applied vacuum is not the issue (similar to the process reported in Ref. [38]).

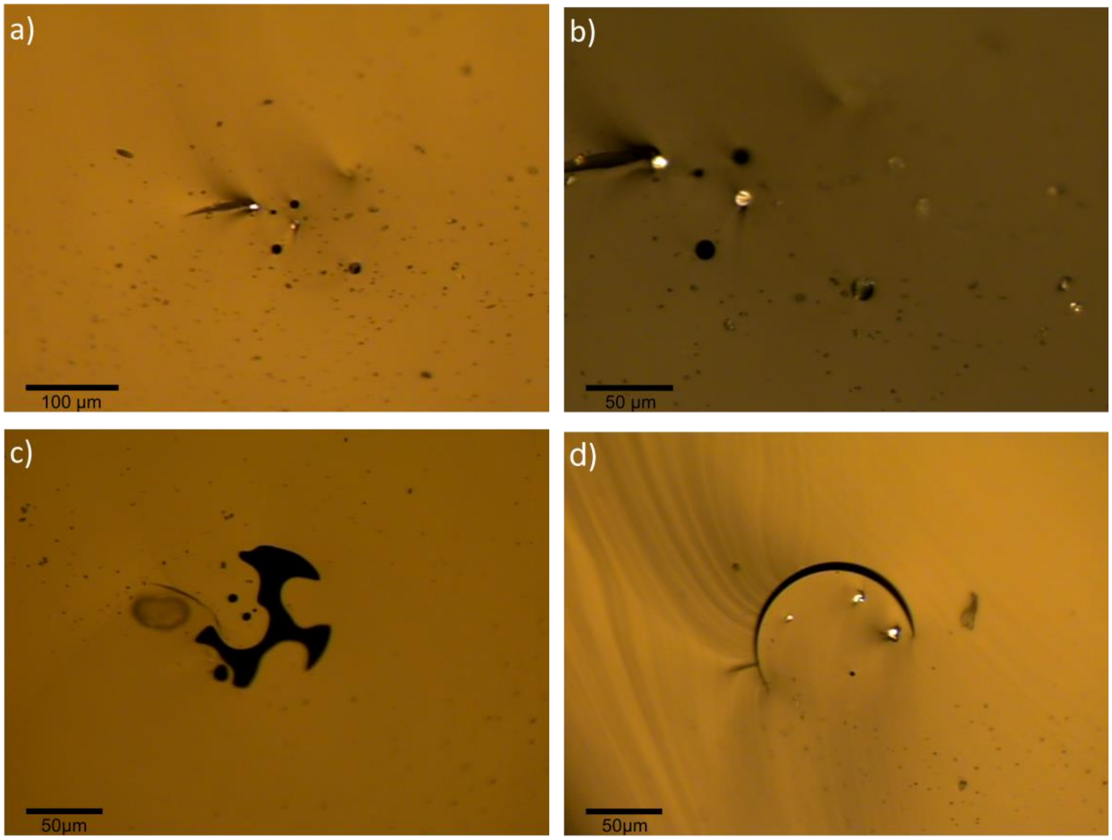

Figure III.12. Front-illuminated light microscope image of the resultant stack-and-draw fibers drawn with vacuum (a and b) and without vacuum (c and d) applied during the draw. The occasional bright spots indicate remaining semiconductor cores, where the dark spots are voids in the glass.

Novel, and rather clever, processing techniques have been investigated to “scavenge” the oxygen migrating into the core. These techniques effectively mitigate the incorporation of oxygen in the silicon-core fibers using either silicon carbide for removing the oxygen [39], or through use of an alkaline earth oxide interface between the Si-core and silica cladding [38]. As argued in Ref. 38, the alkaline earth oxide interface appears to be more effective in scavenging the oxygen, thereby reducing the oxidation of the core. This methodology will be pursued to redraw the Si-core fibers to smaller site sizes (1 μm) using stack-and-draw.

Silica capillary preforms were coated using the process outlined in Ref. 38 and will be briefly described here for completeness. The inner surface of the preform was initially cleaned by filling the cavity with ethanol, drained, and subsequently dried with nitrogen. The coating was prepared by mixing deionized water with CaO powder to form an aqueous calcium hydroxide ($Ca(OH)_2$) paste, and inserted into the preform using glass pipettes. The coating was applied to the walls of the preform using a 2 mm diameter twisted shank tube brush, using surface tension to spread the coating, thus allowing for a uniform layer along the walls of the preform. The preform was dried in an oven at 100°C to remove residual water in the coating. Once dried, a rod of high purity silicon (2.9 mm outer diameter) is inserted in the capillary and the preform loaded in the draw tower. Figure III.13 is an image of the coated preform with the silicon rod inserted.

If the coated preform is exposed to the atmosphere for an extended period of time, the CaO coating can convert to $CaCO_3$ at room temperature. If this is not accounted for, the $CaCO_3$ will decompose during the fiber draw, off-gassing CO_2 into the molten core.

Figure III.13. Optical fiber preform with a calcium oxide coating the inner capillary. A silicon rod is within the capillary, but unable to be seen due to the opacity of the CaO coating.

To account for the formation of $CaCO_3$, and subsequent release of CO_2, the decomposition temperature of $CaCO_3$ was determined. This is usually defined as the temperature when the Gibbs free energy of the reaction ($\Delta G°r$, joules) is equal to 0. The reaction equation for the decomposition of $CaCO_3$ is $CaCO_3 \rightarrow CaO + CO_2$ with $\Delta G°r = 168{,}400 - 144T$ [40] (T being the absolute temperature, K) yielding a decomposition temperature of roughly 1169K (896°C). This is slightly higher than the temperature range reported by Gallagher, *et al*. [41], who determined the decomposition temperature for $CaCO_3$ at various heating rates using Thermogravimetric Analysis (TGA). Applying this to the fiber draw, an additional hold step is implemented during heating.

The furnace is held at 900°C (below the 1414°C melting temperature of the Si) for 10 minutes to thermally decompose the $CaCO_3$ and allow for the off-gassing of CO_2.

The temperature is then increased to 1550°C and held for another 10 minutes to allow the Si to melt and consolidate towards the bottom of the preform. The temperature is then increased to 1950°C and fiber is drawn with a target fiber diameter of 125 μm. An acrylate polymer coating is applied during the draw to increase the mechanical durability of the overall fiber, yielding a final fiber diameter of ~250 μm.

Fibers were cleaved and inspected under an optical microscope to verify the core throughout the length of the fiber. Figure III.14 provides a representative electron micrograph of the core and cladding with a magnified image inset. The coating was removed from the fibers and the bare fibers were sleeved in a silica capillary tube (2.1 mm inner / 2.9 mm outer diameter) to be inserted in a 3 mm inner / 30 mm outer diameter silica preform. The preform was loaded in the optical fiber draw tower and drawn at 1950°C to a 1.5 mm outer diameter cane with 50” of water as an applied vacuum to

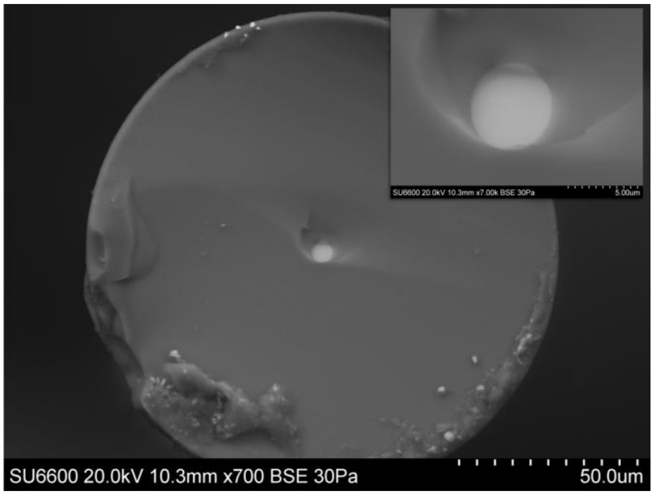

Figure III.14. Representative electron micrograph of the resulting silicon core fiber with a magnified image inset.

consolidate the cane. Pieces of the cane were cleaved and inspected under the optical microscope.

Figure III.15 provides an optical microscope image of the resulting stacked and redrawn fiber cross-section back illuminated at low magnification and high magnification (inset). Silicon, being opaque in the visible spectrum, would appear in these images as black spots where the visible light is absorbed. As shown, there is a darker, translucent region where the cores were expected, but other than debris on the facet, no black spots

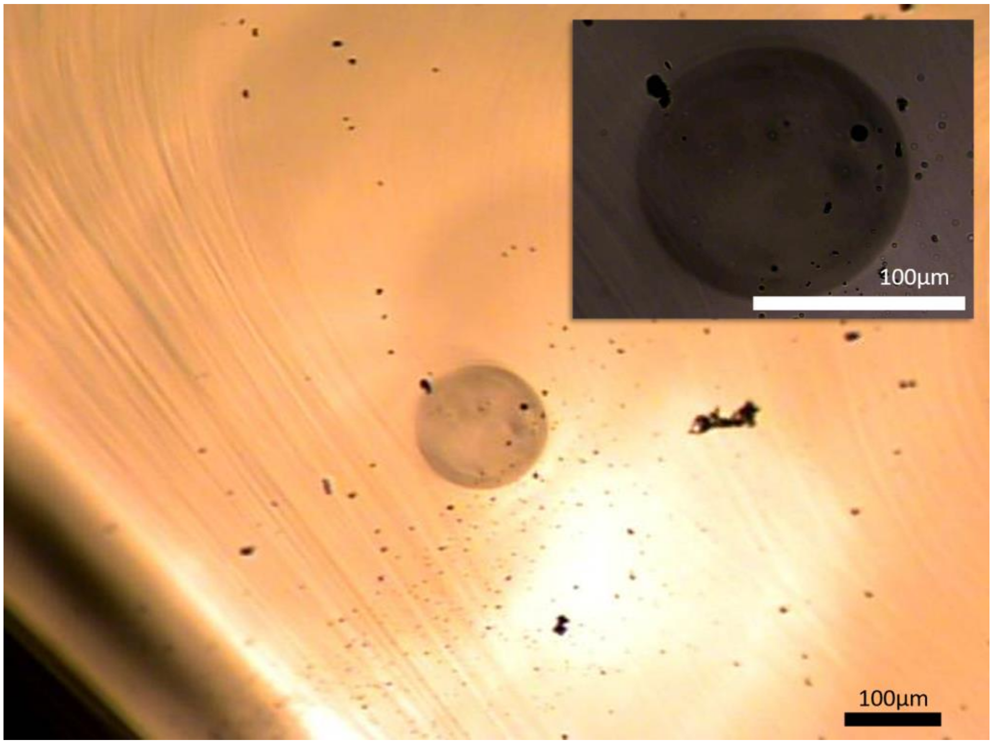

Figure III.15. Back-illuminated image of the stacked Si-core fibers drawn and consolidated. The darker region represents the location that the Si-sites were expected to be present. Inset is a magnified image of this region. The contrast is much lower as less light can pass through the core to the lens of the microscope.

are observed. The cores likely all oxidized during redrawing and, again, the semiconductor phase was lost. It is presently unclear the cause of the darker, translucent region.

While the CaO interfacial layer reduced the oxygen migration into the core during the first fiber draw, it proved unable to inhibit the migration during the second draw. The effectiveness of the interfacial layer during initial fiber drawing is believed to be due to the formation of a phase separated layer resulting from the eutectic melting point of CaO and SiO_2. The resulting phases consist of $CaSiO_3$ and SiO_2 [38], which serves to “bind” the SiO_2 limiting its ability to dissolve into the Si melt. The thickness of the interfacial layer is approximately 1 µm thick [38]. When redrawing for the stack, the interfacial layer likely remelts, along with the core, and becomes further diluted with the effectively endless surrounding silica cladding. As the intermediate layer then becomes highly silica rich, a $CaSiO_3$ phase may no longer be present to act as an effective oxygen sink. Additionally, since the silicon sites would be reducing in diameter, resulting in a higher surface area to volume ratio, the distance the oxygen ions need to diffuse to fully oxidize the silicon decreases. Unfortunately, these various hypotheses become notoriously difficult to validate, since the sites all convert to the same material as the surrounding cladding. Alternative semiconductor core fibers could potentially be investigated for obtaining a high Δn following this methodology, some of which will be described at the end of this dissertation in the “Future Work” section of Chapter VI.

III. F. Conclusions

Optical fibers were developed using a modified stack-and-draw technique and found to be disordered, as well as longitudinally invariant. This longitudinal invariance, contrary to the phase separated fibers of Chapter II, permitted waveguiding in the highly (transversely) disordered fibers. The versatility of the stack-and-draw method, coupled with the molten core method for the first time here, is demonstrated with the different microstructural architectures obtained by modifying the precursor fibers and the preform. The disordered microstructure of these fibers very nearly represents the 2D random array proposed by Abdullaev, *et al.*, [3] to observe TAL.

Various processing techniques on the precursor fibers are used to tailor the microstructure of the disordered cane closer to the target parameters. Etching the precursor fibers increases the disorder and reduces the pitch, while increasing the preform inner diameter, effectively allowing a bundle consisting of more fibers, can decrease the site dimensions. Alternatively, precursor fibers with larger or smaller core areas will likely influence the final site dimensions, though this was not directly investigated in this study.

When compared to the phase separated fibers of Chapter II, many of the averaged microstructural parameters were similar (Λ and Φ), although the index difference and longitudinal invariance were different. While the phase separated fibers yielded a significantly higher Δn, there was no apparent longitudinal invariance. As a result, the phase separated fibers scattered all of the incident light and no waveguiding being observed. Utilizing the stack-and-draw technique, longitudinal invariance over tens of centimeters was demonstrated, however a much lower Δn was obtained. Inasmuch, the fibers developed with the stack-and-draw technique were able to guide light and exhibited TAL over short distances.

It is believed the transverse scattering is resulting from the low refractive index difference between the high and low index phases. Even though precursor fibers made using the molten core method can possess core/clad refractive index differences greater than 0.05, when redrawing the fibers in a stack, the core likely remelts and dissolves more of the silica cladding, further diluting the dopant concentration. As a result, the final Δn becomes ~0.01, an order of magnitude smaller than the target value. As a result, TAL is observed in these fibers, though only over short lengths. Ultimately, a higher Δn, a higher degree of longitudinal invariance, and possibly a larger diameter core may be necessary to observe TAL over long lengths of fiber, though initially the stack-and-draw method utilizing MC-derived precursor fibers is an adequate technique for obtaining novel glass TALOF.

Semiconductor core fibers also were investigated, specifically silicon core silica clad fibers, to obtain significantly higher Δn, although engineering of the final disordered fiber was unsuccessful. Several other semiconductor core fibers have been developed consisting of lower melting temperature constituents that can be drawn in lower temperature glass preforms. Since diffusion is a thermally driven process, lower temperatures may reduce the oxygen migration into the core. Those routes may provide a viable method of retaining the high-index semiconductor phase after redrawing.

III. G. References

[1] T. Seward, “Elongation and Spheroidization of Phase-Separated Particles in Glass,” *Journal of Non-Crystalline Solids* **15**, 487-504 (1974).

[2] T. Seward, “Some Unusual Optical Properties of elongated phases in Glass,” *Physics of Non-Crystalline Solids*, 342-347 (1977).

[3] S. S. Abdullaev, and F. K. Abdullaev, “On propagation of light in fiber bundles with random parameters,” *Radiofizika*, **23**(6), 766-767 (1980).

[4] H. De Raedt, A. Lagendijk, and P. de Vries, “Transverse localization of light,” *Physical Review Letters* **62**(1), 47-50 (1989).

[5] T. Pertsch, U. Peschel, J. Kobelke, K. Schuster, H. Bartelt, S. Nolte, A. Tunnermann, and F. Lederer, “Nonlinearity and disorder in fiber arrays,” *Physical Review Letters* **93**(5), 053901 (2004).

[6] S. Karbasi, C. R. Mirr, P. G. Yarandi, R. J. Frasier, K. W. Koch, and A. Mafi, “Observation of transverse Anderson localization in an optical fiber,” *Optics Letters* **37**(12), 2304-2304 (2012).

[7] S. Karbasi, T. Hawkins, J. Ballato, K. W. Koch, and A. Mafi, “Transverse Anderson localization in a disordered glass optical fiber,” *Optical Materials Express* **2**(11), 1496-1503 (2012).

[8] M. Chen, and M.-J. Li, “Observing transverse Anderson localization in random air line based fiber,” in Photonic Properties of Nanostructures IV, vol. 8994. International Society for Optics and Photonics, 2014, pg. 89941S.

[9] J. Zhao, J. E. A. Lopez, Z. Zhu, D. Zheng, S. Pang, R. A. Correa, and A. Schülzgen, "Image transport through meter-long randomly disordered silica-air optical fiber," *Scientific Reports* **8**(1), 3065 (2018).

[10] T. Tuan, T. Cheng, S. Kuroyanagi, S. Tanaka, K. Nagasaka, T. Suzuki, and Y. Ohishi, "Fabrication of an all-solid tellurite disordered optical rod for transverse localization of light," *Lasers Congress 2016*, paper JTh2A.21.

[11] H. T. Tuan, S. Kuroyanagi, K. Nagasaka, T. Suzuki, and Y Ohishi, "Characterization of an all-solid disordered tellurite glass optical fiber and its near-infrared optical image transport," *Japanese Journal of Applied Physics* **58**(3), 2019.

[12] T. A. Birks, J. C. Knight, and P. St. J. Russell, "Endlessly single-mode photonic crystal fibers," *Optics Letters* **22**(13), 961-963 (1997).

[13] B. J Mangan, L. Farr, A. Langford, P. J. Roberts, D. P Williams, F. Couny, M. Lawman, M. Mason, S. Coupland, R. Flea, H. Sabert, T. A. Birks, J. C. Knight, and P. St. J. Russell, "Low loss (1.7 dB/km) hollow core photonic bandgap fiber," Optical Fiber Communications Conference Technical Digest, OSA 2004, paper PD24.

[14] C. Dunn, F. Kong, G. Gu, T. W. Hawkins, M. Jones, J. Parsons, A. Runnion, M. T. Kalichevsky-Dong, R. Salem, D. Liu, D. Gardner, P. Fendel, R. Synowicki, E. Cheung, J.-T. Gomes, L. Lavoute, D. Gaponov, S. Fevrier, and L. Dong," Solid Tellurite Optical Fiber Based on Stack-and-Draw Method for Mid-IR Supercontinuum Generation," *Fibers* **5**(4) 1-11 (2017).

[15] J. Broeng, D. Mogilevstev, S. Barkou, and A. Bjarklev, "Photonic Crystal Fibers: A New Class of Optical Waveguides," *Optical Fiber Technology* **5**(3), 305-330 (1999).

[16] P. Russell, “Photonic Crystal Fibers,” *Science* **299**, 358-362 (2003).

[17] A. Mafi, M. Tuggle, C. Bassett, E. Mobini, and J. Ballato, “Advances in the fabrication of disordered transverse Anderson localizing optical fibers,” *Optical Materials Express* **9**(7), 2769-2774 (2019) **Invited Review Article**.

[18] J. Ballato and A. C. Peacock, “Perspective: Molten core optical fiber fabrication – A route to new materials and applications,” *APL Photonics* **3**, 120903 (2018).

[19] M. Cavillon, J. Furtick, C. Kucera, C. Ryan, M. Tuggle, M. Jones, T. Hawkins, P. Dragic, and J. Ballato, “Brillouin Properties of a Novel Strontium Aluminosilicate Glass Optical Fiber,” *Journal of Lightwave Technology* **34**, 1435-1441 (2016).

[20] J. Buhler, F.-P Steiner, and H. Baltes, “Silicon dioxide sacrificial layer etching in surface micromachining,” *Journal of Micromachining and Microengineering* **7**, R1-R13 (1997).

[21] P. Wrobel, T. Stefaniuk, T. J. Antosiewicz, A. Libura, G. Nowak, T. Wejrzanowski, M. Andrzejczuk, K. J. Kurzydlowski, K. Jedrzejewski, and T. Szoplik, “Fabrication of corrugated Ge-doped silica fibers,” *Optics Express* **20**(13), 14508-14513 (2012).

[22] W. G. Palmer, “The Action of Aqueous Hydrofluoric Acid on Silica,” J*ournal of the Chemical Society*, 1656-1664 (1930).

[23] J. Judge, “A Study of the Dissolution of SiO_2 in Acidic Fluoridic Solutions,” *Journal of the Electrochemical Society* **118** (11), 1772-1775 (1971).

[24] D. J. Monk, D. Soane, and R. T. Howe, “A review of the chemical reaction mechanism and kinetics for hydrofluoric acid etching of silicon dioxide for surface micromachining applications,” *Thin Solid Films* **232**, 1-12 (1993).

[25] S. Verhaverbeke, I. Teerlinck, C. Vinckier, G. Stevens, R. Cartuyvels, and M. M. Heyns, “The etching mechanisms of SiO_2 in hydrofluoric acid,” *Journal of the Electrochemical Society* **141**(10), 2852-2857 (1994).

[26] A. Mitra, and J. D. Rimstidt, “Solubility and dissolution rate of silica and acid fluoride solutions,” *Geochimica et Cosmochimica Acta* **73**, 7045-7059 (2009).

[27] P. Pace, S. T. Huntington, K. Lyytikainen, A. Roberts, and J. D. Love, “Refractive index profiles of Ge-doped optical fibers with nanometer spatial resolution with atomic force microscopy,” *Optics Express* **12**(7), 1452-1457 (2004).

[28] A. Agrawal, and M. Tomozawa, “Correlation of silica glass properties with the infrared spectra,” *Journal of Non-Crystalline Solids* **209**(1-2), 166-174 (1997).

[29] S. Karbasi, “Transverse Anderson Localization in Disordered Optical Fiber,” Ph.D. dissertation, University of Wisconsin-Milwaukee, 2014.

[30] A. Mafi, J. Ballato, K. Koch, and A. Schulzgen, “Disordered Anderson Localization Optical Fibers for Image Transport – A Review,” *Journal of Lightwave Technology* **37**(22), 5652-5659 (2019). **Invited Review Article**.

[31] W. Tian, H. Zhang, L. Xi, W. Zhang, and X. Tang, “A circular photonic crystal fiber supporting 26 OAM modes,” *Optical Fiber Technology* **30**, 184-189 (2016).

[32] S. Karbasi, C. Mirr, R. Frazier, P. Yarandi, K. Koch, and A. Mafi, “Detailed investigation of the impact of the fiber design parameters on the transverse Anderson localization of light in disordered optical fibers,” *Optics Express* **20**(17), 18692-18706 (2012).

[33] J. Ballato, T. Hawkins, P. Foy, R. Stolen, B. Kokuoz, M. Ellison, C. McMillen, J. Reppert, A. M. Rao, M. Daw, S. R. Sharma, R. Shori, O. Stafsudd, R. R. Rice, and D. R. Powers, "Silicon optical fiber," *Optics Express* **16**(23), 18675–18683 (2008).

[34] I. H. Malitson, "Interspecimen comparison of the refractive index of fused silica*,"* *Journal of the Optical Society of America* **55**, 1205-1208 (1965).

[35] C. Schinke, P. C. Peest, J. Schmidt, R. Brendel, K. Bothe, M. R. Vogt, I. Kröger, S. Winter, A. Schirmacher, S. Lim, H. T. Nguyen, D. MacDonald, "Uncertainty analysis for the coefficient of band-to-band absorption of crystalline silicon," *AIP Advances* **5**, 67168 (2015).

[36] M. Nakamoto, J. Lee, and T. Tanaka, "A model for estimation of viscosity of molten silicate slag," *Transactions of the Iron and Steel Institute of Japan* **45**(5), 651-656 (2005).

[37] M. J. Assael, I. J. Armyra, J. Brillo, S. V. Stankus, J. Wu, and W. A. Wakeham, "Reference data for the density and viscosity of liquid Cadmium, Cobalt, Gallium, Indium, Mercury, Silicon, Thallium, and Zinc," *Journal of Physical and Chemical Reference Data* **41**, 033101 (2012).

[38] E. Nordstrand, A. Dibbs, A. Eraker, and U. Gibson, "Alkaline oxide interface modifiers for silicon fiber production," *Optical Materials Express* **3**(5), 651-657 (2013).

[39] S. Morris, T. Hawkins, P. Foy, C. McMillen, J. Fan, L. Zhu, R. Stolen, R. Rice, and J. Ballato, "Reactive molten core fabrication of silicon optical fiber," *Optical Materials Express* **1**(6), 1141–1149 (2011).

[40] D. Gaskell, *Introduction to the Thermodynamics of Materials 5th ed.*, (New York, NY: Taylor & Francis Group, LLC. 2008.) Ch. 10, pp. 263-303.

[41] P. K. Gallagher and D. W. Johnson Jr., “The effects of sample size and heating rate on the kinetics of the thermal decomposition of $CaCO_3$,” *Thermochemica Acta* 6, 67-83 (1973).

CHAPTER FOUR

INVESTIGATION OF ALL-SOLID ACTIVELY-DOPED TRANSVERSE ANDERSON LOCALIZING OPTICAL FIBERS

IV. A. Introduction

Most of the glass-based transverse Anderson localizing optical fibers (TALOFs) reported within the literature thus far have been comprised of silica, with air as the scattering component [1-3]. The only exclusion to-date being the tellurite all-glass TALOF developed by T. Tuan, *et al*. [4]. As a result, many of the reported applications of these novel TALOFs have been passive, such as image transport [3,5-6] or beam multiplexing [7] since the aforementioned efforts using silica were not in a position to actively dope that glass. In only one instance is a report of an active application in these fibers; that of random lasing based on an organic dye infused into the air pores of a silica / air TALOF [8]. There is a vast realm of optical fiber lasers [9-12] and amplifiers [13-17] that could be investigated using these novel TALOFs. Since only one active TALOF has been reported in the literature [8] as of the writing of this Dissertation, little is known about the impact of transverse Anderson localization on fiber lasing or amplification. This brings up interesting questions regarding the capability for these TALOFs to operate as high-energy lasers. What are the limitations regarding power scaling with the impact of TAL on nonlinear thresholds, such as Spontaneous Brillouin or Raman Scattering (SBS, SRS)? Does the TAL waveguiding have any novel influence on heat mitigation during lasing? How does the localization impact the efficiency of lasing or amplification?

Can amplification occur across the entire localizing core and could this be useful for space division multiplexing?

This chapter explores the fabrication and properties of the first rare-earth doped all-solid TALOFs realized by combining the stack-and-draw methodology discussed through Chapter III with active (ytterbium-doped or erbium-doped) molten core fiber processing. The aim is to create and begin to understand the development of these fibers as a future platform to answer these fundamental questions regarding solid-state lasing or amplification in TALOFs.

IV. B. Development of ytterbium-doped TALOF

The precursor (molten core) fiber core composition was modified to include Yb as the potential lasing ion in a TALOF. The precursor fibers were derived from a mixed powder composition comprising of 58.46% Al_2O_3 – 36.54% SrO – 5.00% Yb_2O_3 in mol% (same 8:5 ratio of Al_2O_3 – SrO as previous precursor fibers) and drawn under the same conditions as the precursor fibers used in subsequent stacks (Section III. B.). These fibers (125 μm OD) were stripped of the acrylate coating using a razor blade, placed in a box furnace for 30 minutes and heated to ~600°C to remove any organic residue on the surface, and subsequently wet etched in hydrofluoric acid (HF) for 17, 20, and 22 minutes to remove roughly 51, 60, and 66 μm respectively from the cladding. The fibers were bundled in a 5.4 mm by 6.8 mm silica tube and inserted in a 7.8 mm inner / 30 mm outer diameter preform and loaded into the draw tower. Cane 4 (DC4) was drawn at 1950°C under a vacuum of 15” Hg to consolidate the core. Figures IV.1a-c provide

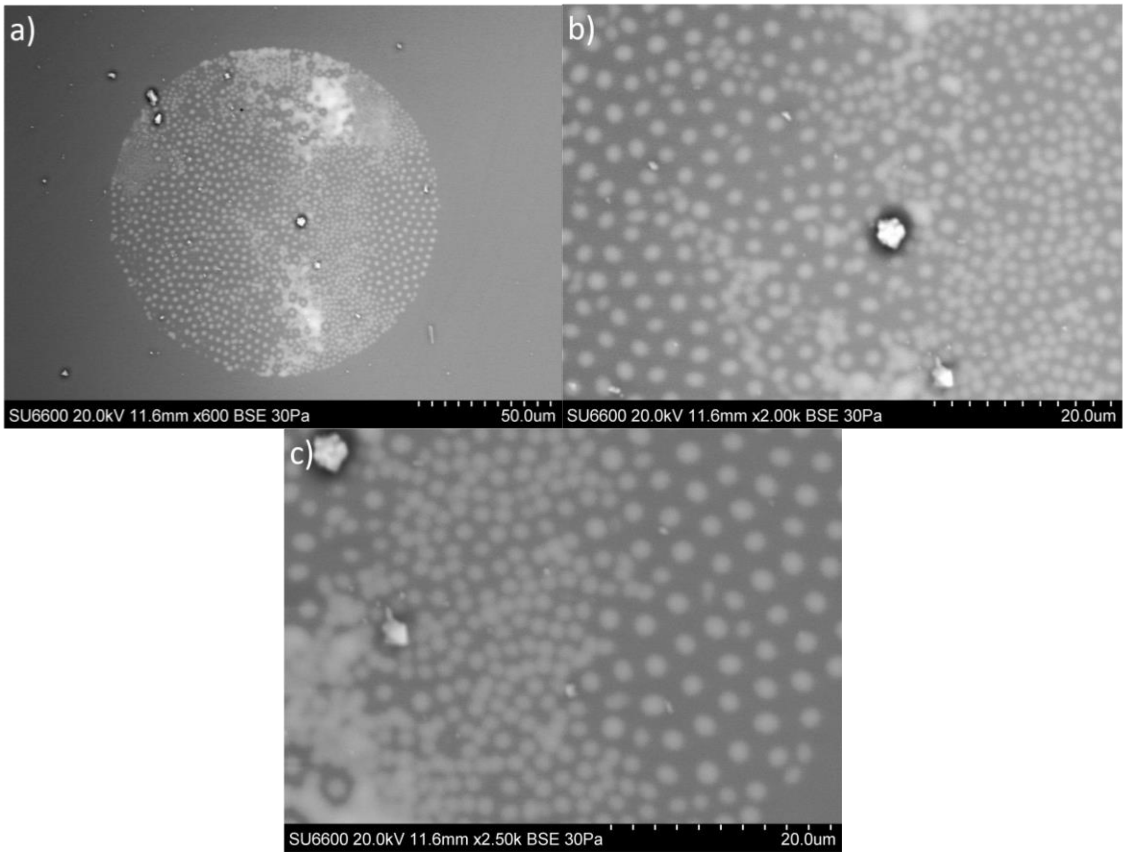

Figure IV.1 Electron micrographs of DC4 at a) 600x, b) 2000x, and c) 2500x magnification

representative electron micrographs of Cane 4 at 600x, magnified 2000x, and 2500x respectively. The draw temperature was lowered relative to the previous stacked fibers to minimize the dilution of the core composition by the surrounding silica cladding [18].

The cross-sections of DC4 portrayed a somewhat unexpected architecture. As shown in Figure IV.1.a, “splotches” of the high index phase are present, and there are distinct regions with large (~2 μm) and small (< 0.5 μm) pitches. Even with the precursor fibers being etched for a slightly longer time (22 minutes), it was expected that roughly

30 μm of silica remained surrounding the core of the precursor fibers and should be present between the high index phases. Neglecting the "splotches," the maximum fill-ratio (high to low index phase) was found to be 0.53 and a minimum of 0.22 with the average microphase diameter of 1.56 μm. Compared to the target values described in Chapter II, the overall average fill ratio is somewhat lower than desired (0.5), however the average pitch and microphase diameter are on the same order of the magnitude of light (1 µm).

A 1 m long sample was cleaved every 10 cm and inspected under an SEM (Hitachi SU-6600) to verify longitudinal invariance. Figures IV.2.a-d provide four electron micrographs showing 0, 30, 60, and 80 cm along the piece. Slight changes in the microstructure are observed along at least 80 cm of the cane (arrows provided as a visual aid). Interestingly, air bubbles are still present along the fiber that when inspected longitudinally under a light microscope, were elongated (Figure IV.2.e). These air bubbles minimize longitudinal invariance along the fiber, which likely results in scattering losses. Localization measurements were made in regions away from the air holes to avoid the impact of the high index difference of silica and air on the localization.

Since the microphases are too small in the bulk sample to be accurately probed with EDX, the FIB was used to lift-out and ion polish a sample of the core to 100 nm thickness and probed for composition following the procedure outlined in Chapter II.C.2. Figure IV.3a is an electron micrograph of the fiber facet with a box labeling the region to be lifted out and Figure IV.3b shows the corresponding region with the higher and lower index phases labeled. The contrast is low in Figure IV.3a because the surface of the fiber

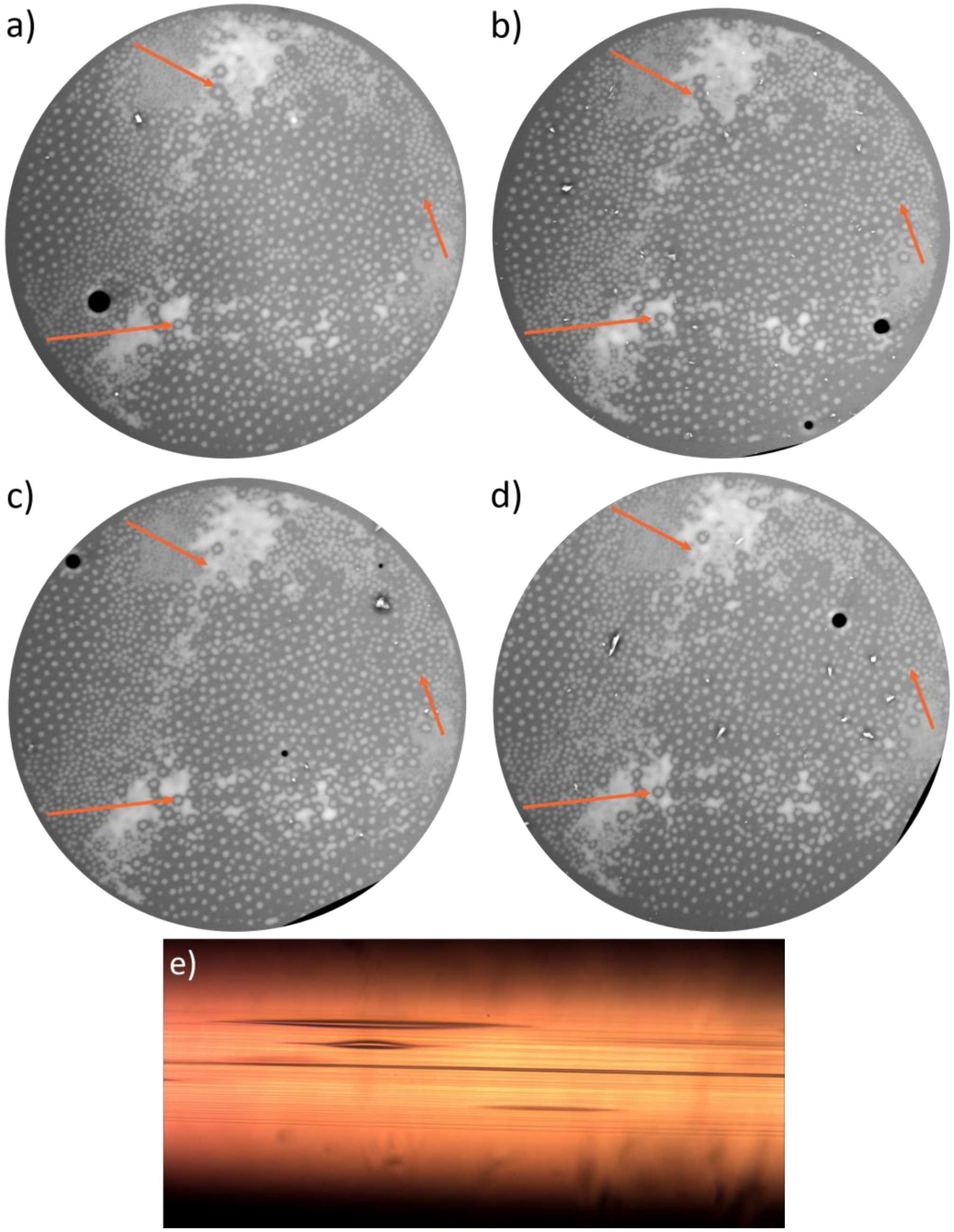

Figure IV.2. Representative electron micrographs at 700x magnification of DC4 taken along 1 m of cane with a) being the beginning (0 cm), b) taken at 30 cm, c) 60 cm, and d) 80 cm. e) is a light microscope image of the longitudinal axis showing the air bubbles. The arrows provide a visual aid to show the longitudinal invariance.

is coated in platinum to make the sample conductive, and in Figure IV.3b because the compositional difference is small between the higher and lower index phases. Black lines are added on either side of the higher index phase in Figure IV.3.b to aid the reader. The measured composition (mol%) and calculated refractive indices of the high and low index phases along with the precursor fiber for reference are provided in Table IV.1. Interestingly, the Al/Sr ratio (originally 8:5) increased in the final higher index phase (suggesting less SrO in the final phase than would be expected). This disparity (roughly 0.2 mol% of Al_2O_3) is likely a result of the compositional analysis (resolution of the EDX when probing glass), however further studies are necessary to validate this claim.

The refractive indices were calculated in the same manner as in Chapter II and the refractive index difference (Δn) determined to be ~0.01, an order of magnitude lower than targeted. Upon redrawing the precursor fibers, the "cores" (high-index phases) are diluted further by the surrounding silica, resulting in more than a 25% decrease in relative dopant concentration [18]. This is likely due to the core remelting and dissolving more of the silica during the stack-and draw process [18] instead of solely elongating by viscous flow. Since the effective radii of the fiber cores in the stack are so small (~15 μm), there is less volume for the silica to diffuse through. This means that as the core melts, the silica from the cladding will quickly diffuse through to the center of the core, resulting in the dopant dilution occurring long before the final fiber is drawn from the furnace [18]. The surrounding silica (lower-index phase) migrating into the cores (higher-index phase) during redrawing could explain why the core diameters decrease less than expected during redrawing and why less silica was observed between the higher index phases. Table IV.2 provides the overall microstructural properties of DC4, along with the target parameters.

Localization measurements were conducted on various lengths of fiber using a He-Ne laser source (632.8 nm) and TAL was verified in DC4 for lengths of fiber up to

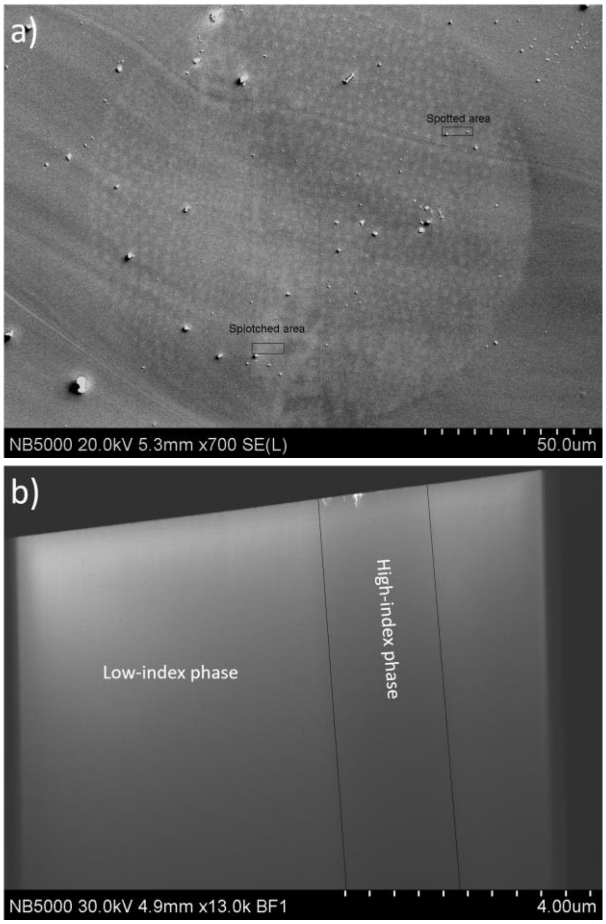

Figure IV.3. a) Electron micrograph of DC4 coated in platinum with the region to be lifted out labeled as “Spotted area,” and b) corresponding lifted-out region. Black lines were included to the lifted-out region to help the reader differentiate the two phases.

Table IV.1. Measured compositions of the higher index phase, lower index phase and precursor fibers, along with the calculated refractive indices.

	SiO_2 (mol%)	Al_2O_3 (mol%)	SrO (mol%)	Yb_2O_3 (mol%)	n
High Index Phase	96.60	1.98	1.09	0.33	1.4548
Low Index Phase	100.00	0.00	0.00	0.00	1.4444
Precursor Fiber (beginning)	70.34	20.96	6.74	1.96	1.5284
Precursor Fiber (end)	75.25	15.71	7.77	1.27	1.5156

Table IV.2. Microstructural properties of the disordered cane DC4 compared with target values, including the refractive index difference (Δn), the core diameter (Φ_{core}), microphase diameter ($\Phi_{microphase}$), and pitch (Λ). Target parameters deduced from [19].

Material Parameter	**Target**	**DC4**
Δn	0.10	0.01
Φ_{core}	150 μm	117 μm
Max Fill Ratio	0.50	0.53
Min Fill Ratio	0.50	0.22
$\Phi_{microphase}$	1.00 μm	1.56 μm
Λ	1.00 μm	1.18 μm

almost 1 m long. Figure IV.4.a shows the output facet a 94 cm long piece of DC4 recorded on a CCD camera as light from the He-Ne laser source is coupled to different regions. The appearance of a single high intensity mode suggests strong TAL. The exposure time was increased on the CCD to increase the brightness along the entire facet

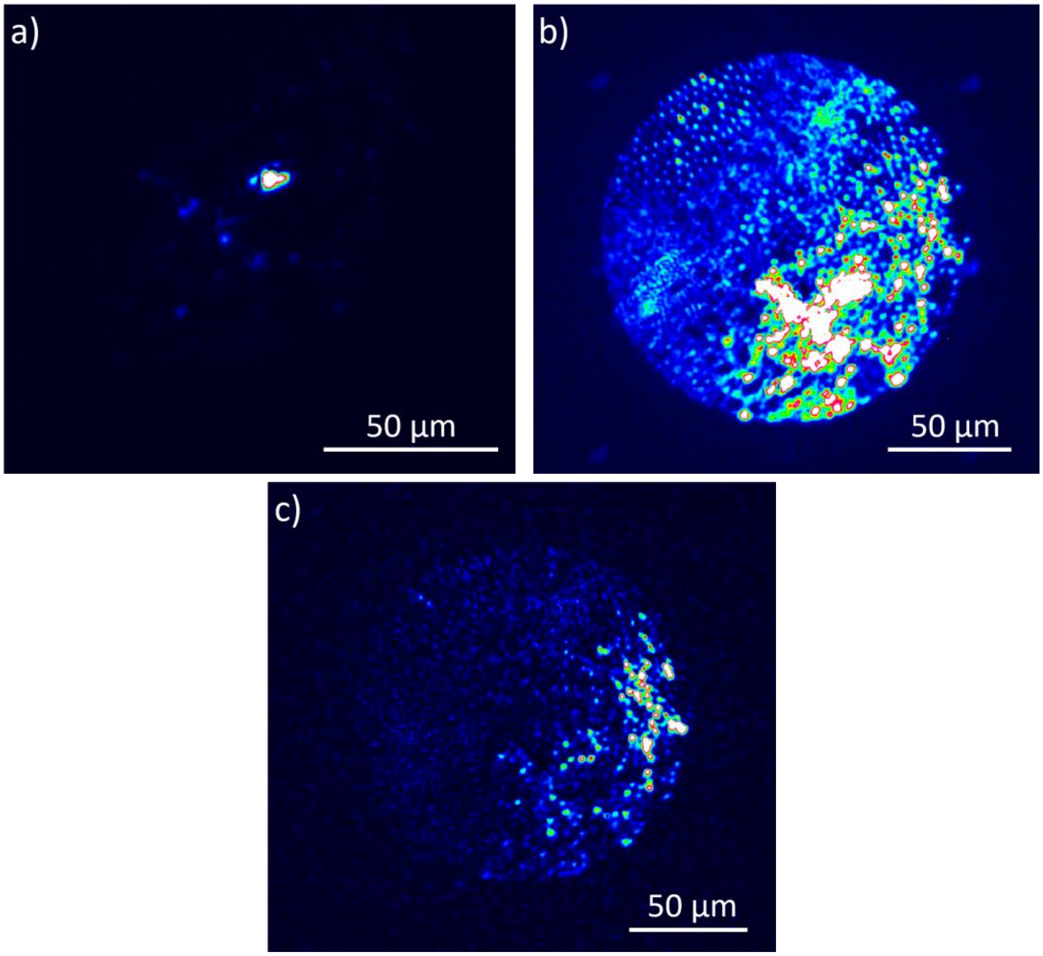

Figure IV. 4. CCD images of the output from a 94 cm long piece of DC4 showing a) strong localization, b) the same mode with high exposure to show the localization position in the facet of the fiber, and c) a weakly localized mode. All images were taken from different modes in the same fiber.

with the strongly localized mode still excited (Figure IV. 4.b) to provide a visual comparison against a weakly localized mode observed elsewhere in the fiber facet (Figure IV.4.c). As shown in Figure IV.4.b, with the exposure time increased, the high intensity mode becomes indistinguishable. Similarly, a single, high intensity mode is not observed in the weakly localizing region, even at low exposure times.

IV. C. Lasing characteristics

With TAL verified in DC4, a linear laser cavity was constructed using this TALOF. First, background losses (α) were measured in various localized modes with the fiber in the laser cavity using a He-Ne laser of known intensity and the cutback method to determine an ideal length. For lasing to occur, the loss needs to be lower than the gain. The α was measured to be between 0.6-1.2 dB/cm for different modes. This is higher by a factor of about 100 and admittedly unexpected for these fibers in that the precursor fibers themselves possessed loss values on the order of dB/m [20-22]. It is noted that there are high levels of uncertainties with this measurement. Firstly, it is assumed that every measurement was taken with no change to the input conditions of the laser to the localized mode. Since the input laser was moved to different modes to measure the output powers at decreasing lengths, it is probable that the input conditions were different for the various modes. Additionally, it is assumed that of all the output power measured using the powermeter is from light coupled solely into the single localized mode. Further studies are necessary to understand the overarching loss mechanisms within the modes of these fibers and to better understand and ultimately characterize the loss in these fibers. However, from a lasing standpoint, shorter lengths of fiber should be pumped to accommodate for this high loss.

Initial lasing experiments were conducted using a 5 cm long sample of DC4 that was cleaved using a Vytran large diameter fiber cleaver (Thorlabs) to ensure pristine surfaces and butt-coupled to a dielectric mirror to minimize cavity losses. A He-Ne laser was used to locate and excite various localized modes. Figure IV.5.a is an image of the output of DC4 with the He-Ne coupled into a localized mode. As shown, even though the laser light is coupled into a localized mode (depicted by the bright high-intensity spot), there is some light leakage into the remaining core. This could provide some insight into the high background losses measured for the various modes, in that not all the input light is confined in the localized mode. This mode leakage is likely due to the low Δn between the phases or longitudinal inhomogeneities leading to scattering losses. Figure IV.5.b is a CCD of a representative localized mode excited using the He-Ne to provide a visual.

Once a strongly localized mode was excited, the He-Ne laser was turned off and the pump laser source switched to a 976 nm laser traversing the same beam path. The output facet was imaged on a CCD (Figure IV.6.a) and the emission was recorded on an Optical Spectrum Analyzer (OSA) for 3 different pump powers (Figure IV.6.b). The expected emission for Yb $^5F_{5/2} \rightarrow {}^5F_{7/2}$ transition occurs at 1050 nm [20] so the OSA was set to record from 900 to 1200 nm. Interestingly, the localized beam (observed previously with the He-Ne laser) is no longer observable at 976 nm with the CCD, which suggests delocalization. This is unexpected since the localization behavior is expected to be independent of input wavelength [23]. A key indication of lasing is a narrow (< 1 nm) linewidth emission [24]. Otherwise, if broad peaks are observed, the emission is considered spontaneous emission. The output emission recorded on the OSA is broad

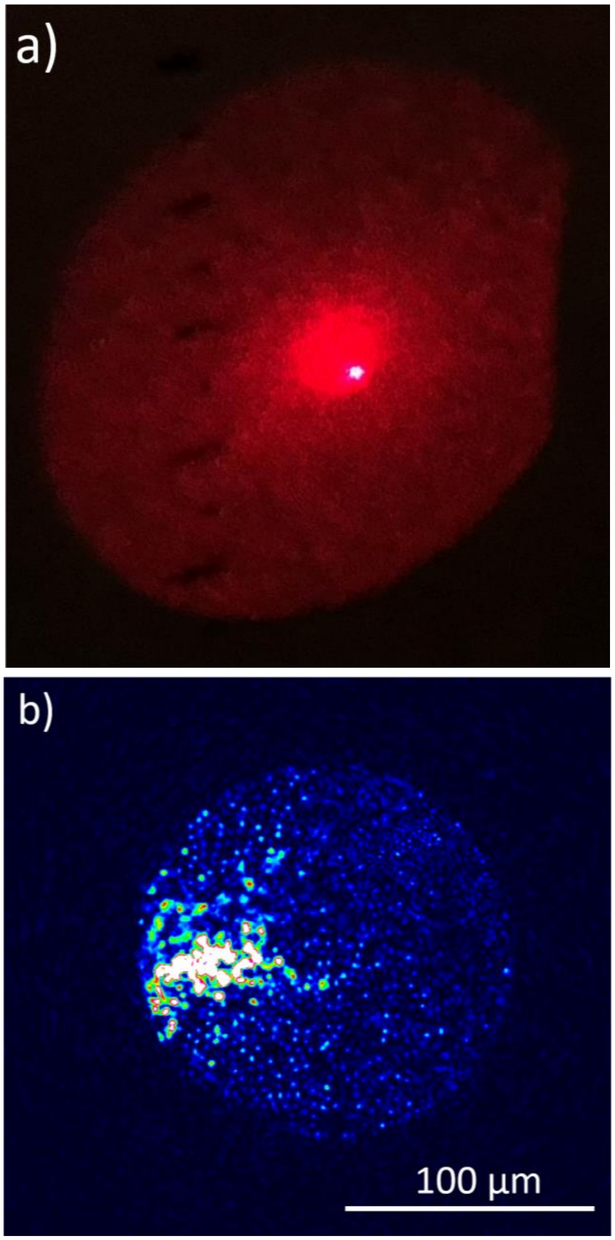

Figure IV.5. a) output of a TALOF pumped with a He-Ne coupled into a localized mode imaged on paper and b) a representative CCD image of a localized mode when pumped with a He-Ne. The two figures are of different modes in the same fiber.

(100 nm) and characteristic of spontaneous emission of Yb^{3+} [25]. The slight shift of the pump peak (976 to 970 nm) is attributed to improper calibration of the OSA. It is possible that at these pump powers, the Yb ions are absorbing the pump energy and spontaneously reemitting in all directions, effectively masking the localization. Additionally, the fiber was visibly fluorescing a blue-green, suggested in literature as cooperative emission of

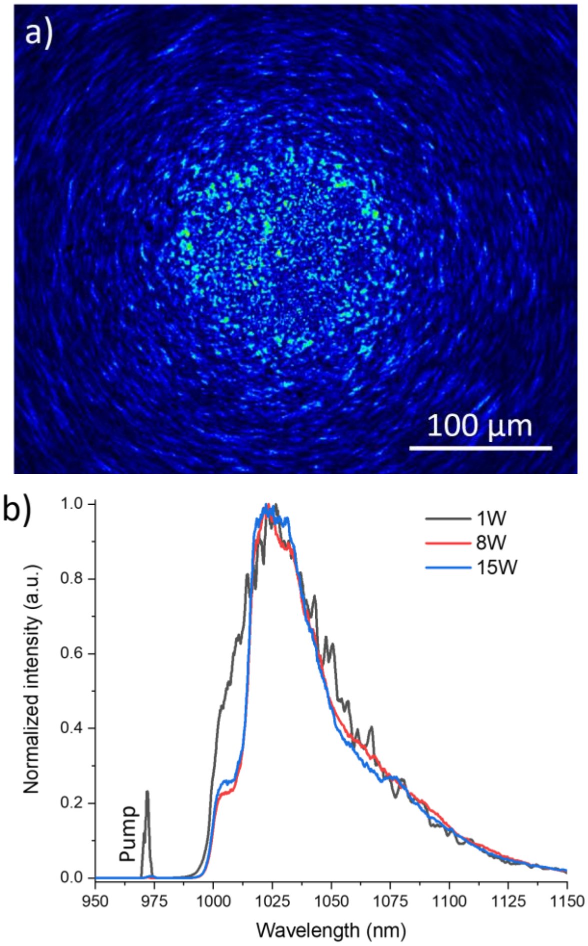

Figure IV.6. a) Output facet of a de-localized mode in a Yb-doped TALOF pumped with 976 nm and b) resulting emission spectra suggesting spontaneous emission of Yb^{3+}.

Yb^{3+} [26], which may also influence the delocalization and spectroscopic behavior. Cooperative emission suggests that the ions are too densely populated in the glass, allowing for energy transfer between neighboring ions. This should be verified by investigating the emission from 400 – 600 nm and comparing the resulting emission spectra with the one reported in Ref. 26. For lasing to occur (neglecting the high background losses), the concentration of Yb should be decreased in future fibers.

Investigating this delocalization further, the 5 cm long sample of DC4 was pumped with a tunable Ti:Sapphire laser from 960 to 990 nm. When pumped at 960 nm, a strongly localized mode was observed. This wavelength was used to align the laser to ensure sufficient coupling into the localized mode. The laser wavelength was then varied from 960 nm to 970, 976, 980, and 990 nm and the output emission recorded on a CCD. Figures IV.7 a-e are the resulting CCD images of the output facet when pumped with the various wavelengths. As shown, strong localization is first observed at 960 nm. At 970 nm, the strong localization is still observed, however some slight emission was also observed in surrounding regions of the core. At 976 and 980 nm, complete delocalization occurs, and at 990 nm the beam is relocalized. It must be noted that the alignment of the beam and the position of the fiber was not shifted during any of these experiments. The delocalization therefore must be a result of the absorbing ion and the pump wavelength.

The input wavelengths were plotted against an absorption spectrum for a Yb-doped fiber laser of a similar composition (fiber and data presented in Ref. 20) and is shown in Figure IV. 8. The compositions of the fibers discussed in Ref. 20 contain fluorine and therefore, some features of the absorption spectra differ from that of a

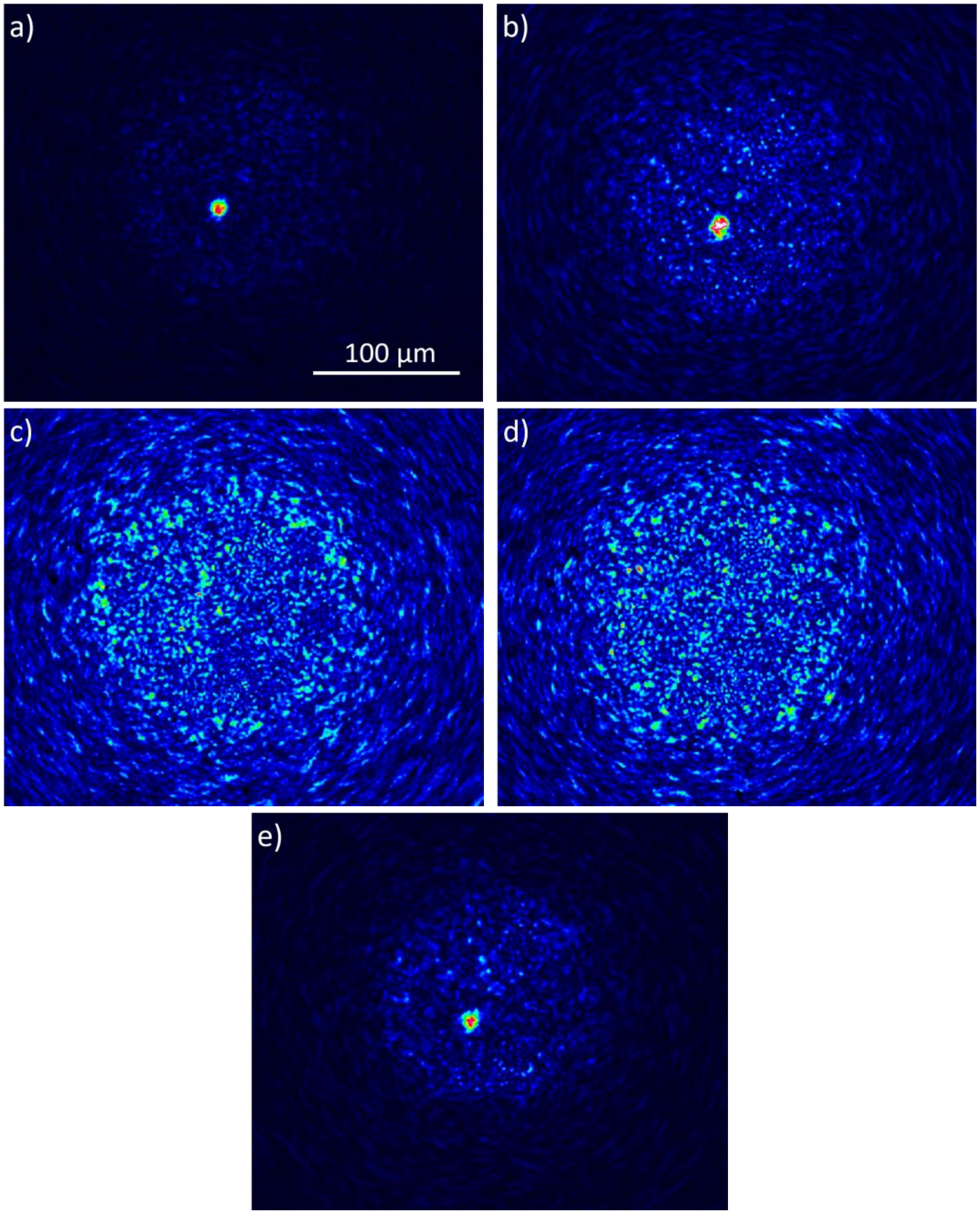

Figure IV.7. The output of the TALOF measured on a CCD pumped with a tunable Ti:Sapphire laser at a) 960 nm, b) 970 nm, c) 976 nm, d) 980 nm, and e) 990 nm. The scale bar is the same for all images.

commercial Yb-doped fiber laser. The purpose of this plot, however, is to portray the absorption bandwidth of MCM-derived Yb-doped fiber lasers doped with both SrO and Al_2O_3. At 960 nm, the pump energy is outside of the primary absorption band and localization is maintained. At 970 nm, the pump wavelength is at the cusp of the absorption peak and most of the localization is maintained, though some slight emission is observed elsewhere in the facet of the fiber. At 976 and 980 nm, the pump wavelength is within the absorption band and the localization is lost. Finally, at 990 nm, the pump is outside of the absorption band and localization is observed. This further supports the

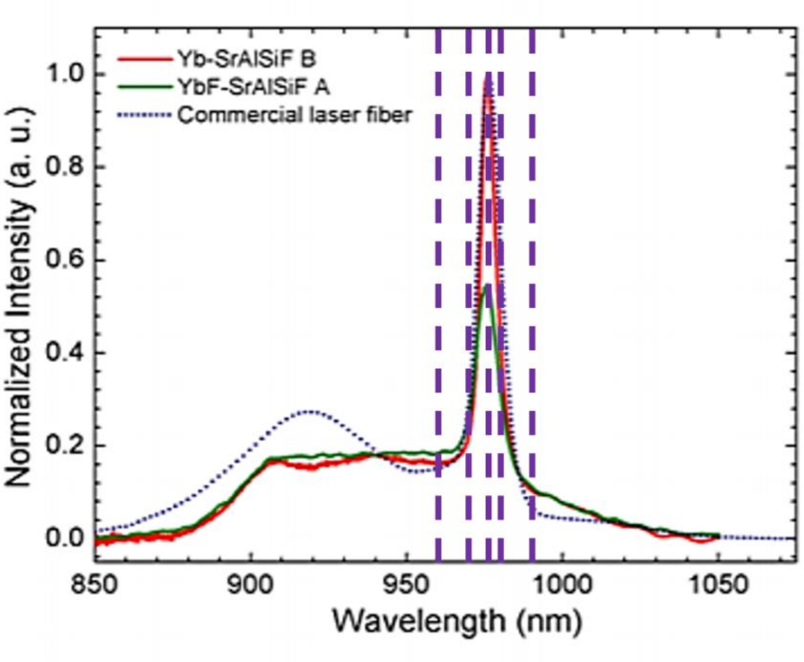

Figure IV.8. Representative absorption spectra for a Yb-doped SrAlSiO derived optical fiber obtained from Ref. 20 with the pump wavelengths overlaid from 960 – 990 nm (purple dashes).

conclusion that the Yb^{3+} ions absorb the incoming light and spontaneously reemit in all directions. This spontaneous reemission is likely masking the localization (not) observed in the output. These observations corroborate the theoretical analysis of Gökbulut and Inci [27], who investigated the effect of spontaneous emission on TAL in hyperbolic waveguides. It is possible some of the delocalization results from longitudinal inhomogeneities, though if this were the case, all incident light tested (~500 – 1000 nm) should be impacted similarly.

Lasing is highly directional [24] and therefore would redirect the emission along the fiber, potentially re-localizing the beam. However, initial attempts at lasing a 5 cm long piece of DC4 were unsuccessful up to a pump power of 15 W. As mentioned previously for lasing to occur the gain (Yb^{3+} concentration) needs to be higher than the loss (scattering). However, if the Yb^{3+} concentration is too high, cooperative emission can occur. In these experiments, background losses were significantly high (dB/cm) and cooperative emission was observed, suggesting too high of a Yb^{3+} concentration. For efficient lasing, the precursor composition must be tailored to decrease the Yb concentration in the glass to reduce cooperative emission, and losses must be improved. Unfortunately, very little work has been done studying loss mechanisms within these novel TALOFs to provide insight into how to improve these fibers for future lasing experiments. It is imperative that the loss mechanisms be well understood to optimize these TALOFs for future applications.

IV. D. Amplification in an Er-doped TALOF

While the spontaneous emission resulting in delocalization might be detrimental for a TALOF laser, this phenomenon might have some benefit in an optical amplifier. If a certain localized mode is pumped at low intensities, and the ions spontaneously emit in all directions, this could simultaneously pump other localized modes across the facet of the fiber as a form of tandem pumping. Seed sources localized in other Anderson localized modes could potentially be amplified. Also, an interesting feature of TALOFs are the intrinsic ability for spatial multiplexing [7]. An erbium (Er) doped TALOF may then be able to act as an efficient optical amplifier for multiple distinct input beams.

In an attempt to study amplification properties in these TALOFs, and to begin investigating a spatial multiplexing TAL erbium-doped fiber amplifier (EDFA), precursor fibers were developed and drawn using the same base composition as with all prior draws (8:5 molar ratio of Al_2O_3 – SrO), although doped with 2.5 mol% Er_2O_3 instead of Yb_2O_3. For completeness, the precursor powder composition (used to develop the MCM-derived fiber) was 60% Al_2O_3 – 37.3% SrO – 2.5% Er_2O_3 in mol%. The fabricated fibers were cut to size, coating removed, acid etched, and stacked in a 7.8 mm x 30 mm preform. This bundle was then drawn to the final disordered cane (DC5) under similar draw conditions as DC4. Figure IV.10.a is a representative electron micrograph of the resulting microstructure. Localization was confirmed with a He-Ne laser to attempt to avoid the absorption bands of Er^{3+} [28], however only weak localization was observed over a few cm (< 5cm). Longer samples were also probed but no localization was observed. The 632.8 nm pump is close to the ${}^4I_{15/2} \rightarrow {}^4F_{9/2}$ transition [28], which could potentially

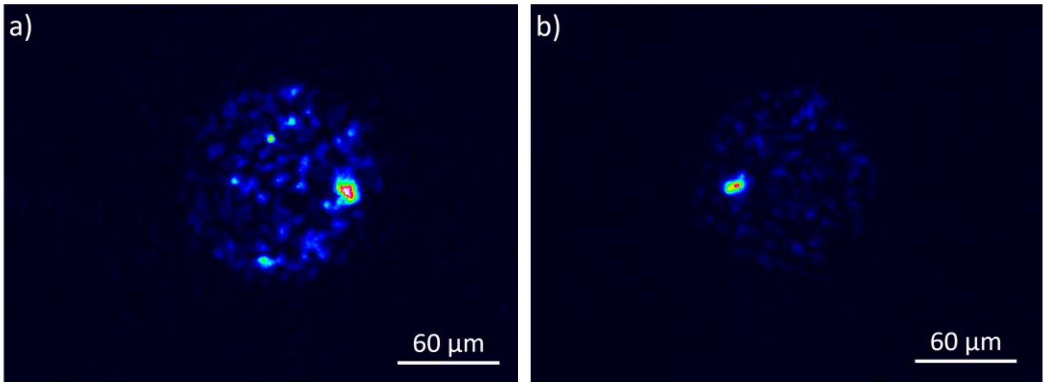

Figure IV.9. CCD images portraying the localization in short lengths (5 cm) of DC5 when pumped with a HeNe laser.

explain some of the delocalization or spontaneous emission elsewhere in the facet. As described with respect to the Yb-doped TALOF, pumping with a wavelength even on the cusp of the absorption band results in some spontaneous emission, effectively masking the localization. Figure IV.9.b-c are CCD images of the resulting localization. Further localization tests should be conducted with pump wavelengths outside of the absorption bands, however present studies were limited by the availability of laser sources.

Unfortunately, this delocalization over short lengths (5 cm) adds a level of complexity when aligning the 1550 nm seed source to a localized mode. Generally, a He-Ne laser was used first to align into the localized mode through free-space optics, and then a subsequent laser traversing the same beam path is used to pump the rare earth ions. Compared to Yb^{3+}, Er^{3+} has a more complex energy diagram with far more possible higher energy states, thereby more absorption bands [28]. This, in conjunction with most commercially available laser pumps specifically designed for pumping *within* these absorption bands, makes studying the Er-doped TALOF a challenge in and of itself.

Upon the completion of this Dissertation, these amplifier experiments were underway by collaborators at the University of New Mexico. Since the loss mechanism is not well understood in these fibers, and passive pumping the Er-doped TALOF remains a challenge, the performance (and understanding) of these actively doped TALOFs is limited.

Depending on the amplification performance of pumping the various localized modes with the spontaneous emission, another option for pumping the Er-doped TALOF amplifier could be to side-pump the fiber at 976 nm, effectively flooding the cross-section, and seeding the localized modes. It would be interesting to compare the efficiency of the two pumping schemes. Additionally, while the spontaneous emission might be an unanticipated challenge, rather clever techniques methods of incorporating light absorbing claddings in optical fibers has been explored for decades [29] including more recently, double-clad EDFAs with the inner clad doped with samarium (Sm) [30-32]. The absorption spectra of Sm overlaps with the amplified spontaneous emission (ASE) spectra of Er and can effectively filter the amplification wavelength [30,32]. A next-generation iteration of this Er-doped TALOF could have a secondary ring layer doped with Sm around the higher-index phases (or simply dope the lower index phase) to filter the spontaneous emission, so the Er-doped regions potentially maintain the lasing / amplifying light.

IV.E. Conclusions

Through use of a modified stack-and-draw technique previously described in Chapter III, two all-solid actively doped TALOFs were developed. The first, a Yb-doped TALOF, possessed a core microstructure with the physical properties (pitch, phase diameter, fill ratio) close to the target values established early in this Dissertation. The limiting component was the low refractive index difference resulting from the cores remelting during stacking-and-redrawing, which led to more diffusion and dissolution of the silica cladding into the core, diluting the core composition. However, even with a low index difference, this fiber demonstrated strong localization in various regions across the facet of the core over lengths upwards of 1 m.

Losses in this fiber however were surprisingly high (dB/cm) and are not entirely well understood. Air bubbles are observed occasionally throughout the length of the fiber which could be a source of this high loss, however the recorded losses were high even in fiber lengths with no visible air bubbles. Such high background losses, when constructing the linear laser cavity, limited the overall lasing capabilities of this TALOF, and when pumped at 976 nm, only spontaneous emission was recorded. Interestingly, pumping at the absorption wavelength appears to result in delocalization. This was confirmed by pumping the Yb-doped TALOF with a tunable Ti:Sapphire laser and varying the wavelength across the absorption band. The pump wavelengths within the band demonstrated delocalization while those outside of the absorption band demonstrated strong localization. The spontaneous emission observed from being pumped within the absorption band, could be masking the localization. Further theoretical modeling is underway to understand this effect and determine the impact on lasing capabilities of these actively doped TALOFs.

This spontaneous emission, however, could be used to pump other modes within the TALOF for possible amplification. Therefore, the second TALOF developed was doped with erbium. Presently, the Er-doped TALOF only demonstrated localization over a few cm. It is believed the difference in localization strength from the Yb-doped to the Er-doped TALOF is less so due to the microstructure, and more a result of the active dopant and the pump wavelength. Trivalent erbium absorbs at the currently available pump wavelengths (532, 633, and 976 nm), and demonstrated delocalization over longer lengths. Further localization studies are necessary to determine the localization strength in this fiber. Even though initial attempts at the development of either a TALOF laser or amplifier were unsuccessful, significant strides were made for their eventual demonstration. This Chapter presents the first all-solid actively doped TALOFs, one doped with Yb and the other doped with Er. The fiber fabrication method described herein can be used to incorporate other rare earth dopants as well, not just Yb or Er. Once the loss mechanisms in these fibers are better understood, and the laser cavities optimized, material development becomes simply modifying the precursor composition. Additionally, the effects of TAL in the presence of spontaneous emission were first addressed and need to be considered for future TALOF laser and amplifier development. Further investigations are necessary to determine the overall impact; however, it appears that in the presence of spontaneous emission, TAL is lost.

IV. F. Appendix: Er-doped holey fibers

To increase the localization strength of the Er-doped TALOF for potentially more efficient multiplexing, an Er-doped silica-and-air disordered fiber was developed. The overall fabrication process follows suit with the previously described stack-and-draw technique, except instead of utilizing molten core derived optical fibers, the precursor core material comprised of hollow core Er-doped silica fibers of varying inner and outer diameters. These precursor fibers were developed using Modified Chemical Vapor Deposition (MCVD). Initially, silica soot was deposited on the inside of a silica substrate tube. The tube was then solution doped using a 1:1 weight ratio of $AlCl_3$ and $ErCl_3$ salts (2 grams of each) dissolved in 200 mL of water. Once dried, the tube was sintered and partially collapsed to have an Er-doped ring surrounding the hollow core. Figure IV.10 is a light microscope image of the resulting hollow-core fiber.

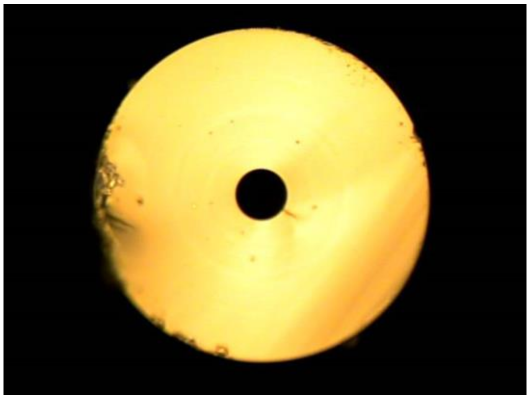

Figure IV. 10. Light microscope image of the hollow-core precursor fiber.

The refractive index profile (RIP) of the preform was measured to verify the presence of the doped ring. Figure IV.11 is the corresponding RIP. The two lines represent different locations along the preform taken 30 mm apart to estimate longitudinal homogeneity. The shoulders at ± 0.5 mm suggest the presence of the doped ring. The 0.0003 offset in the cladding ($\Delta n > 0$) is attributed to the differences in the refractive index of the cladding and the index matching gel. Finally, the noise in the middle of the RIP is due to the magnitude of the refractive index difference resulting from central region being hollow and is an artifact of the processing software.

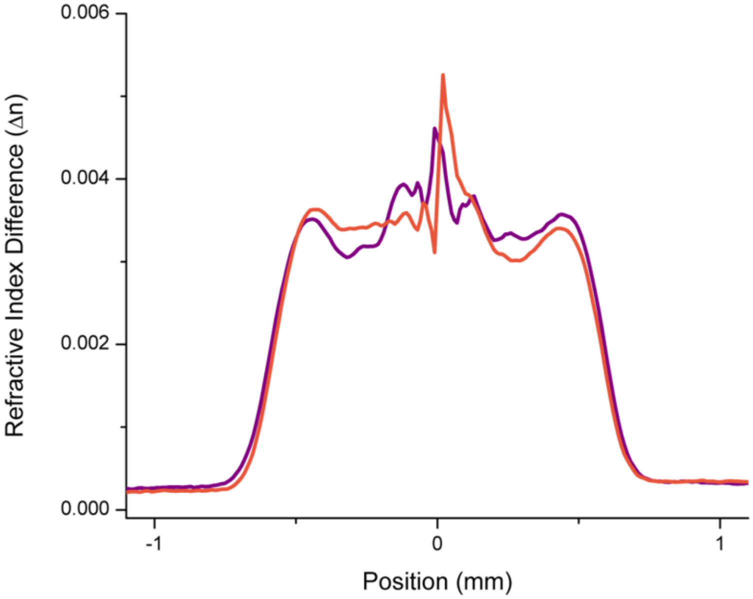

Figure IV.11. Refractive index profile of two locations taken 30 mm apart along the hollow-centered preform containing the erbium ring layer. The noise in the middle of the profile is an artefact of the processing software due to the large refractive index difference between silica and air.

Three identical hollow-core preforms were developed using this methodology and were drawn to hollow-core fiber possessing varying dimensions ranging from 35 to 45 µm inner and 200 to 300 µm outer diameters. These fibers were cut to 15 cm lengths and subsequently stacked in a 19x25 mm inner / outer diameter custom manufactured preform. Since the inner diameters of these hollow core fibers were much larger than the core sizes of the molten core derived fibers, the inner diameter of the preform needed to be much larger to obtain site sizes on the order of ~1 µm. The preform was drawn to a 1 mm outer diameter fiber at 1865°C. The lower draw temperature was to keep the hollow region of the fibers open during drawing. Figure IV.12.a is a representative electron micrograph of the facet and Figure IV.12.b is a light microscope image back illuminated to show the Er-sites (lighter spots dispersed throughout). As can be seen, the bright spots suggest the cores all collapsed during drawing. When drawing, the surface tension remained too high for the cores to open, though the interstitials between the different fibers began to open. Unfortunately, because of these new air-gaps, the mechanical strength of the core / fiber diminished. When this fiber was cleaved to investigate potential localization, the core would shatter. Smaller diameter fibers may yield more success. The use of an active ring layer in a hollow-cre precursor fiber could potentially be a useful method of introducing air into the disordered core to potentially increase the localization strength, however further fiber development is necessary. Techniques such as pressurinzing the prefurm during draw could result in more air-gaps.

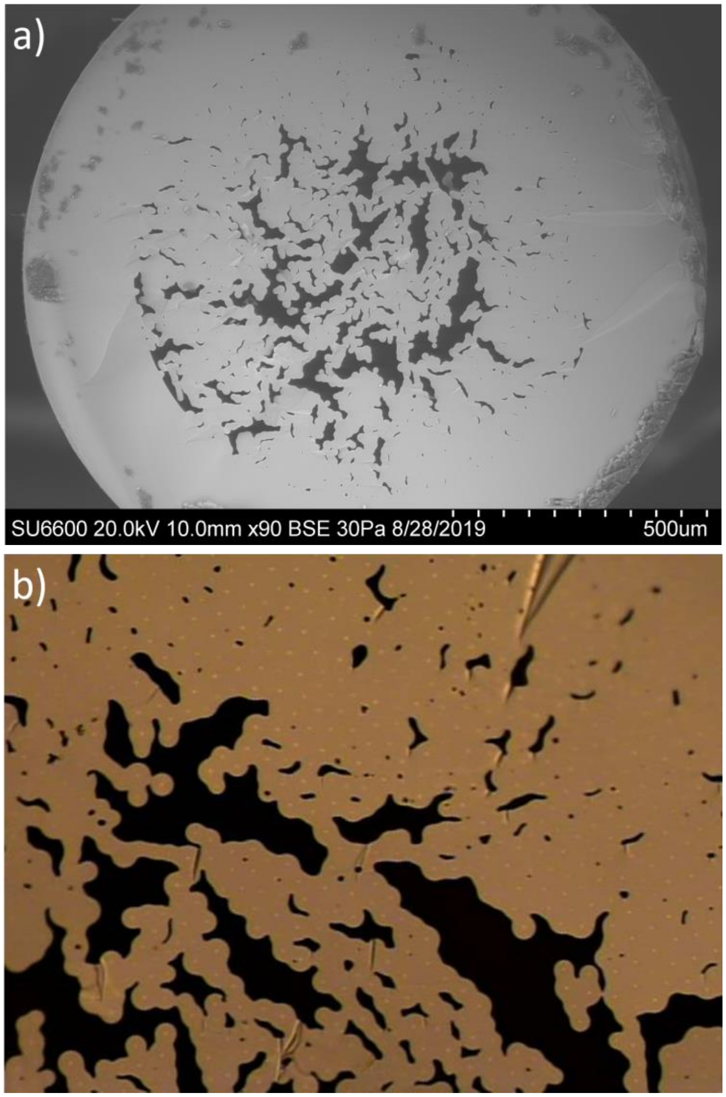

Figure IV.12. a) Representative electron micrograph of the resulting cross-section of the fiber derived from stacking-and-drawing the hollow core precursor fibers. Also shown is b) a light microscope image back-illuminated to show the collapsed Er-ring layer, appearing as lighter spots throughout.

IV. G. References

[1] S. Karbasi, T. Hawkins, J. Ballato, K. W. Koch, and A. Mafi, “Transverse Anderson localization in a disordered glass optical fiber,” *Optical Materials Express* **2**(11), 1496-1503 (2012).

[2] M. Chen, and M.-J. Li, “Observing transverse Anderson localization in random air line based fiber,” Proceedings Volume 8994, Photonics and Phononic properties of engineered nanostructures IV, 89941S, SPIE (2014).

[3] J. Zhao, J. E. Antonio-Lopez, R. A. Correa, A. Mafi, M. Windeck, and A. Schülzgen, “Image transport through silica-air random core optical fiber,” CLEO JTu5A.91 (2017).

[4] T. H. Tuan, S. Kuroyanagi, K. Nagasaka, T. Suzuki, and Y. Ohishi, “Characterization of an all-solid disordered tellurite glass optical fiber and its NIR optical image transport,” *Japanese Journal of Applied Physics* **58**(3), 032005 (2019).

[5] J. Zhao, J. E. Antonio-Lopez, Z. Zhu, D. Zheng, S. Pang, R. A. Correa, and A. Schülzgen, “Image transport through meter-long randomly disordered silica-air optical fiber,” *Scientific Reports* **8**, 3065 (2018).

[6] S. Karbasi, R. J. Frazier, K. W. Koch, T. Hawkins, J. Ballato, and A. Mafi, “Image transport through a disordered optical fibre mediated by transverse Anderson localization,” *Nature Communications* **5**, 3362 (2014).

[7] S. Karbasi, K. W. Koch, and A. Mafi, “Multiple-beam propagation in an Anderson localized optical fiber,” *Optics Express* **21**(1), 305-313 (2013).

[8] B. Abaie, E. Mobini, S. Karbasi, T. Hawkins, J. Ballato, and A. Mafi, “Random lasing in an Anderson localizing optical fiber,” *Light: Science and Applications* **6**, e17041 (2017).

[9] I. D. Miller, D. B. Mortimore, P. Urquhart, B. J. Ainslie, S. P. Craig, C. A. Millar, and D. B. Payne, “A Nd^{3+}-doped cw fiber laser using all-fiber reflectors,” *Applied Optics* **26**(11), 2197-2201 (1987).

[10] D. J. Richardson, J. Nilsson, and W. A. Clarkson, “High power fiber lasers: current status and future perspectives,” *Journal of the Optical Society of America B* **27**(11), B63-B92 (2010).

[11] M. N. Zervas and C. A. Codemard, “High power fiber lasers: a review,” IEEE *Journal of Selected Topics in Quantum Electronics* **20**(5), 0904123 (2014).

[12] P. D. Dragic, M. Cavillon, and J. Ballato, “Materials for optical fiber lasers: a review,” *Applied Physics Reviews* **5**, 041301 (2018).

[13] R. J. Mears, L. Reekie, I. M. Jauncey, D. N. Payne, “Low-noise erbium-doped fibre amplifier operating at 1.54 um,” *Electronics Letters* **23**(19), 1026-1028 (1987)

[14] R. I. Laming, M. N. Zervas, and D. N. Payne, “Erbium-doped fiber amplifier with 54 dB gain and 3.1 dB noise figure,” *IEEE Photonics Technology Letters* **4**(12), 1345-1347 (1992).

[15] B. J. Ainslie, “A review of the fabrication and properties of erbium-doped fibers for optical amplifiers,” *Journal of Lightwave Technology* **9**(2), 220-227 (1991).

[16] Y. Ohishi, T. Kanamori, T. Kitagawa, and S. Takahashi, “Pr^{3+}-doped fluoride giber amplifier operating at 1.31 um,” *Optics Letters* **16**(22), 1747-1749 (1991)

[17] A. Mori, Y. Ohishi, T. Kanamori, and S. Sudo, “Optical amplification with neodymium-doped chalcogenide glass fiber,” *Applied Physics Letters* **70**, 1230-1232 (1997).

[18] M. Cavillon, P. Dragic, B. Faugas, T. W. Hawkins, and J. Ballato, “Insights and Aspects to the modeling of the molten core method for optical fiber fabrication,” *Materials* **12**(18), 2898 (2019).

[19] S, Karbasi, C. R. Mirr, R. J. Frazier, P. G. Yarandi, K. W. Koch, and A. Mafi, “Detailed investigations of the impact of the fiber design parameters on the transverse Anderson localization of light in disordered optical fibers,” *Optics Express* **20**(17), 18692-18706 (2012).

[20] M. Cavillon, C. Kucera, T. W. Hawkins, N. Yu, P. Dragic, and J. Ballato, “Ytterbium-doped multicomponent fluorosilicate optical fibers with intrinsically low optical nonlinearities,” *Optical Materials Express* **8**(4), 744-760 (2018).

[21] M. Cavillon, C. Kucera, T. Hawkins, A. F. Runge, A. C. Peacock, P. Dragic, and J. Ballato, “Oxyfluoride core silica-based optical fiber with intrinsically low nonlinearities for high energy laser applications,” *Journal of Lightwave Technology* **36**(2), 284-291 (2018).

[22] M. Cavillon, J. Furtick, C. Kucera, C. Ryan, M. Tuggle, M. Jones, T. Hawkins, P. Dragic, and J. Ballato, “Brillouin properties of a novel strontium aluminosilicate glass optical fiber,” *Journal of Lightwave Technology* **34**(6), 1435-1441 (2016).

[23] W. Schirmacher, B. Abaie, A. Mafi, G. Ruocco, and M. Leonetti, "What is the right theory for Anderson localization of light? An experimental test," *Physical Review Letters* **120**, 067401 (2018).

[24] I. D. W. Samuel, E. B. Namdas, and G. A. Turnbull, "How to recognize lasing," *Nature Photonics* **3**, 546-549 (2009).

[25] M. Melo, J. Sousa, and M. Berendt, "Stimulated Raman scattering mitigation through amplified spontaneous emission simultaneous seeding on high power double-clad fiber pulse amplifiers," Proceedings of SPIE 7914, Fiber Lasers VIII: Technology, Systems, and Applications, 79142N (2011).

[26] W.-P. Qin, Z.-Y. Liu, C.-N. Sin, C.-F. Wu, G.-S. Qin, Z. Chen, and K.-Z. Zheng, "Multi-ion cooperative process in Yb^{3+} clusters," *Light: Science and Applications* **3**, e193 (2014).

[27] B. Gökbulut, and M. N. Inci, "Investigation of spontaneous emission dynamics of dye molecules coupled into transverse Anderson localized cavities in a hyperbolic waveguide," *Photonics and Nanostructures – Fundamentals and Applications* **39**, 100769 (2020).

[28] M. Digonnet, *Rare-earth-doped fiber lasers and amplifiers 2nd ed.* (Marcel Dekker, Inc., 1993, New York, NY) Chapter 2.

[29] C. J. Koester, E. O. Dixon, and E. Snitzer, Laser systems and the like employing solid laser components and light absorbing claddings, US Patent #3,445,785 (May 1969).

[30] S. Kim, U.-C. Ryu, and K. Oh, "41-nm 3-dB gain-band optical amplifier using an Er-doped core and Sm-doped inner-cladding fiber without external filters," *IEEE Photonics Technology Letters* **12**(8), 986-988 (2000).

[31] U.-C. Ryu, S. Kim, and K. Oh, "Gain controlling or erbium-doped fiber amplifier by samarium doped inner-cladding in the 1.5μm region," *Fiber and Integrated Optics* **20**(5), 471-477 (2001)

[32] K. Oh, S. Yoo, U.-C. Ryu, S. Kim, U.-C. Paek, D. B. S. Soh, J. K. Sahu, and J. Nilsson, "Spectral control of optical gain in a rare earth-doped optical fiber using novel triple layered structures," *Optical Fiber Technology* **12**, 297-304 (2006).

CHAPTER FIVE

NONLINEARITIES IN TRANSVERSE ANDERSON LOCALIZING OPTICAL FIBERS

V. A. Introduction

One area where rich opportunities exist for TALOFs of different compositions and where no results have yet been reported, is in nonlinear fiber optics. TALOFs offer interesting possibilities for nonlinear optics because their localization can yield very small values to the effective area (A_{eff}) for a localized mode and, therefore, potentially result in the observation of nonlinearities at low threshold intensities. However, due to the low nonlinearity of silica [1], coupled with the relatively large A_{eff} (effectively the localized beam radius squared multiplied by π) nonlinearities have yet to be observed from the TALOFs reported to date [2-6]. The question of the influence of optical nonlinearities on Anderson localization has been a topic of debate for some time [7,8]. The underlying question regarding this debate is whether the presence of nonlinearity enhances or destroys Anderson localization. Unfortunately, due to the limited experimental observations of Anderson localization in material systems, much of this work is currently theoretical [7,9].

V. B. Development of fibers investigated

The TALOF discussed here was drawn using the stack-and-draw technique specifically adapted for utilizing molten core derived precursor fibers [10] in the stack.

This method is thoroughly discussed in Chapter III. The fibers used throughout these experiments are the same as those originally designed for developing a TALOF laser (Chapter IV). For completeness, the stack-and-draw process and precursor fibers will be described here. The precursor optical fibers, i.e., optical fibers later stacked and re-drawn, were drawn from a well-studied powder composition (8:5 molar ratio of Al_2O_3 – SrO [11]), lightly doped with Yb_2O_3. The core powder was prepared by weighing and mixing commercial SrO (99.5% purity, Alfa Aesar), Yb_2O_3 (99.999% purity, Alfa Aesar) and Al_2O_3 (99.995% purity, Alfa Aesar) powders. The powders were ball-milled to ensure homogeneous mixing, and then loaded into a silica preform to be drawn to fiber. The capillary silica preform (3 mm inner / 30 mm outer diameter) was drawn to 125 μm outer diameter fiber. This fiber composition (denoted Yb:SrAlSiO) was chosen because its properties are well-known and include a relatively high refractive index difference with respect to the silica cladding of the fiber [11,12]. Bare fibers were etched in hydrofluoric (HF) acid for various times to achieve different outer diameters that facilitated a random arrangement upon stacking as well as to achieve a higher fill ratio of high index inclusions (the Yb:SrAlSiO glass) in the silica. Roughly 2000 of these etched fibers then were stacked inside a 7.8 mm inner / 30 mm outer diameter telecommunications grade silica capillary preform and re-drawn at 1925°C to the final fiber with an outer diameter of ~900 μm. This fiber possessed a disordered core of approximately a 150 μm diameter.

Compositional analysis was conducted using Energy Dispersive X-ray Spectroscopy (EDX) on a Hitachi NB5000 dual-beam Focused Ion Beam (FIB) and Scanning / Transmission Electron Microscope (STEM). Conventional EDX on bulk optical fibers generally results in the electron beam probing a larger volume than just one of the TALOF phases, resulting in a skewed composition. Therefore, a 50 μm^2 region of the sample containing both the higher and lower index phases was lifted out using the FIB and subsequently ion polished to a thickness of less than 100 nm to minimize the beam probe diameter, obtaining a more accurate composition. Refractive indices (n) were calculated using the measured composition and a form of the Winkelmann-Schott model [13]. Physical parameters (such as site size, Φ, and pitch, Λ) of the disordered fiber were determined using ImageJ and high-resolution images of the facet.

V. C. Nonlinear optics within TALOFs

Nonlinear experiments were conducted by free-space coupling a frequency doubled Q-switched Nd:YAG laser (532 nm, 680 ps, high peak power) into various Anderson localized modes and increasing the laser intensity. The fibers were cooled using a fan during the experiments to minimize surface damages induced by the high light intensity. The output spectra were measured by free-space coupling the output mode into an optical fiber-based detector connected to a CCS200 compact spectrometer (Thorlabs) with an operation wavelength of 200 – 1000 nm and a spectral resolution of < 2 nm. The intensity of the pump emission was reduced using neutral density filters. All fibers used for these experiments were kept straight to minimize bend-induced losses. Figure V.1.a is a representative image of the nonlinear measurement setup, along with Figure V.1.b providing a visual example of an Anderson localized mode excited in the

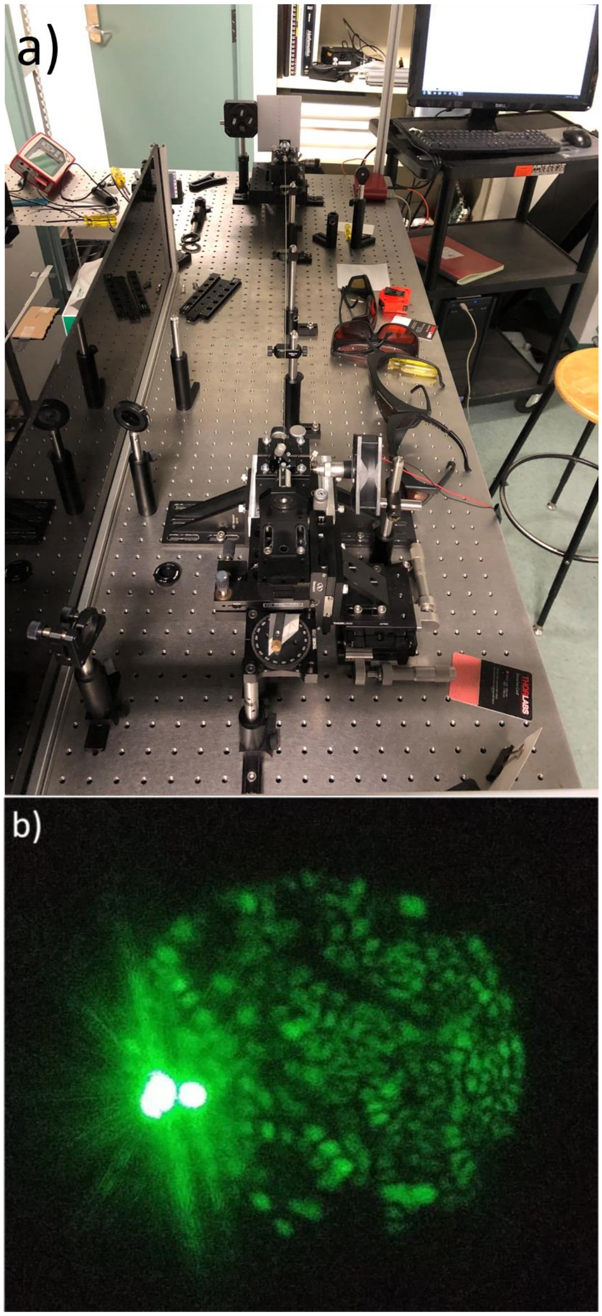

Figure V.1. a) Experimental setup for the nonlinear measurements. Not shown in the image is the frequency doubled Nd:YAG laser source. b) is the output image from the facet of the fiber imaged using a camera. The high intensity spots portray a localized mode.

TALOF. Figure V.1.b is merely an example of the localized mode to provide a visual example for the reader. Not all localized modes will have the same appearance [7]. From the image, the localized mode in this example extends to two of the higher index nodes. The entire core is illuminated, suggesting some of the light is leaking from the localized mode. This could potentially provide insight into the sources of loss discussed in Chapter IV.

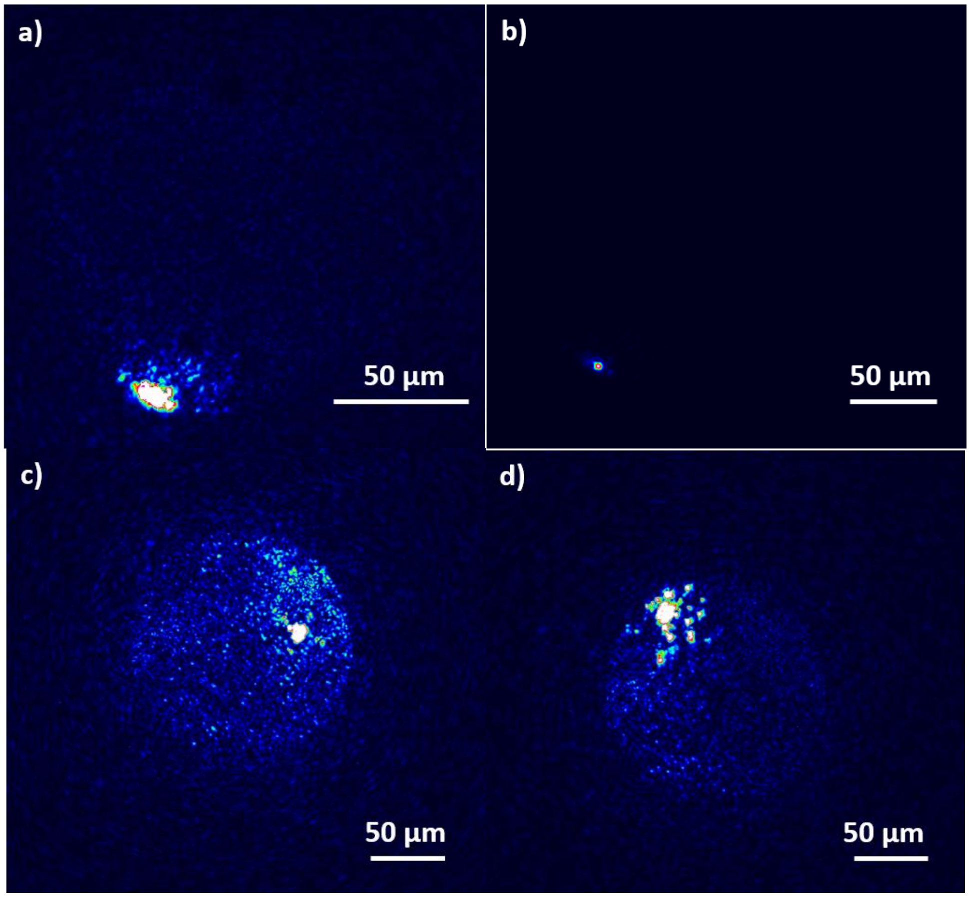

Figure V.2. Output from the TALOF of various localized modes along a (a) 80 cm long sample with a (b) low exposure picture of the same mode. (c) and (d) are of the localized modes in a 70 cm long piece excited for nonlinear experiments.

Figure V.2 provides images of the output facet of the all-solid silicate TALOF recorded with a CCD of various localized modes excited. Figure V.2.a shows the output over an 81 cm long sample and Figure V.2.b is of the same mode with a lower exposure time to minimize saturation in the intensity profile. The high exposure is merely to portray the location of the localized mode within the facet of the fiber. Occasionally, longitudinal inhomogeneities, such as air-bubbles, were observed along the length of the fiber, an inherent problem with the stack-and-draw process, resulting in scattering and loss that often masked the localization. Also, since minor longitudinal perturbations are detrimental to nonlinear phase matching [14,15], the fiber was cut back until nonlinear four-wave mixing (FWM) frequency shifts were observed. Figures V.2.c and V.2.d are CCD images of representative localized modes in the 70 cm long piece utilized for the nonlinear experiments.

Figure V. 3 is an intensity plot extracted from the CCD images of Figure V.2.b with the 0 position being the center of the peak. The shoulder around -4 μm suggests some coupling to a neighboring mode. The shape of the mode profile is similar to those reported in Refs. 3 and 16 for transverse Anderson localized (TAL) modes. The characteristic exponentially decaying "tails" can be observed at either end. Based on the modal profile, the mode A_{eff} is approximately 39.37 μm^2 (calculated using the intensity measured with the CCD at a wavelength of 632.8 nm). This corresponds to a mode field diameter (MFD) of approximately 7.08 μm, nearly quadruple the physical diameter of the higher-index phases. Assuming a Gaussian profile, the MFD was calculated using the

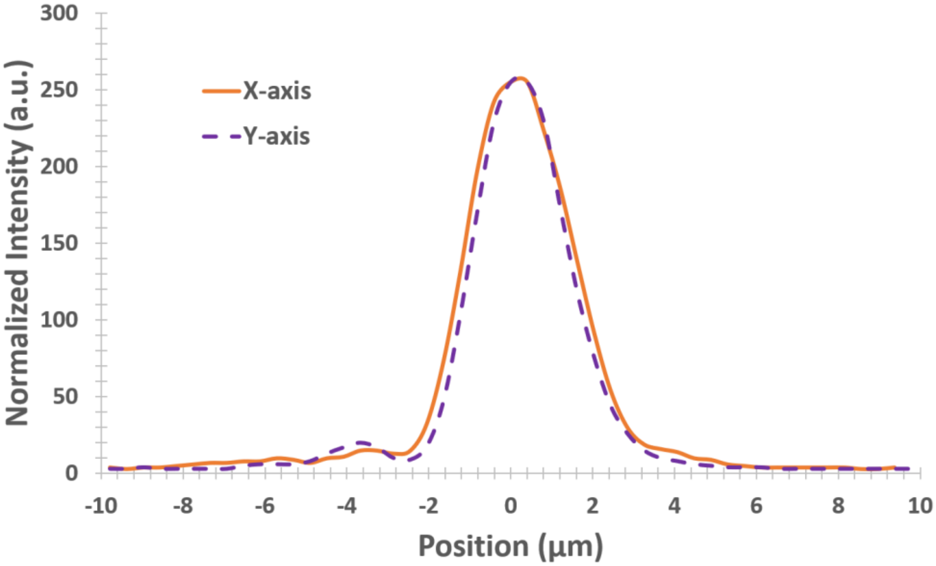

Figure V. 3. Intensity plot of the localized beam profile in the x- and y-directions of Figure V.2.b showing the exponentially decaying tails, characteristic of transverse Anderson localization.

equation: $MFD = \frac{2}{\sqrt{\pi}}\sqrt{A_{eff}}$ [17]. Intuitively, this makes sense as the localized mode extends beyond a single higher-index node. For a comparison, the A_{eff} of a commercial Thorlabs 630HP optical fiber containing a physical core diameter of 3.5 µm is ~12.6 µm^2 [18] (calculated from MFD). It must be noted that every localized mode in the facet of the fiber will contain a different A_{eff} due to the randomness of the microstructure [7]. The one reported here is merely to provide an example of the potential A_{eff} in these localized modes, which in this case, proves beneficial for optical nonlinearities.

An 83 cm long piece of DC 4 was first investigated for optical nonlinearities. Both ends of the fiber were cleaved using a Vytran (Thorlabs) automated cleaver designed for larger diameter fibers to ensure a pristine facet. The laser was coupled into a localized mode using one of the objectives and the output recorded on the CCD. Then, the CCD was moved, and the output spectra analyzed recorded. The output intensity of the fiber was controlled using neutral density filters to attenuate the light intensity, and a notch filter designed to absorb/reflect the pump wavelength. The intensity of the laser was increased, and different output spectra recorded.

The output spectra obtained from a mode in the 83 cm long sample are provided in Figure V.4 with each peak labeled in the spectral shift in wavenumber (calculated as $10^7/\lambda$, with λ being the wavelength in nm) from the emission peak. Also provided is a CCD image of the localized mode excited for these experiments with a high exposure time to image more of the fiber (b), and low exposure time to focus on the localized mode (c). The peak emission wavelength for the 532 nm laser source was measured using the spectrometer to be 531.47 nm, therefore this value will be used for all subsequent calculations. The deviation from 532 nm is due to the spectrum analyzer not being properly calibrated, however the shift is assumed to affect all recorded peaks. Each plot is effectively “tuned” to suppress different peaks by rotating the notch filter or attenuating the beam using neutral density filters. Three separate spectra are overlaid on the plot and all were recorded from the same localized mode. The emission laser line is plotted in blue as a reference point and is centered at the 0 cm^{-1}. The orange and purple spectra were “tuned” to emphasize different observed peaks. The input conditions were equivalent between the two frequency-shifted spectra.

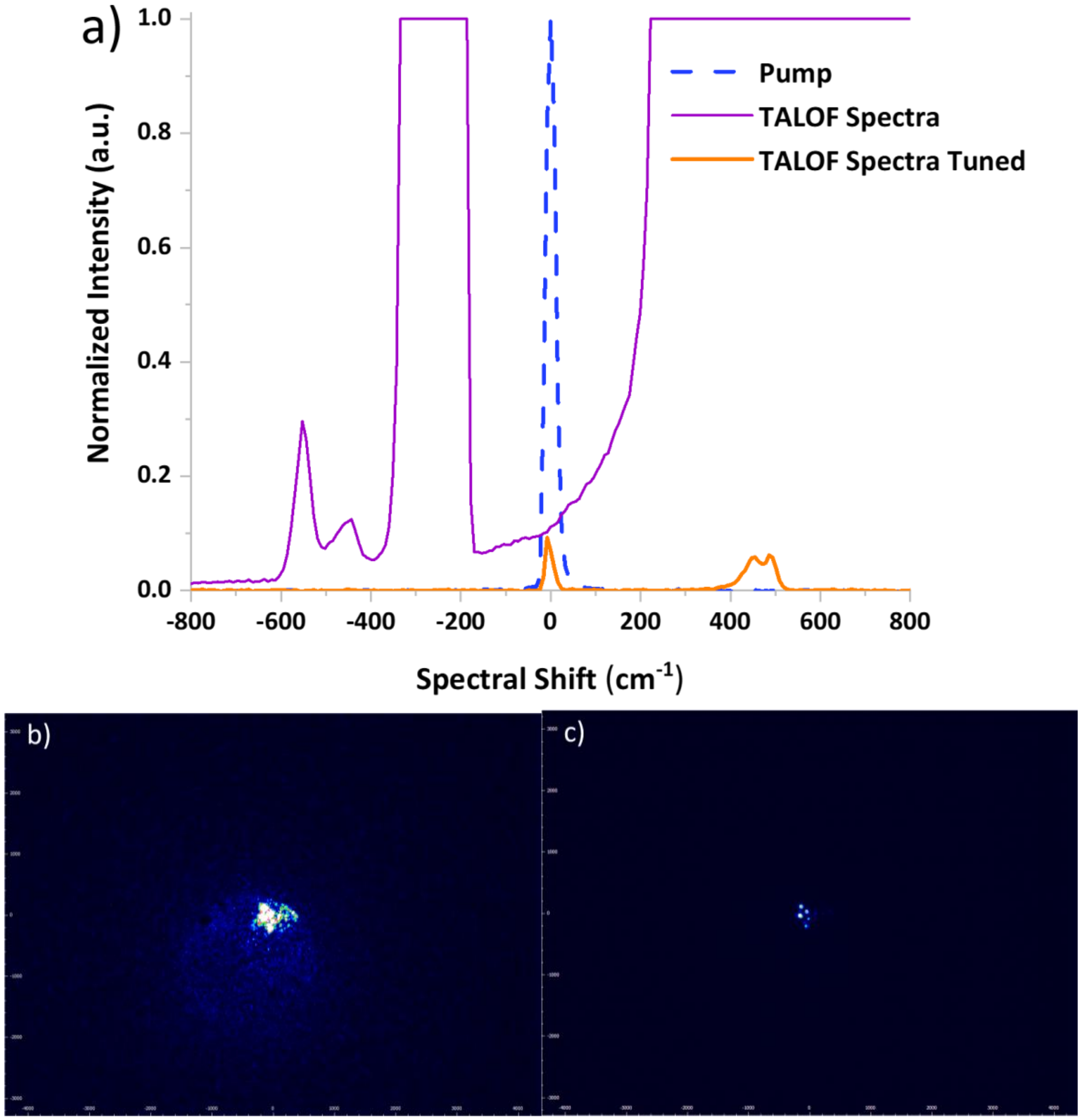

Figure V.4. a) Emission spectra through an 83 cm long sample of DC4 pumped with 532 nm through a localized mode. The localized mode was imaged using a CCD with a b) high exposure time to image the entire facet of the core and c) low exposure to emphasize the localized mode. The units on the axes of b and c are arbitrary.

Several frequency shifts were observed, spanning -600 to 600 cm^{-1} shifted from the laser emission (between 515 to 545 nm). The negative shifts are blueshifted frequencies and the positive shifts are redshifted frequencies. It is believed the peaks observed at 455 and 485 cm^{-1} (544.65 and 545.56 nm respectively) are the Raman Stokes shift in high silica containing fibers [19,20]. The peak at -443 cm^{-1} (519.25 nm) from the laser emission line is believed to be the Raman anti-Stokes shift. An additional peak is observed near the perceived Raman anti-Stokes shift at -552.63 cm^{-1} (516.31 nm), along with a saturated peak spanning from -170 to 400 cm^{-1}. Since the saturated peak is unresolvable, it will be ignored for the present discussion. It is possible the peak at -552 cm^{-1} could be FWM, although the red-shifted counterpart is unable to be observed due to the strong Raman intensity saturating the detector. Further investigations are necessary to confirm the origin of these peaks.

Figure V.5 provides the output spectrum measured when an Anderson localized mode in a 70 cm long piece of the TALOF was pumped with the 532 nm pulsed laser source (blue dashed line). The abscissa again is reported in wavenumber to represent the frequency shifts away from the pump wavelength (the 0 cm^{-1} point). The spectrum is separated in two colors (orange-solid and purple-dashed line) to aid the reader in differentiating the two nonlinear phenomena being discussed. These peaks were observed simultaneously. As previously discussed, the doublet peaks observed at approximately 440 and 485 cm^{-1} (purple dashed line) are characteristic of the Raman shift in fused silica [19]. These correspond to the Si-O-Si stretching modes and the defect lines respectively. If the pump power is increased beyond a certain threshold, sequential Raman peaks can be observed at further iterations of ~440 cm^{-1}. While only one Raman shift was demonstrated in this Chapter, further studies are underway to investigate the possibility of extending the Raman peaks in these TALOFs [21].

Two additional peaks were observed at frequency shifts of +331 cm^{-1} and -334 cm^{-1} (orange solid line) relative to the pump laser line. These shifts correspond to mixed-mode FWM in high silica-content fibers [14,22]. The slight difference in peak position (~3 cm^{-1}) is attributed to the resolution of the spectrometer. The FWM intensity is expected to be an order of magnitude stronger than the Raman intensity [14], which was not the case here. Minor perturbations along the length of the TALOF (such as air

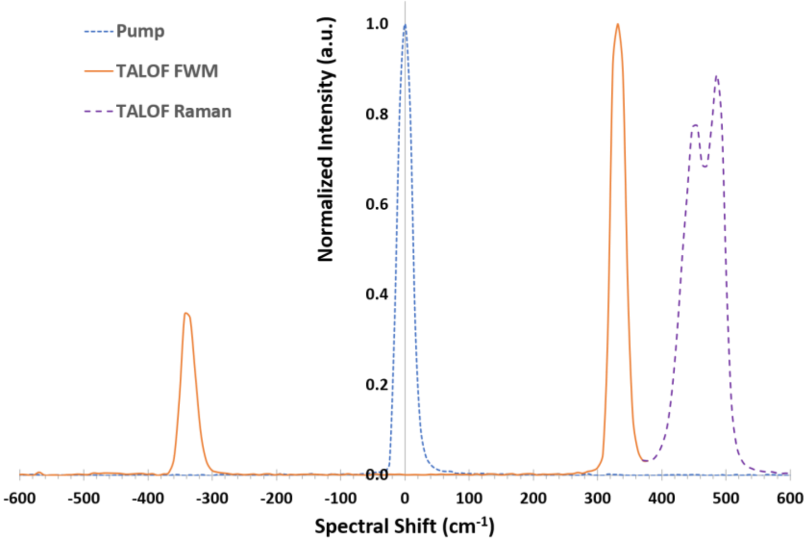

Figure V. 5. Output spectra from an Anderson localized mode pumped at 532 nm (blue-dashed line). Shown is the Raman shift at ~440 cm^{-1} (purple-dashed line), and four-wave mixing both blue and redshifted equidistant at ~330 cm^{-1} (orange solid line).

bubbles) likely reduce the FWM intensity [15]. Shorter lengths of fiber could be used, minimizing longitudinal distortions. Additionally, it is expected the red and blue-shifted frequencies will have nearly the same intensities [14]. Obviously, this also was not the case. At frequency shifts less than 1000 cm^{-1} from the pump, the FWM intensity of the Stokes shift (redshift) is expected to be higher than the resulting anti-Stokes shift (blueshift) [23]. This has been observed in silica optical fibers previously [14, 22].

Several additional peaks were observed in this mode with increased pump intensity. Each peak is labeled on in Figure V.6. Interestingly, peaks a and g are blue- and

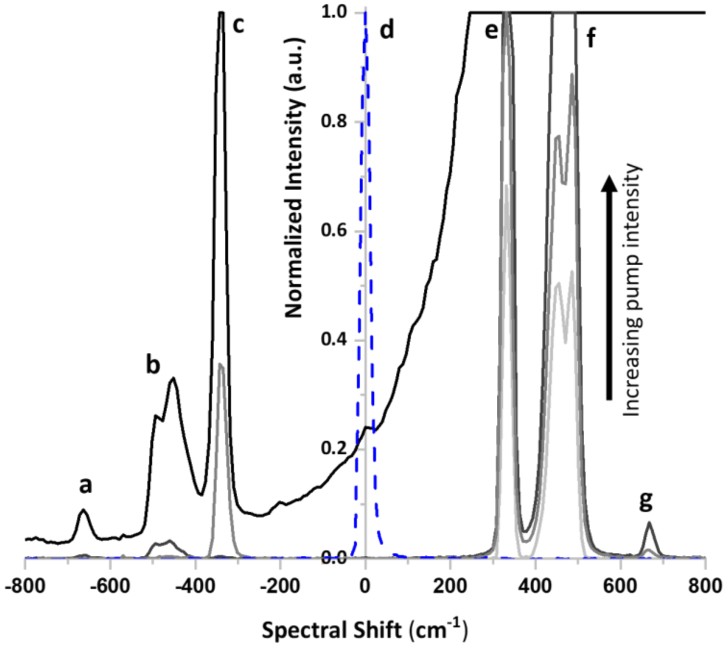

Figure V.6. Plot representing the spectral shifts observed from the Anderson localized mode of a 70 cm long TALOF when varying the intensity of the pulsed laser source. The blue dashed line represents the pump and the gray-scale lines are the resulting spectra. All peaks are labeled in the plot and described in the text.

redshifted equidistant ~660 cm^{-1}. It is possible these peaks may be additional FWM, however, the g peak is oftentimes masked by the strong intensity of the Raman shift (peak f), as shown with the solid black line saturating from ~200 cm^{-1} to beyond the edge of the spectrum. It would be possible to investigate this further to validate the additional FWM if the Raman shifted wavelengths could effectively be filtered out. Peaks b and f are the anti-stokes and stokes Raman shift associated with the molecular vibrations of the silica glass (± 440 cm^{-1}). Peaks c and e are the FWM described above, and peak d is the pump. Further efforts are necessary to effectively filter the Raman emission to study the additional peaks observed through Figures V.4 and V.6.

V. C. 1. Laser-induced damage to the fiber facet

Occasionally, during experiments at high laser peak power, the input fiber end-face would damage over time. Fortunately, the damage only extended a few micrometers within the fiber. If all localized regions of the fiber were damaged or destroyed, a few centimeters of the fiber could be cleaved to remove the damaged portion and tests could resume. Interestingly, weakly localized modes tended to exhibit a lower damage threshold than the strongly localized modes. This is somewhat counter-intuitive in that a weakly localized mode tends to have a larger A_{eff}, meaning a lower power density (intensity per effective mode area). If the damage threshold is the result of a material limitation, it would be expected the damage would occur more frequently at a higher power density. It is presently unclear specifically the cause of the seemingly anomalous damage threshold.

Figure V.7.a-c are electron micrographs of three different fiber facets with the resulting laser damage. The grooves in Figures V.7.a-b are a result of moving the high intensity laser after the initial damage has occurred. Figure V.7.c shows the laser damage in three distinct modes. It is also interesting to note that the laser damage would only occur when the laser was coupled into a localized mode. Figure V.7.d is a light microscope image of the depth of the damage. Air bubbles are also observed along the length of the fiber near the facet, which could be a potential cause for the damage.

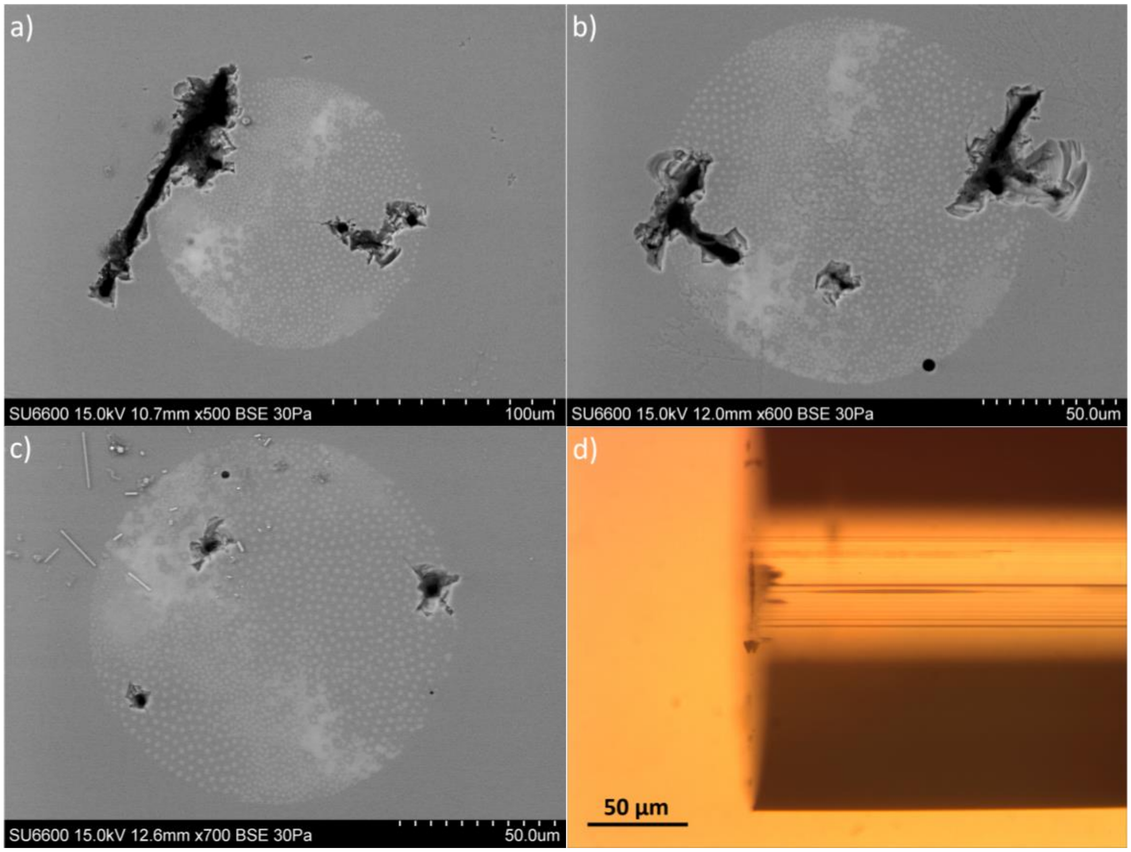

Figure V. 7. (a-c) Various electron micrographs of laser damage in the facet of DC4. Figure d is a light microscope image depicting the depth of laser damage.

V. D. Conclusions

In conclusion, a new modified stack-and-draw method of TALOF fiber fabrication was developed and employed that incorporates molten core derived optical fibers for developing novel all-solid, silicate TALOFs. Even though the resulting Δn was low, the transversely disordered optical fiber demonstrated strong TAL in various regions across the fiber cross-section. To the best of the authors' knowledge, this is the first report of an all-solid silicate TALOF. Further, the fabrication approach permitted small localized mode areas of about 39.37 μm^2. The resultingly small A_{eff} permitted the observation of optical nonlinearities in a TALOF, specifically Raman and FWM, also a first to our knowledge. This method of fiber fabrication could be utilized to incorporate a very wide variety of fiber core compositions possessing higher nonlinearities for the further development of nonlinear TALOFs. Longitudinal inhomogeneities are likely impacting the FWM. Shorter lengths of fiber could be used to suppress Raman scattering, while enhancing FWM due to minimizing longitudinal inhomogeneities along the length of the fiber.

As to the interplay between optical nonlinearities and TAL, the results of this Chapter at the very least support the conclusion that the presence of nonlinearities does not necessarily destroy TAL. The nonlinearity resulting from strongly localized modes is enough to generate FWM, and localization is maintained. Whether this localization is enhanced or weakened in the presence of nonlinearities is not conclusive. This work is not meant to be decisive as to the underlying nature of Anderson localization in the presence of nonlinearities, however, can begin providing experimental insight into these fundamental questions.

V. E. Appendix: Additional optical frequency shifts

Several additional peaks were observed during these experiments in the same mode of the 70 cm long TALOF described above, however oftentimes the Raman peak was saturating the detector. Figure V.8 is a plot depicting the spectral shifts (grey solid line) when the TALOF was pumped with the 532 nm pulsed laser source (blue dashed line). Peaks a and d are spaced equidistant at -663 and 667 cm^{-1} respectively as described previously. These could be attributed to additional FWM shifts in the fiber. Unfortunately, the peak intensity is kept low to not become masked by the strong Raman intensity (as shown by the broad saturation in Figure V.6). These peaks could be studied further if the Raman intensity is effectively filtered out. There is a smaller blueshifted peak (b) observed at -493 cm^{-1}. This could be the anti-stokes of Raman, although the shift is expected to occur closer to -440 cm^{-1}. The mismatch could be attributed to the low resolution of the spectrometer or could be a secondary FWM frequency shift with the redshifted counterpart occurring near the Raman frequency shift. (e.g. the second peak in the Raman at 485 cm^{-1}, Figure V.5). These additional peaks warrant further studies regarding the possible interplays between FWM and Raman nonlinear frequency shifts.

If the intensity of the input laser is increased further, additional peaks become apparent. The same blueshifted peaks (-663, -451, and -338 cm^{-1}) as described previously in this Chapter are observed. A slight peak at -775 cm^{-1} is also observed, though at a

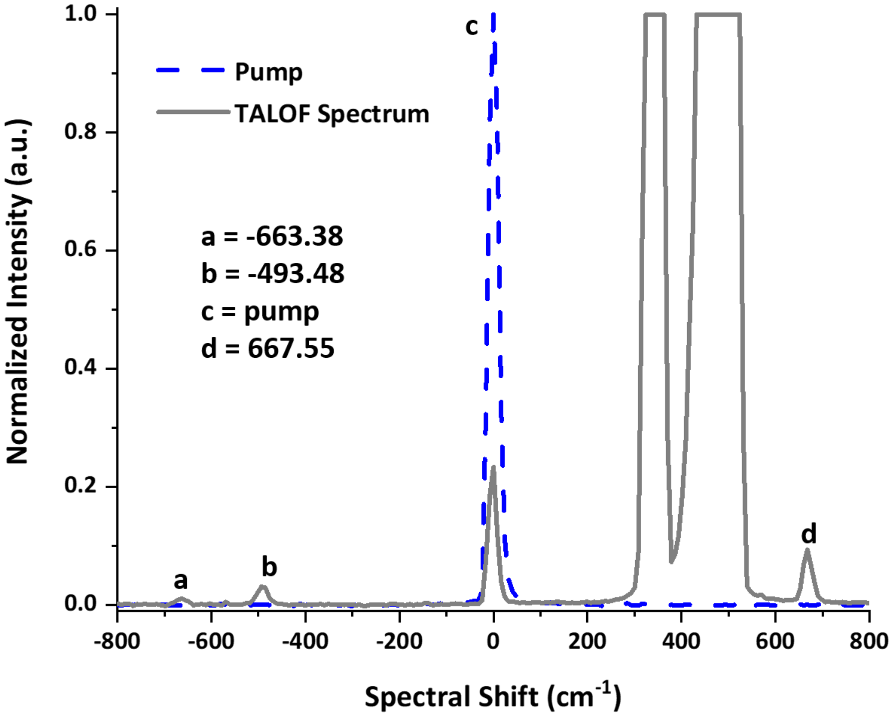

Figure V. 8. Spectral shifts observed from the Anderson localized mode of a 70 cm long TALOF when varying the intensity of the pulsed laser source. The blue dashed line represents the pump and the gray-solid line represents the spectrum. All peaks are labeled in the plot and described in the text.

significantly low peak intensity. It is possible this may be FWM, though the red-shifted counterpart is masked by the Raman shift. Due to the low peak intensity, it could also be noise amplified by the saturation. Three redshifted peaks also occur at 3141.95, 3215.81, and 3455.54 cm^{-1} (638.01, 641.03, and 651.04 nm). The suggested cause of these peaks is a rare earth impurity (such as trivalent erbium) resulting from contaminants in the industrial-grade precursors. Erbium-doped fibers have been pumped at 532 nm; however, the near-IR emission was the transition of interest for potential amplification in the telecommunications band [24]. Pumping trivalent erbium at 532 nm excites an electron from the ground state ($^4I_{15/2}$) to the excited state ($^2H_{11/2}$) [24]. Therefore, a possible route for relaxation could be non-radiative emission from $^2H_{11/2}$ to $^4F_{9/2}$ and subsequent radiative emission from $^4F_{9/2}$ to $^4I_{15/2}$ resulting in the generation of a photon around 650 nm [25]. This emission has been observed previously in Er/Yb co-doped nanoparticles [26]. This said, other trivalent lanthanide ions can also be pumped at

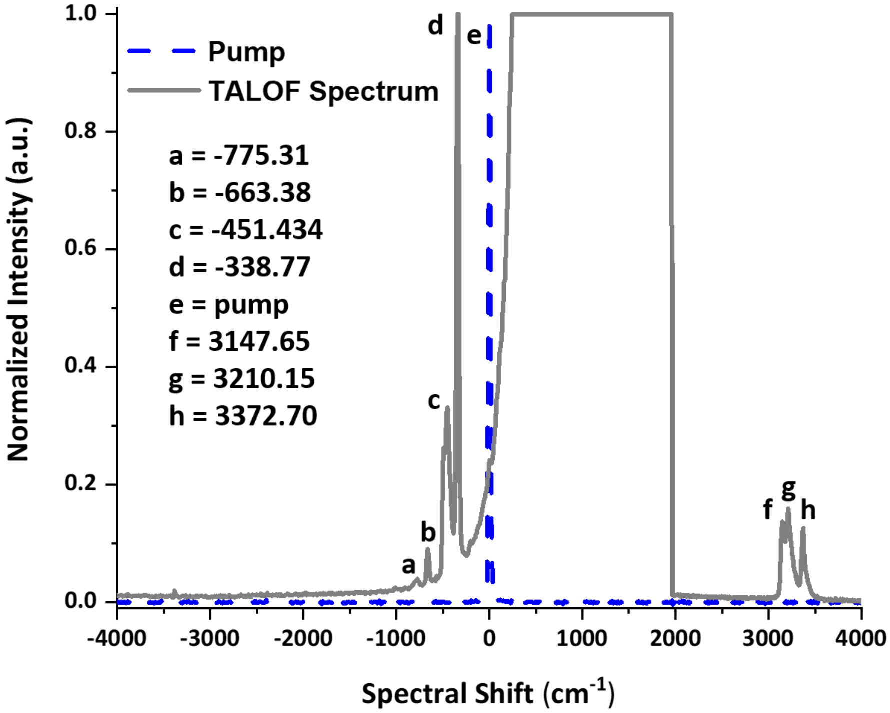

Figure V.9. Spectral shifts observed from the Anderson localized mode of a 70 cm long TALOF at higher pump intensity compared to Figure V.9. The blue dashed line represents the pump and the gray-solid line represents the spectrum. All peaks are labeled in the plot and described in the text.

532 nm [27], such as neodymium (Nd), samarium (Sm), europium (Eu), and holmium (Ho) that may have emissions near 650 nm. Further studies are necessary to confirm the origin of the three peaks.

V. F. References

[1] D. Milam, "Review and assessment of measured values of the nonlinear refractive-index coefficient of fused silica," *Applied Optics* **37**, 546-550 (1998).

[2] S. Karbasi, C. R. Mirr, P. G. Yarandi, R. J. Frazier, K. W. Koch, and A. Mafi, "Observation of transverse Anderson localization in an optical fiber," *Optics Letters* **37**, 2304–2306 (2012).

[3] S. Karbasi, T. Hawkins, J. Ballato, K. W. Koch, and A. Mafi, "Transverse Anderson localization in a disordered glass optical fiber," *Optical Materials Express* **2**, 1496–1503 (2012).

[4] M. Chen and M.-J. Li, "Observing transverse Anderson localization in random air line based fiber," Proceedings Volume 8994, Photonic and Photonic Properties of Engineered Nanostructures IV; 89941S (2014).

[5] J. Zhao, J. E. A. Lopez, Z. Zhu, D. Zheng, S. Pang, R. A. Correa, and A. Schülzgen, "Image transport through meter-long randomly disordered silica-air optical fiber," *Scientific Reports* **8**, 3065 (2018).

[6] T. Tuan, S. Kuroyanagi, K. Nagasaka, T. Suzuki, and Y. Ohishi, "Characterization of an all-solid disordered tellurite glass optical fiber and its NIR optical image transport," *Japanese Journal of Applied Physics* **58**, 032005 (2019).

[7] A. Mafi, “Transverse Anderson localization of light: a tutorial,” *Advances in Optics and Photonics* **7**(3), 459, (2015).

[8] A. Mafi, A brief overview of the interplay between nonlinearity and transverse Anderson localization,” preprint arXiv:1703.04011

[9] M. K. Nezhad, D. Mirshamsi, F. A. Zarif, H. R. M. Rezaelun, “Effect of loss on transverse localization of light in 1D optical waveguide array in the presence of Kerr-type nonlinearity,” *Optical and Quantum Electronics* **52**(4), (2020).

[10] J. Ballato, and A. Peacock, “Perspective: Molten Core optical fiber fabrication – A Route to new materials and applications,” *APL Photonics* **3**, 120903 (2018)

[11] M. Cavillon, J. Furtick, C. Kucera, C. Ryan, M. Tuggle, M. Jones, T. W. Hawkins, P. Dragic, and J. Ballato, “Brillouin properties of a novel strontium aluminosilicate glass optical fiber,” *Journal of Lightwave Technology* **34**(6), 1435-1441 (2016).

[12] M. Cavillon, C. Kucera, T. W. Hawkins, N. Yu, P. Dragic, and J. Ballato, “Ytterbium-doped multicomponent fluorosilicate optical fibers with intrinsically low optical nonlinearities,” *Optical Materials Express* **8**(4), 744-760 (2018).

[13] P. Dragic, M. Cavillon, A. Ballato, and J. Ballato, “A Unified materials approach to mitigating optical nonlinearities in optical fiber. II. Material additivity models and basic glass properties,” *International Journal of Applied Glass Science* **9**, 278-287 (2018).

[14] R. Stolen, “Phase-matched-stimulated four-photon mixing in silica-fiber waveguides,” *IEEE Journal of Quantum Electronics* **QE-11**, 100 (1975).

[15] R. Stolen, and J. Bjorkholm, “Parametric amplification and frequency conversion in optical fibers,” *IEEE Journal of Quantum Electronics* **QE-18**(7), 1062 (1982).

[16] T. Schwartz, G. Bartal, S. Fishman, and M. Segev, “Transport and Anderson localization in disordered two-dimensional photonic lattices,” *Nature* **446**, 52–55 (2007)

[17] Y. Namihira, “Relationship between nonlinear effective area and modefield diameter for dispersion shifted fibers,” *Electronic Letters* **30**(3), 262-264 (1994).

[18] https://www.thorlabs.com/thorproduct.cfm?partnumber=630HP

[19] R. Stolen, and F. Ippen, “Raman gain in glass optical waveguides,” *Applied Physics Letters* **22**, 276-278 (1973).

[20] G. Agrawal, *Nonlinear fiber optics 2nd edition,* (San Diego, CA: Academic Press, Inc. 1995).

[21] H. Pourbeyram, G. P. Agrawal, and A. Mafi, “Stimulated Raman scattering cascade spanning the wavelength range of 523 to 1750 nm using a graded-index multimode optical fiber,” *Applied Physics Letters* **102**(20), 201107 (2013).

[22] H. Pourbeyram, E. Nazemosadat, and A. Mafi, “Detailed investigation of intermodal four-wave mixing in SMF-28: blue-red generation from green,” *Optics Express* **23**(11), 14488 (2015).

[23] N. Bloembergen and Y. R. Shen, “Coupling between vibrations and light waves in Raman laser media,” *Physical Review Letters* **12**, 504 (1964).

[24] M. C. Farries, P. R. Morkel, R. I Laming, T. A. Birks, D. N. Payne, and E. J. Tarbox, “Operation of Erbium-doped fiber amplifiers and lasers pumped with frequency-doubled Nd:YAG lasers,” *Journal of Lightwave Technology* **7**(10), 1473-1477 (1989).

[25] M. J. F. Digonnet, *Rare-earth-doped fiber lasers and amplifiers 2nd edition*, Chapter 2, pages 61-90, (New York, NY: Marcel Dekker, Inc., 1993).

[26] A. Nadort, J. Zhao, and E. M. Goldys, “Lanthanide upconversion luminescence at the nanoscale: fundamentals and optical properties,” *Nanoscale* **8**(27), 13083-13524 (2016).

[27] G. H. Dieke, and H. M. Crosswhite, “The spectra of the doubly and triply ionized rare earths,” *Applied Optics* **2**(7), 675-686 (1963).

CHAPTER SIX

CONCLUSIONS, PRESENT CHALLENGES, AND FUTURE PERSPECTIVES IN THE DEVELOPMENT OF TRANSVERSE ANDERSON LOCALIZING OPTICAL FIBERS

VI. A. Summary of research and contributions to the state of knowledge

This Dissertation began with the investigation of phase separation in molten core derived optical fibers for the development of transversely disordered, longitudinally invariant optical fibers for studying TAL. It was found that in these phase separated fibers, while the transverse microstructure contained physical properties (such as microphase size, pitch, and refractive index difference) that could support TAL, along the longitudinal axis, the formed microphases were spherical in shape, leading to an opaque core unable to waveguide. This led to the development of a novel fiber fabrication process, the two-tier molten core method of fiber fabrication (Chapter II), in an attempt to elongate the formed microphases. During the fiber draw, the molten core dissolves some of the surrounding silica which ultimately dilutes the core composition, shifting it to higher silica concentrations. While generally considered problematic when specific (low SiO_2 containing) compositions are desired, this was utilized to control the viscosity and permit some elongation of the microphases during a secondary redrawing stage. Unfortunately, the resulting elongation was not sufficient for waveguiding. It was found that the lack of elongation was because of the low viscosity of the core phase, effectively limited by the high draw temperature (due to the silica cladding). Additionally, while not relating to TAL, this work has improved the understanding of phase separation and phase transitions that can occur in MCM-derived optical fibers, and the impact of processing on the final microstructure, which ultimately led to the realization of a potential fiber medium for random lasing, and serendipitously a magnetic polycrystalline fiber.

To combat the longitudinal invariance, a second fiber fabrication method was developed through an adaptation of the stack-and-draw technique to incorporate MCM-derived precursor fibers, demonstrated for the first time in this Dissertation (Chapter III). Core/clad optical fibers were initially drawn using the MCM, had the coating removed, were stacked together in a capillary preform and drawn down to the final fiber containing a disordered "core of cores." The final fiber consisted of a disordered structure of higher refractive index phases (what were the fiber cores), surrounded by a lower refractive index phase (what was the fiber cladding). The random microstructure led to random propagation constants of the supported modes which reduces the optical tunneling efficiency (or diffusion of the beam) [1]. This *absence of diffusion* was translated as TAL by Abdullaev, *et al.* [2]. It was found that even though the microstructural properties were not perfect (quasi-periodic microstructure, low Δn), strong localization can occur. This has resulted in a rather straightforward method of developing all-solid TALOFs with varying compositions, effectively providing a platform for further studies into the material influences on transverse Anderson localization in optical fibers.

This newly developed technique of disordered optical fiber fabrication led to the first ever doped silicate TALOFs being realized, comprised of passive (SrO and Al_2O_3, Chapter III), active (Yb_2O_3 and Er_2O_3, Chapter IV), and nonlinear dopants (SrO, Al_2O_3, and Yb_2O_3, Chapter V). Additionally, the precursor constituents utilized in the stack-and-draw method have extended beyond MCM-derived optical fiber to in-house designed MCVD-derived hollow core fibers. Inasmuch, this technique has proved highly versatile for incorporating new dopants into the disordered core, thus opening the periodic table for further studies of material influences on transverse Anderson localizing optical fiber. Present losses were too high in these fibers for the demonstration of either lasing or amplification in these TALOFs. However, rather unexpectedly, it was found that in the presence of spontaneous emission, TAL appears to be lost. When pumping the active TALOFs at wavelengths within the ion absorption bands, spontaneous emission would occur that ultimately masks the localization. It is not clear if the localization is completely destroyed, or if the spontaneous emission simply covers up the localization. While this may not be necessarily beneficial for lasing, the spontaneous emission could potentially be used to pump other seed sources in various localized modes for amplification, once the losses have been improved.

Even though the resulting Δn was low in these TALOFs, thereby resulting in an estimated silica-like nonlinear refractive index (n_2) in the higher index phases, the transversely disordered optical fiber demonstrated strong TAL in various regions across the fiber cross-section. This permitted small localized mode areas (A_{eff}) of less than 40 μm^2. The resultingly small A_{eff} permitted the first reported observation of optical nonlinearities in a TALOF, specifically Raman and FWM. Longitudinal inhomogeneities are likely impacting the FWM, and therefore shorter lengths of fiber could be used to suppress Raman scattering, while enhancing FWM due to minimizing longitudinal inhomogeneities along the length of the fiber. As to the interplay between optical nonlinearities and TAL, the results of this Dissertation at the very least support the conclusion that the presence of nonlinearities and TAL are not mutually exclusive. The nonlinearity resulting from strongly localized modes is enough to generate FWM, and localization is maintained. Whether this localization is enhanced or weakened in the presence of nonlinearities is not conclusive and requires further analysis. This work is not meant to be decisive as to the underlying nature of Anderson localization in the presence of nonlinearities; however, it provides an experimental platform for providing insight into these fundamental questions.

Finally, an in-house technique used to characterize the disorder of the core microstructure in these optical fiber systems was devised utilizing a radial distribution function to measure the number of inclusions present within the cross-section of the core as a function of the radius. The variance of the number of inclusions per radius indicates the percent deviation away from the average value. For a theoretical photonic crystal fiber, the number of inclusions scales linearly with the increase in radius; therefore, the variance becomes 0%. For the fibers containing micro-inclusions in the core, the percent variance ranged from 2% to 10% in the stack-and-draw fibers, and over 100% variance for the phase separated fibers, indicating the degree of disorder present within the various fiber systems. While initially this analysis was done merely to compare the disorder in the microstructure of the fibers developed, it may potentially be useful to predict the overall strength of localization possible by using an image of the fiber cross-section.

VI. B. Present Challenges for Glass Anderson Localizing optical fibers

Disordered optical fibers were developed by each of the fabrication techniques studied and adapted throughout this Dissertation (fabricate and elongate the formed microphases of a phase separated system, stack-and-draw of precursor optical fibers). However, not all of these techniques resulted in TALOFs. Those that did, brought with them their own set of challenges that can be further optimized.

First and foremost, TALOFs are difficult to fabricate. The fabrication methodology presented in this Dissertation is straightforward, however the implementation is challenging, tedious, and incredibly time-consuming. A single TALOF takes significant precursor preparation with multiple fiber draw stages (first to draw the precursor fibers, then to draw the final stack). Even utilizing hollow tubes within the stack requires the tubes to first be drawn to different dimensions before the final draw. Due to the randomness desired in the microstructure, there is no one single recipe for developing these fibers, as there are many “knobs” throughout the fabrication process that can be turned to tailor the core microstructure of these TALOFs. This Dissertation presents a method for developing these fibers, however, there remains ample opportunities for optimizing the fiber fabrication process to reduce time, cost, and material loss (broken fibers).

Since TALOFs are new in practice, many of the standard characterization techniques used for commercial / conventional optical fibers need to be adapted as well. Much of the characterization reported in this Dissertation was done through free-space optics. This consequently yields high loss with mode coupling. Inasmuch, the loss mechanism(s) is(are) not entirely well understood in these fibers. Even though the precursor fibers possessed loss values on the order of dB/m, the loss measured in these TALOFs are on the order of dB/cm. Air bubbles are observed along the length of the fibers and likely contribute to this loss but may not be the only factor. Additionally, the refractive index difference between the higher and lower index phases is quite low (0.01) which could lead to transverse scattering (more loss). Further studies are necessary to understand the overarching loss mechanisms within the modes of these fibers and to better understand and ultimately characterize the loss in these fibers. Furthermore, theoretical studies are necessary to understand the impact of the material (Δn) and the microstructure on wave propagation in these fibers to begin understanding the sources of loss.

The high measured loss and delocalization resulting from the absorption and spontaneous reemission in the active TALOFs presently limits the performance of lasing and amplification. The reemission masks the localization, raising doubt when aligning the pump laser into localized modes. Ideal transverse Anderson localizing optical fibers should localize everywhere across the facet of the fiber. Those presented in this Dissertation only localize in a few select modes. Overall, there are far too many uncertainties when characterizing these novel fibers. Once the theoretical understanding of the characterization has progressed, further material development can occur.

VI. C. Future Perspectives

VI. C. 1. Phase separation

Slight microphase elongation was demonstrated in Chapter II with the NiO-SiO_2 system, however it was insufficient for waveguiding. As shown by T. Seward [3], the elongating of microphases is possible in glass that ultimately demonstrates waveguiding. The limitation with the system presented in this Dissertation is the composition (thereby the viscosity) of the protective cladding. The viscosity of the core is significantly lower than that of the cladding, therefore, the temperature required for redrawing is much too high to permit microphase elongation of the already phase separated core. This could potentially be remedied through use of a different cladding composition, one that draws at a lower temperature. For example, Duran^{TM} borosilicate glass can be used as a preform and is drawn below 1000°C. This permits for lower melting temperature compositions to be investigated, such as bismuth or high alkali containing glasses. With enough understanding of the MCM, one can predict the composition in the final core when drawing with these various claddings. Then, the correct cladding could be selected to match the viscosity of the resulting phase separated core, potentially resulting in elongated microphases.

On the other hand, the ZrO_2 – SiO_2 system has a liquidus for the liquid-liquid immiscibility region higher than the draw temperature for fused silica (approximately 2200°C [4]). Therefore, simply beginning with powder in the silica preform will not draw at 2100°C, as shown in Figure VI.1.a with the unmelted power remaining in the drawn glass. A flux may be added to tailor the melting temperature, and potentially the core

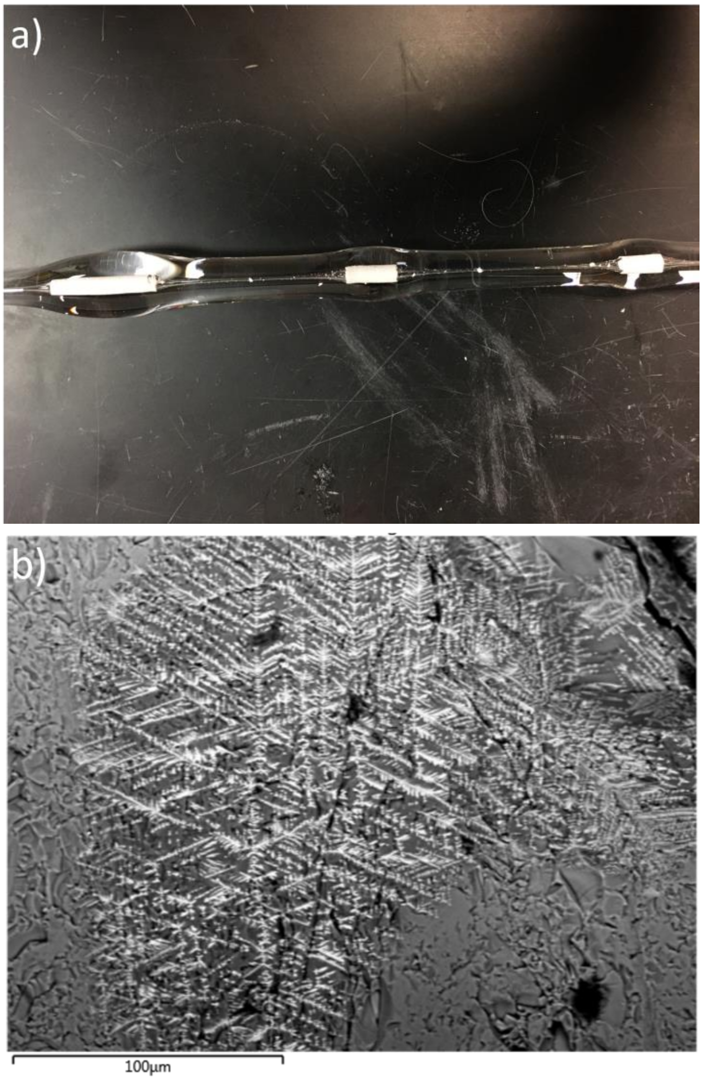

Figure VI.1. a) The large diameter cane sample with pure ZrO_2 as the powder composition, the large white rods are unmelted powder. b) An electron micrograph of the ZrO_2-Li_2O derived core showing devitrification.

viscosity, to permit microphase elongation. Unfortunately, many general fluxes (i.e., Li_2O) often lead to devitrification of the glass (Figure VI.1.b). However, tailoring the precursor composition to include other flux agents, such as CaO, may still be a viable route for tailoring the composition of the ZrO_2 system.

VI. C. 2. Stack-and-draw

The fibers presented throughout this Dissertation developed using this modified stack-and-draw simply demonstrate the beginning of TALOF development. The versatility of the MCM opens the periodic table for investigating optical fiber core compositions having never been developed. In turn, these novel composition fibers can be stacked and drawn following the methodology outlined in this Dissertation to draw TALOFs. The optical properties of the precursor fibers can be characterized to provide a baseline for those the resulting TALOF should possess. This would provide both a route for optimizing the characterization techniques, as well as optimizing the fabrication process. Finally, this stack-and-draw method is not limited to fibers drawn using the MCM. As shown by T. Tuan, *et al.* [5], rods of two homogeneous glass compositions can be stacked in a preform (containing similar mechanical properties, i.e., thermal expansion coefficient and viscosity) and drawn to a disordered TALOF. Commercial off-the-shelf (COTS) optical fibers could potentially be used as well to develop these TALOFs and would provide a good comparison as many of the optical properties of the COTS fibers are well-known.

One of the limitations of the TALOFs developed throughout this Dissertation is the low Δn between phases in the final fiber. Initial attempts at utilizing semiconductor core fibers (Δn greater than 2) were unsuccessful due to the oxidation of the silicon core during redrawing. There are, however, many more semiconductor core compositions that have been reported in the past few years [6,7], including silicon-germanium [8], germanium [9], and indium-antimonide [10] to name a few. Some of these compositions were drawn around 1000°C in soft-glass preforms. These compositions drawn at lower temperatures may be less susceptible to oxidation than if drawn in a silica preform (diffusion is a temperature driven process) and therefore may retain the higher index phase in the final disordered fiber. Unfortunately, many of these semiconductor core fibers reported high loss (dB/cm). If the loss observed in these TALOFs is a result of the fabrication process, even if the semiconductor core phase is retained after stacking-and-drawing, the losses may be substantially high for any measurements to be conducted.

A secondary attempt at introducing high Δn scattering centers into the core was through stacking and drawing hollow-core optical fibers doped with an active ring layer surrounding the hole. However, the holes in the fibers collapsed during the draw, consolidating into an all-solid core. At lower draw temperatures, it was found that the cores remained closed, but the interstitials between the fibers began separating. Reducing the temperature further results in the fiber breaking during the draw. Instead of reducing the temperature, it may be possible to draw the stack of hollow core fibers while pressurizing the preform to keep the central holes open. This process is generally done for drawing hollow-core photonic crystal fibers [11]. With the interstitials separated, the mechanical durability of the fiber diminishes. As such, when the fibers were cleaved for localization measurements, the core would shatter. The silica and air TALOFs reported by J. Zhao, *et al.* [12], contained a higher fill fraction of air, were much smaller in diameter (250 μm as compared to 1 mm), and were cleaved without shattering the core, suggesting smaller diameter fibers may be a viable route.

Loss may be the most limiting factor (and the least understood) in the fibers developed in this Dissertation. A detriment is the destructive nature of the cutback method. The standard procedure for the cutback method is to align the input beam into the desired mode, measure the output power, remove a known length from the output end of the fiber, measure the output power and repeat. Each increment should see an increase in power. This change in output power as a function of length represents loss. Regarding a TALOF, the question becomes: which single mode represents the entirety of the localized modes across the fiber, since all localized modes are different? How does one begin to answer this question without prior knowledge of the loss in each individual mode? Moving the input beam to different modes at each increment changes the input conditions within each mode, which impacts the accuracy of the measurement. When utilizing the bulk of the TALOF for applications such as image transport, the performance of individual modes becomes less important. However, when specific modes are excited for active applications (lasing or amplification), or studies regarding optical nonlinearities, the loss becomes more critical.

To begin to better understand loss in these fibers, or at least begin ruling out certain culprits, two TALOFs can be developed and compared. The first would be developed using COTS Yb-doped fibers (dB/km loss), and the second would be MCM-derived Yb-doped fibers (dB/m loss) drawn with a similar core composition and diameter. If the precursor fibers were processed identically (i.e., consistent etching times), and fiber draw conditions were identical (preform dimensions, draw temperature), the resulting microstructure should be similar in the final TALOFs. Then, all modes could be characterized in each fiber using a CCD camera to extract the intensity profiles, and modal effective areas could be determined. Finally, measure the loss using the cutback method only characterizing a single mode in each fiber with comparable effective areas to keep the input conditions consistent during the measurement. If the magnitude of loss is similar, impurities from the precursor powders used to develop the MCM-derived fibers can be ruled out as a major contributing factor of loss, suggesting it is likely a result of the microstructure or unexpected micro-inclusions along the length of the TALOF.

If the loss is a result of the microstructure, a more thorough understanding of the evolution of the microstructure along the length of the fiber is necessary. Instead of cleaving samples every 10 cm as demonstrated in Chapter IV, samples could be cleaved in 1 cm increments (or smaller, depending on the quality of the cleaver) and imaged. These images could be compiled, and a representative 3D image produced. Alternatively, a nondestructive method of characterizing the microstructure can be done with x-ray computed tomography (CT) with up to nanometer resolution [13-15] to develop a 3D representation of the microstructure. This would provide a more accurate depiction of the microstructure and can begin providing clues as to the origins of loss in these TALOFs. Additionally, it would support theoretical models to better understand how the light is propagating along the fiber in certain localized modes.

Loss in these TALOFs is likely a combination of mechanisms; low Δn causing light leakage, micro-inclusions causing scattering, precursor impurities, however these claims are simply speculation. Once the mechanisms driving loss in these TALOFs are better understood, they can be alleviated in subsequent generations of these TALOFs.

As discussed in Chapter IV regarding the actively doped TALOFs, depending on the amplification performance of pumping various localized modes with spontaneous emission, another option for pumping the Er-doped TALOF amplifier could be to side-pump the fiber. This could potentially amplify all localized modes in the cross section, whereby individual modes could then be seeded. It would be interesting to compare the efficiency of the two pumping schemes. Additionally, while the spontaneous emission might be an unanticipated challenge, rather clever techniques of incorporating light absorbing claddings in optical fibers have been utilized, such as double-clad erbium-doped fiber amplifiers with the inner clad doped with absorbing ions such as samarium (Sm) [16-18]. The absorption spectra of Sm overlaps with the amplified spontaneous emission (ASE) spectra of Er and can effectively filter the amplification wavelength [16,18]. A next-generation iteration of this Er-doped TALOF could have a secondary ring layer doped with Sm around the higher-index phases (or simply dope the lower index phase) to filter the spontaneous emission, so the higher index (Er-doped) regions potentially maintain the lasing / amplifying light.

Since it has been determined that optical nonlinearities and TAL are not necessarily mutually exclusive, the impact of optical nonlinearities on TAL can be further investigated by providing experimental evidence within these TALOFs to support the theoretical models. Using MCM-derived fibers with dopants containing higher nonlinear refractive indices (i.e., GeO_2 or Y_2O_3) could enhance the nonlinearities observed in these fibers. Furthermore, pumping these localized modes with two high intensity pulsed lasers simultaneously (e.g. 532 nm and 1064 nm) could aid in FWM generation. Also, if all localized modes in these fibers have different modal properties, it may be possible to demonstrate multiple four-wave mixing (FWM) frequency shifts in a single TALOF, simply by pumping different localized modes. Finally, since lasing in these fibers through use of active ions (e.g. Yb^{3+} or Er^{3+}) proves challenging, and a strong Raman shift is observed in many of the modes, it may be possible to create a Raman laser [19] with the TALOF in a similar cavity setup as used in Chapter IV. Since, rather unexpectedly, it was found that spontaneous emission masks the localization, and postulated that directional emission would relocalize the beam, such a schematic could potentially provide insight into the effects of directional emission (lasing) on TAL.

VI. C. 3. Additive Manufacturing

A more recent technique demonstrated by a few groups is the development of both core/clad and microstructured optical fiber through additive manufacturing (AM) [20-24]. AM [25] is the process of developing specialized parts through depositing the material layer by layer until the final 3D part is "printed." The beauty of AM stems from an ability to design an image or structure in some computer 3D modeling software, and subsequently have a part printed. Several techniques of additive manufacturing include Fused Deposition Modeling (FDM), Selective Laser Sintering (SLS), and

Stereolithography (SLA). AM is not limited to polymer printing, as glass and metal [25] parts have been demonstrated in recent years with high precision.

FDM utilizes a filament that is melt extruded and deposited on a platform. The layers cool and harden before subsequent layers are deposited until the full part has been fabricated. The resolution is determined by the tip of the extrusion head and generally is on the order of a few hundred microns. Instead of extruding a molten phase, SLS (as the name suggests) uses a laser to sinter a powdered material. Powder is added to the deposition platform and the laser sinters specific regions to begin fabricating the part. This process continues layer-by-layer until the final part is produced. Since SLS is laser-assisted, the resolution is comparable to the laser beam width and can be much smaller than FDM. SLA is a similar process, except the powder material is replaced with a light-curing resin or a photopolymer. A light source (usually UV, 365-405 nm) selectively cures the polymer until the final part is produced.

Depending on the desired application, different AM techniques can be used for development of the final part. Through AM, virtually any microstructure can theoretically be designed in a 3D computer software and subsequently printed to a precursor rod, which can then be drawn to the final fiber. The composition can be altered to study various material properties, or the microstructure can be tailored to change the size, shape, and number of inclusions present within the printed part to study the physics of wave propagation in custom designed microstructures that closely resemble those used in theoretical models. Then, through careful drawing parameters, the printed part can be drawn to a fiber possessing the desired microstructural dimensions. This potentially offers a method for precisely designing truly randomized structures within the core of an optical fiber and effectively bridging the theory of transverse Anderson localization of light in an optical fiber to the experimental counterpart.

VI. D. References

[1] A. Mafi, J. Ballato, K. W. Koch, and A. Schülzgen, "Disordered Anderson localization optical fibers for image transport – A Review," *Journal of Lightwave Technology* **37**(22), 5652-5659 (2019).

[2] S. S. Abdullaev and F. K. Abdullaev, "On propagation of light in fiber bundles with random parameters," *Radiofizika* **23**, 766–767 (1980).

[3] T. P. Seward, "Elongation and spheroidization of phase-separated particles in glass," *Journal of Non-Crystalline Solids* **15**(3), 487-504 (1974).

[4] R. Telle, F. Greffrath, and R. Prieler, "Direct observation of the liquid immiscibility gap in the zirconia-silica system," *Journal of the European Ceramic Society* **35**(14), 3995-4004 (2015).

[5] T. H. Tuan, S. Kuroyanagi, K. Nagasaka, T. Suzuki, and Y. Ohishi, "Characterization of an all-solid disordered tellurite glass optical fiber and its NIR optical image transport," *Japanese Journal of Applied Physics* **58**(3), (2019).

[6] J. Ballato, T. Hawkins, P. Foy, B. Yazgan-Kokuoz, C. McMillen, L. Burka, S. Morris, R. Stolen, and R. Rice, "Advancements in semiconductor core optical fiber," *Optical Fiber Technology* **16**(6), 399-408 (2010).

[7] A. C. Peacock, U. J. Gibson, and J. Ballato, “Silicon optical fibres – past, present, and future,” *Advances in Physics: X*, **1**(1), 114-127 (2016).

[8] D. A. Coucheron, M. Lokine, N. Patil, D. W. Breiby, O. T. Buset, N. Healy, A. C. Peacock, T. Hawkins, M. Jones, J. Ballato, and U. J. Gibson, “Laser recrystallization and inscription of compositional microstructures in crystalline SiGe-core fibres,” *Nature Communications* **7**, 13265 (2016)

[9] J. Ballato, T. Hawkins, P. Foy, B. Yazgan-Kokuoz, R. Stolen, C. McMillen, N. K. Hon, B. Jalali, and R. Rice, “Glass-clad single-crystal germanium optical fiber,” *Optics Express* **17**(10), 8029-8035 (2009).

[10] J. Ballato, T. Hawkins, P. Foy, C. McMillen, L. Burka, J. Ruppert, R. Podila, A. M. Rao, and R. R. Rice, “Binary III-V semiconductor core optical fiber,” *Optics Express* **18**(5), 4972-4979 (2010).

[11] Y. Y. Wang, N. V. Wheeler, F. Couny, P. J. Roberts, and F. Benabid, “Low loss broadband transmission in hypocycloid-core Kagome hollow-core photonic crystal fiber,” *Optics Letters* **36**(5), 669-671 (2011).

[12] J. Zhao, J. E. Antonio-Lopez, Z. Zhu, D. Zheng, S. Pang, R. A. Correa, and A. Schülzgen, “Image transport through meter-long randomly disordered silica-air optical fiber,” *Scientific Reports* **8**, 3065 (2018).

[13] M. Dogan, S. M. J. Moysey, R. M. Ramakera, T. A. DeVol, F. J. Beekman, H. C. Groen, and B. A. Powell, “High-resolution 4D preclinical single-photon emission computed tomography / X-ray computed tomography imaging of technetium transport

within a heterogeneous porous media," *Environmental Science & Technology* **51**, 2864-2870 (2017).

[14] W. K. Epting, J. Gelb, and S. Lister, "Resolving the three-dimensional microstructure of polymer electrolyte fuel cell electrodes using nanometer-scale X-ray computed tomography," *Advanced Functional Materials* **22**, 555-560 (2012).

[15] P. R. Shearing, J. Gelb, J. Yi, W.-K. Lee, M. Drakopolous, and N. P. Brandon, "Analysis of triple phase contact in Ni-YSZ microstructures using non-destructive X-ray tomography with synchrotron radiation," *Electrochemistry Communications* **12**, 1021-1024 (2010).

[16] S. Kim, U.-C. Ryu, and K. Oh, "41-nm 3-dB gain-band optical amplifier using an Er-doped core and Sm-doped inner-cladding fiber without external filters," *IEEE Photonics Technology Letters* **12**(8), 986-988 (2000).

[17] U.-C. Ryu, S. Kim, and K. Oh, "Gain controlling or erbium-doped fiber amplifier by samarium doped inner-cladding in the 1.5μm region," *Fiber and Integrated Optics* **20**(5), 471-477 (2001)

[18] K. Oh, S. Yoo, U.-C. Ryu, S. Kim, U.-C. Paek, D. B. S. Soh, J. K. Sahu, and J. Nilsson, "Spectral control of optical gain in a rare earth-doped optical fiber using novel triple layered structures," *Optical Fiber Technology* **12**, 297-304 (2006).

[19] K. O. Hill, B. S. Kawasaki, and D. C. Johnson, "Low-threshold cw Raman laser," *Applied Physics Letters* **21**, 181-183 (1976).

[20] W. Talataisong, R. Ismaeel, S. R. Sandoghchi, T. Rutirawut, G. Topley, M. Beresna, and G. Brambilla, "Novel method for manufacturing optical fiber: extrusion and drawing

of microstructured polymer optical fibers from a 3D printer," *Optics Express* **26**(24), 32007-32013 (2018).

[21] K. Cook, J. Canning, S. Leon-Saval, Z. Reid, M. A. Hossain, J.-E. Comatti, Y. Luo, and G.-D. Peng, "Air-structured optical fiber drawn from a 3D printed preform," *Optics Letters* **40**(17), 3966-3969 (2015).

[22] K. Cook, G. Balle, J. Canning, L. Chartier, T. Athanaze, M. A. Hossain, C. Han, J.-E. Comatti, Y. Luo, and G.-D. Peng, "Step-index optical fiber drawn from 3D printed preforms," *Optics Letters* **41**(19), 4554-4557 (2016).

[23] J. Canning, M. A. Hossain, C. Han, L. Chartier, K. Cook, and T. Athanaze, "Drawing optical fibers from three-dimensional printers," *Optics Letters* **41**(23), 5551-5554 (2016)

[24] Q. Zhao, F. Tian, Z. Yang, S. Li, J. Zhang, X. Zhu, J. Yang, Z. Liu, Y. Zhang, T. Yuan, and L. Yuan, "Optical fibers with special shaped cores drawn from 3D printed preforms," *Optik* **133**, 60-65 (2017)

[25] T. D. Ngo, A. Kashani, G. Imbalzano, K. T. Q. Nguyen, and D. Hui, "Additive manufacturing (3D printing): A review of materials, methods, applications and challenges," *Composites Part B: Engineering* **143**, 172-196 (2018).